**UNIVERSIDADE FEDERAL DE JUIZ DE FORA**
**FACULDADE DE ENGENHARIA**
**PROGRAMA DE PÓS-GRADUAÇÃO EM ENGENHARIA ELÉTRICA**

**Marcelo de Castro Fernandes**

# Multivariable Strategy for Modeling and Control Design of Voltage-Sourced and Back-to-Back Converters

Juiz de Fora

2022

**Marcelo de Castro Fernandes**

# Multivariable Strategy for Modeling and Control Design of Voltage-Sourced and Back-to-Back Converters

Master thesis presented to the Electrical Engineering Program of Universidade Federal de Juiz de Fora as partial fulfilment of the requirements for Master degree in Electrical Engineering. Area: Electric Energy Systems.

Supervisor: Pedro Machado de Almeida, Dr.Eng.

Co-supervisor: Janaína Gonçalves de Oliveira, Ph.D.

Juiz de Fora

2022

Ficha catalográfica elaborada através do Modelo Latex do CDC da UFJF
com os dados fornecidos pelo(a) autor(a)

de Castro Fernandes, Marcelo.
Multivariable Strategy for Modeling and Control Design of Voltage-Sourced and Back-to-Back Converters / Marcelo de Castro Fernandes. – 2022.
128 f. : il.

Supervisor: Pedro Machado de Almeida, Dr.Eng.
Co-supervisor: Janaína Gonçalves de Oliveira, Ph.D.
Dissertação (Mestrado) – Universidade Federal de Juiz de Fora, Faculdade de Engenharia. Programa de Pós-Graduação em Engenharia Elétrica, 2022.

1. Palavra-chave. 2. Palavra-chave. 3. Palavra-chave. I. Sobrenome, Nome do orientador, orient. II. Título.

**FEDERAL UNIVERSITY OF JUIZ DE FORA**
**RESEARCH AND GRADUATE PROGRAMS OFFICE**

**Marcelo de Castro Fernandes**

**Multivariable Strategy for Modeling and Control Design of Voltage-Sourced and Back-to-Back Converters**

Dissertation submitted to the
Graduate Program in Electrical Engineering
of the Federal University of Juiz de Fora
as a partial requirement for obtaining
a Master's degree in Electrical Engineering.
Concentration area: Electronic Systems

Approved on 17 of March of 2022.

**EXAMINING BOARD**

**Prof. Dr. Pedro Machado de Almeida –** Academic Advisor
Federal University of Juiz de Fora

**Prof. Dr. Janaína Gonçalves de Oliveira**
Federal University of Juiz de Fora

**Prof. Dr. Pedro Gomes Barbosa**
Federal University of Juiz de Fora

**Prof. Dr. Allan Fagner Cupertino**
Federal Center for Technological Education of Minas Gerais

Juiz de Fora, 03/17/2022.

Documento assinado eletronicamente por **Pedro Machado de Almeida**, **Professor(a)**, em 17/03/2022, às 11:45, conforme horário oficial de Brasília, com fundamento no § 3º do art. 4º do Decreto nº 10.543, de 13 de novembro de 2020.

Documento assinado eletronicamente por **Pedro Gomes Barbosa**, **Professor(a)**, em 17/03/2022, às 11:46, conforme horário oficial de Brasília, com fundamento no § 3º do art. 4º do Decreto nº 10.543, de 13 de novembro de 2020.

Documento assinado eletronicamente por **Janaina Goncalves de Oliveira**, **Professor(a)**, em 17/03/2022, às 11:46, conforme horário oficial de Brasília, com fundamento no § 3º do art. 4º do Decreto nº 10.543, de 13 de novembro de 2020.

Documento assinado eletronicamente por **Allan Fagner Cupertino**, **Usuário Externo**, em 17/03/2022, às 11:47, conforme horário oficial de Brasília, com fundamento no § 3º do art. 4º do Decreto nº 10.543, de 13 de novembro de 2020.

A autenticidade deste documento pode ser conferida no Portal do SEI-Ufjf (www2.ufjf.br/SEI) através do ícone Conferência de Documentos, informando o código verificador **0702332** e o código CRC **DE2BFB1E**.

**ACKNOWLEDGEMENTS**

I would like to express my profound gratitude to my supervisor, Prof. Pedro Machado, for his patience, support, friendship and confidence in my work. To my co-supervisor, Prof. Janaína Gonçalves, for all incentives, valuable advices and friendhsip. To the committee members for their effort in strengthening my work. To professors and colleagues from all laboratories I have worked in; thanks for motivating me during this journey. To my parents, Rose and Paulo, for giving me endless love and unlimited encouragement, crucial for completion of this work. To my sisters, Luiza and Patrícia, and my nephews Gabriel and Francisco, for their affection and incentive; thanks for inspiring me. To Gabriela, my fiancé, for giving me unconditional support and love; thank you for standing by me. To my aunt Bel for always being there for me. To my friends and family for being my safe heaven. I would like to thank all who somehow contributed for this work: muito obrigado!

## RESUMO

O sistema energético mundial atualmente passa por uma grande transição na qual conversores eletrônicos de potência ganham cada vez mais importância. Nesse contexto, conversores de fonte de tensão assim como sua associação em um conversor BTB, são bastante comuns e têm ganhado relevância. Essa dissertação de mestrado então apresenta a modelagem matemática desses dois conversores em uma estratégia de representação multivariável. Dois sistemas-teste são projetados: um sistema composto de um conversor fonte de tensão conectando a rede CA ao barramento CC, onde uma fonte de corrente CC é utilizada para representar o perfil de potência de uma microrrede CC, e um sistma composto de um conversor BTB que interconecta dois sistemas CA. Para o primeiro sistema duas estratégias de controle multivariável são apresentadas: um regulador linear quadrático (LQR) e de um controlador robusto, baseado na alocação de polos através de desigualdades matriciais lineares. Ambos os controladores são projetados para que o conversor tolere um fluxo de potência bidirecional. Já para o segundo sistema, um único controlador é projetado, também baseado na alocação de polos através de desigualdades matriciais lineares. Neste caso, o controlador é projetado para que o conversor BTB possa lidar com fluxo bidirecional de potência, além de incertezas e distúrbios nos parametros que compõe o sistema AC conectado a um dos terminais do conversor. Ambos os sistemas são implementados em um ambiente de simulação digital e as respostas dinamicas são avaliadas e comparadas.



Palavras-chave: Conversores Fontes de Tensão. Modelagem Multivariável. Controladores Multivariáveis.

**ABSTRACT**

The world's energy system is currently undergoing a major transition in which power eletronic converters gain more importance. In this context, voltage-sourced converters just like their association on Back-To-Back converters, are rather common and have gained more relevance. This master thesis then presents the mathematical modeling of both converters in a multivariable representation strategy. Two test systems are designed: one system composed of a voltage-sourced conveter connecting an AC grid to a DC bus, in which a DC current source is used to represent the power profile of a DC microgrid, and a system composed of a BTB converter that interconnects two AC systems. For the first system, two multivariable control strategies are presented: a linear quadratic regulator (LQR) and a robust controller which is based on pole placement via linear matrix inequalities. Both controllers are designed so the converter might deal with a bidirectional power flow. For the second test system, one single controller is designed and it is based on pole placement via linear matrix inequalities. In this case, the controller is designed so the BTB converter might deal with bidirectional power flow, while being resilient against uncertainties and disturbances in the parameters that compose the AC system connected to one of the converter's terminals. Both systems are implemented in a digital simulation environment and their dynamic responses are assessed and compared.

Keywords: Voltage-Sourced Converters. Multivariable Modeling. Multivariable Controllers.

## LIST OF FIGURES

## LIST OF TABLES

SUMARY

# 1 INTRODUCTION

## 1.1 Background

The world is currently undergoing a major transition regarding energy systems which have important effects in the power sector. Concerns with environmental impacts and with nations' energy security have bolstered the research on alternative and renewable sources of energy. As many governments use specialized policies to push for the deployment of renewable energy sources, Wind and Solar Photovoltaics (PV) have experienced a major increase in the past few years (COZZI; GOULD, 2017).

This energy transformation, however, is not only limited to large renewable-based power plants nor it is restricted to the power industry alone. Concerning the former, it is possible to cite the Distributed Energy Resources (DER) which have been drawing the attention of both industry and academia, especially when associated with the various types of microgrids. Moreover, the energy transition has also been present in the vehicle industry such as cars and even airplanes. Although all these cases might appear to be disconnected, they have many things in common and the main actors that are shared by all these different examples are the power electronic converters.

For example, when the subject is microgrids, they can be AC, DC or hybrid and they are normally composed of multiples sources of energy, mainly renewable-based, and loads which are commonly connected at distributed-level grids (OLIVARES *et al.*, 2014). The conection of microgrids in the point of common coupling is generally performed by power electronic converters, such as the Voltage-Sourced Converter (VSC), which operates using specially designed controllers that guarantee a safe and adequate operation for all components composing the microgrid (ORNELAS-TELLEZ *et al.*, 2017).

In fact, the integration of microgrids to the bulk power system introduces many challenges regarding the control these interface converters. As an illustration, it is possible to mention the bidirectional power flows that should be natural in these connections (OLIVARES *et al.*, 2014). A microgrid might have many non-dispatchable power surces and, therefore, it might have to deal with a power flow constantly being inverted from the two connected systems. In this cases, generated and consumed energy might not always be in balance and when power demand by the loads connecte to the microgrid is high, energy must be drained from the bulk power system. The contrary might also occur, when power demand by those loads is low, energy must be sent to the power system. This subject has been the main topic of different research publications in literature, especially the proper design of controllers that can properly handle these issues (CHEN *et al.*, 2016; MIRANDA *et al.*, 2013).

Voltage-sourced converters can also be combined for creating new power electronic devices that are used in solutions proposed for power system enhancement and improvement.

Among these devices, the Back-To-Back (BTB) converter is one of the most common topologies used in industry to perform low-power and low-voltage connection between two AC systems. The Back-to-Back based on Voltage Source Converter (BTB-VSC) consists in two VSCs sharing a common link on the DC side while performing the interconnection of two different AC systems. BTB converters are frequently used in Unified Power Quality Conditioners (UPQC) and in applications related to renewable energy generation such as wind generators connected to the grid (BLAABJERG; LISERRE; MA, 2011; CHEN, 2013). These controlled power electronic devices can be especially designed in order to make the grid more resilient and robust, and its usage has been increasing due to some interesting characteristics such as: (i) the provision of wide control in bidirectional power flow and (ii) independent control of active and reactive power allowing a flexible operation (FRIEDLI *et al.*, 2011). Furthermore, these two characteristics, when combined, lead to the interesting property of rapid manipulation of power flows in order to provide the balance between two different systems (RODRÍGUEZ-CABERO; SÁNCHEZ; PRODANOVIC, 2016).

It is evident that the control approach is essential in order to take advantage of the important benefits associated with the single VSC and with the BTB-VSC. The conventional control strategy designed for these converters is based on two loops: the inner and the outer (RODRÍGUEZ-CABERO; SÁNCHEZ; PRODANOVIC, 2016). The inner controller usually deals with the AC current injected by each or by the single VSC while the outer controller addresses the DC link capacitor voltage. In order for this strategy to work properly and the controllers to be designed independently, the inner loop should have much faster action than the outer loop (YAZDANI; IRAVANI, 2010). As an illustration, this conventional configuration of two control loops is shown in (ALCALA *et al.*, 2011) to perform the regulation of a BTB converter dealing with bidirectional power flow.

Although the conventional control approach is well established, many different alternative strategies have been proposed lately in the literature. One example of an alternative control strategy, when dealing with these converters, is the full state-feedback. In (RODRÍGUEZ-CABERO; SÁNCHEZ; PRODANOVIC, 2016) a unified multi-variable strategy is proposed to control a BTB converter with LCL output filters. The proposed state feedback strategy is found to deal very well with transient mismatches of power flow and to outperform the traditional inner-outer loop approach. In (OSÓRIO *et al.*, 2018) a robust control strategy is proposed to a grid-connected inverter. Results show that the controller ensure a stable operation and good performance for a set of uncertainties related to the grid equivalent inductance and resistance at the Point of Common Coupling (PCC).

Therefore, it is clear that new strategies for regulating VSC and BTB converters are welcome and that new studies should be performed so it could facilitate researchers to take advantage of the best of features each controlled converters has to offer. Therefore, in this context, this study presents a multivariable approach for modeling and control of a single voltage-sourced converter and for a back-to-back converter. In addition, this

study presents the comparison of two multivariable control strategies for the VSC, while assessing the robustness of a multivariable approach for the BTB converter.

## 1.2 Objectives and Scope

This master thesis has the following objectives:

- To present and describe mathematical tools that are used in the modeling theory of power electronic converters together with tools that are used for studying dynamical systems, such as stability and linearization procedures. These techniques should be presented with enough detail to allow future students to read this report, to comprehed the subject and apply the concepts to design multivariable control strategies for power electronic converters.
- To present and scrutinize multivariable mathematical models for a single Voltage-Sourced and for Back-to-Back converters. Moreover, this master thesis should also perform linearization of such converters' numerical models for obtaining linear representations, enabling the design of multivariable linear control systems.
- Present two multivariable control strategies, the LQR and LMI-based robust pole placement approaches, design the controllers, test and assess their performance in a system composed by a single VSC that interfaces a DC and an AC system, while dealing with bidirectional power flow.
- Design an LMI-based robust pole placement control strategy for the BTB converter that is able to deal with bidirectional power flow and to uncertainties or disturbances that can occur in the parameters that compose one of the two AC systems being connected to the converter.
- Implement and test both systems in a simulation environment.

## 1.3 Outline

The remainder of this master thesis is organized as follows: Chapter 2 presents the theoretical foundations for linear algebra and for dynamic systems that are used in the modeling of both converters and control strategies. In Chapter 3, the mathematical model for the converters is obtained by using some of the tools presented in previous chapters. Chapter 4 presents applies the linearization concepts to the studied converters, while multivariable linear control strategies are presented. The controller design procedure and numerical implementation of the control strategies is carried out in Chapter 5, together with a description of the experiments to be performed for testing controller performance for the appropriate converter. The simulation results are presented and discussed in Chapter 6. Conclusions are drawn in Chapter 7.

# 2 THEORY FUNDAMENTALS

The study presented here tries to use concepts and techniques already consolidated in the dynamical systems and linear algebra fields to build a better interpretation and understanding for phenomena observed in the analysis and control of power electronic devices. Therefore, it is obviously necessary to describe the techniques and concepts that are essential for the work developed in this study. In order to do so, this chapter lays all the foundation and summarizes the important theoretical aspects that are needed for the complete understanding of the present master thesis.

## 2.1 LINEAR ALGEBRA

This section is concerned with the presentation of some basic concepts related to the vectors and matrices. The concepts related to norms are important for understanding sizes and, consequently, distances. On the other hand, the concepts related to matrix decompositions are going to be extremely useful when linear systems are being studied.

### 2.1.1 Vector and Matrices Norm

The concept of norm $\|\cdot\|$ is needed for the definitions of sizes and distances that are used in different topics of this work. First, let us introduce the three necessary conditions for a function to be considered a norm. Let $\mathbf{x}_1$, $\mathbf{x}_2$ be vectors in $\mathbb{R}^n$ and $\gamma \in \mathbb{R}$. Then, according to (TREFETHEN; III, 1997), the vector norm should satisfy the following

**i.** $\|\mathbf{x}_1\| \geq 0$ and $\|\mathbf{x}_1\| = 0 \Rightarrow \mathbf{x}_1 = \mathbf{0}$,

**ii.** $\|\mathbf{x}_1 + \mathbf{x}_2\| \leq \|\mathbf{x}_1\| + \|\mathbf{x}_2\|$,

**iii.** $\|\gamma\mathbf{x}_1\| = |\gamma|\|\mathbf{x}_1\|$.

Under these assumptions, a really useful norm is the $p-$norm. They are defined as

$$\|\mathbf{x}\|_p = \left(\sum_{j=1}^{n} |x_j|^p\right)^{\frac{1}{p}}. \tag{2.1}$$

where $\mathbf{x} = [x_1 \ x_2 \ \cdots \ x_j \ \cdots \ x_n]^\intercal$. The most useful norms are $p = 1, 2, \infty$ (ZHOU; DOYLE, 1998). For a $n \times 1$ vector $\mathbf{x}$, these norms can be described as

$$\|\mathbf{x}\|_1 = x_1 + x_2 + \cdots + x_n, \tag{2.2}$$

$$\|\mathbf{x}\|_2 = \sqrt{x_1^2 + x_2^2 + \cdots + x_n^2} = \mathbf{x}^\intercal \mathbf{x}, \tag{2.3}$$

where the superscript $^\intercal$ stands for the transpose operation, and

$$\|\mathbf{x}\|_\infty = \max_{1 \leq j \leq \infty} |x_j|. \tag{2.4}$$

Concerning matrices, the most important norms for this study are the induced norms (TREFETHEN; III, 1997)(ZHOU; DOYLE, 1998). These types of norms are calculated as a ratio between the norms of two vectors. The idea behind the induced norm is that a matrix $\mathbf{A} \in \mathbb{R}^{m \times n}$ can be interpreted as a linear map between a vector $\mathbf{x} \in \mathbb{R}^n$ and a vector $\mathbf{Ax} \in \mathbb{R}^m$. Hence, if the matrix norm defining as the largest possible ratio between the $p$-norm of $\mathbf{Ax}$ and $\mathbf{x}$ it will, in fact, present how the matrix can stretch or reduce a vector. Therefore, the $p$-norm of a matrix can be defined as

$$\|\mathbf{A}\|_p = \sup_{\mathbf{x} \neq \mathbf{0}} \frac{\|\mathbf{Ax}\|_p}{\|\mathbf{x}\|_p}, \tag{2.5}$$

or

$$\|\mathbf{A}\|_p = \sup_{\|\mathbf{x}\|_p = 1} \|\mathbf{Ax}\|_p. \tag{2.6}$$

In this work, unless it is stated otherwise, the operation $\|\cdot\|$ will be equivalent to the 2-norm. Hence

$$\|\mathbf{x}\| = \|\mathbf{x}\|_2, \tag{2.7}$$

and

$$\|\mathbf{A}\| = \|\mathbf{A}\|_2. \tag{2.8}$$

### 2.1.2 Matrix Decompositions

Properties regarding matrices are really important for linear systems. Among all factorizations, the eigendecomposition and the singular value decomposition are really useful for the study presented here and, thus, they are going to be discussed next.

#### 2.1.2.1 *Eigenvalue and Eigenvectors*

The Eigendecomposition of a matrix is of extreme importance for the study conducted here. This is due the relation between eigenvalues of a matrix and the dynamic behavior of the linear system described by that matrix. These concepts are going to be further discussed later in this very chapter, but for now it is important to describe what is an eigenvalue and an eigenvector.

First, let $\mathbf{A} \in \mathbb{R}^{n \times n}$. Then, it is possible to raise the question wether exists a non-zero vector $\mathbf{q}_1 \in \mathbb{R}^{n \times 1}$ such that the linear transformation $\mathbf{A}\mathbf{q}_1$ produces a vector colinear with $\mathbf{q}_1$ (DERUSSO; CLOSE; ROY, 1990). If such vector exists, then $\mathbf{q}_1$ and $\mathbf{A}\mathbf{q}_1$ are proportional to each other and their proportionality scalar constant is $\lambda_1$, which is said to be the eigenvalue (DERUSSO; CLOSE; ROY, 1990). In this situation, $\mathbf{q}_1$ is said to be the right eigenvector corresponding to eigenvalues $\lambda_1$. Therefore, for each eigenvalue, it is possible to write the following equation:

$$\mathbf{A}\mathbf{q}_i = \lambda_i \mathbf{q}_i, \tag{2.9}$$

where $i = 1,2,\ldots,n$. If all equations are written simultaneously, we have that

$$\mathbf{A}\mathbf{Q} = \mathbf{Q}\mathbf{\Lambda}, \tag{2.10}$$

or

$$\mathbf{A} = \mathbf{Q}\mathbf{\Lambda}\mathbf{Q}^{-1}, \tag{2.11}$$

where

$$\mathbf{\Lambda} = \begin{bmatrix} \lambda_1 & 0 & \cdots & 0 \\ 0 & \lambda_2 & \cdots & 0 \\ \vdots & \vdots & \ddots & \vdots \\ 0 & 0 & \cdots & \lambda_m \end{bmatrix}, \tag{2.12}$$

and

$$\mathbf{Q} = \begin{bmatrix} \mathbf{q}_1 & \mathbf{q}_2 & \cdots & \mathbf{q}_m \end{bmatrix}. \tag{2.13}$$

First note that $\mathbf{\Lambda}$ is a diagonal matrix and that the eigenvalue decomposition allows matrix $\mathbf{A}$ to be represented as $\mathbf{\Lambda} = \mathbf{Q}^{-1}\mathbf{A}\mathbf{Q}$. This is called diagonalization and it

is important to state that not every system is diagonalizable. However, this will not be the case in this study and the interested reader can reffer to (DERUSSO; CLOSE; ROY, 1990) for ways of addressing this problem with Jordan blocks.

#### 2.1.2.2 *Singular Value Decomposition*

Next is another extremely important matrix representation, the Singular Value Decomposition or SVD. This is because the SVD is incredibly helpful to determine things such as the 2−norm of a matrix and singular vectors can be used to determine if input output relations are weak or strong. First it is necessary to state that the SVD exists for every matrix and that its singular values are unique (ZHOU; DOYLE, 1998). For instance, let $\mathbf{A} \in \mathbb{R}^{n\times n}$, then exist unitary matrices

$$\boldsymbol{\Upsilon} = \begin{bmatrix} \boldsymbol{\upsilon}_1 & \boldsymbol{\upsilon}_2 & \cdots & \boldsymbol{\upsilon}_m \end{bmatrix} \in \mathbb{C}^{n\times n}, \tag{2.14}$$

$$\mathbf{V} = \begin{bmatrix} \mathbf{v}_1 & \mathbf{v}_2 & \cdots & \mathbf{v}_n \end{bmatrix} \in \mathbb{C}^{n\times n}, \tag{2.15}$$

$$\tag{2.16}$$

where $\boldsymbol{\upsilon}_i \in \mathbb{C}^{n\times 1}$, $\mathbf{v}_i \in \mathbb{C}^{n\times 1}$ are unit vectors for all $i$ such that

$$\mathbf{A} = \boldsymbol{\Upsilon}\boldsymbol{\Sigma}\mathbf{V}^{\dagger}, \tag{2.17}$$

where $^{\dagger}$ denotes the conjugate transpose,

$$\boldsymbol{\Sigma} = \begin{bmatrix} \sigma_1 & 0 & \cdots & 0 \\ 0 & \sigma_2 & \cdots & 0 \\ \vdots & \vdots & \ddots & \vdots \\ 0 & 0 & \cdots & \sigma_m \end{bmatrix}, \tag{2.18}$$

and $\sigma_1 \geq \sigma_2 \geq \cdots \geq \sigma_m \geq 0$ (ZHOU; DOYLE, 1998). The fact that matrices $\upsilon$ and $\mathbf{V}$ are unitary means that $\boldsymbol{\Upsilon}^{\dagger}\boldsymbol{\Upsilon} = \boldsymbol{\Upsilon}\boldsymbol{\Upsilon}^{\dagger} = \mathbf{V}^{\dagger}\mathbf{V} = \mathbf{V}\mathbf{V}^{\dagger} = \mathbf{I_n}$, where $\mathbf{I_n}$ is the $n \times n$ identity matrix.

One interesting fact about this decomposition is that it is possible to demonstrate that $\|\mathbf{A}\| = \sigma_1$. Therefore, the 2-norm of a matrix can be calculated as its largest singular value (ZHOU; DOYLE, 1998). However, since we defined that the induced norm of a matrix is a measure of how much it can stretch (or compress) a vector, it is clear that the SVD might be an indicator of how this matrix can stretch or compress vectors in determined directions. Indeed, note that (2.17) can be re-written as

$$\mathbf{AV} = \boldsymbol{\Upsilon}\boldsymbol{\Sigma},$$

$$\mathbf{A}\begin{bmatrix}\mathbf{v}_1 & \mathbf{v}_2 & \cdots & \mathbf{v}_n\end{bmatrix} = \begin{bmatrix}\boldsymbol{\upsilon}_1 & \boldsymbol{\upsilon}_2 & \cdots & \boldsymbol{\upsilon}_m\end{bmatrix}\begin{bmatrix}\sigma_1 & 0 & \cdots & 0\\ 0 & \sigma_2 & \cdots & 0\\ \vdots & \vdots & \ddots & \vdots\\ 0 & 0 & \cdots & \sigma_m\end{bmatrix}. \tag{2.19}$$

Therefore, for $i = 1,2,\ldots,m$ we have that

$$\mathbf{A}\mathbf{v}_i = \sigma_i\boldsymbol{\upsilon}_i. \tag{2.20}$$

Since $\mathbf{v}_i$ and $\boldsymbol{\upsilon}_i$ are unit vectors, we have that the matrix multiplication $\mathbf{A}$ is stetching vector $\mathbf{v}_i$ by $\sigma_i$. Note that $\mathbf{v}_i$ and $\boldsymbol{\upsilon}_i$ are not necessarily colinear and, therefore, the matrix multiplication $\mathbf{A}$ can also rotate vector $\mathbf{v}_i$. But what is important to note here is that the singular vector $\mathbf{v_1}$ is the direction that will have the largest stretching or the smallest compression, while $\mathbf{v_n}$ is the direction that will have the smallest stretching or largest compression (ZHOU; DOYLE, 1998). In an input/output perspective, an input in the direction of $\mathbf{v_1}$ will have the largest gain, while an input in the direction of $\mathbf{v_n}$ will have the smallest one. This can be very helpful when deciding for controlling inputs and controlled variables.

## 2.2 NON-LINEAR SYSTEMS

The field of dynamical systems is ancient and its origins can be traced to the time when Newton invented calculus and studied motion problems (STROGATZ, 2018). Since then, the field has experienced tremendous growth, and many different problems arose, such as chaos. Here, however, the scope will be limited to a very interesting topic on dynamical systems. In fact, non-linear systems are rather common and virtually everything exhibit a behavior that can be expressed by a non-linear equation. Even components that are called linear are only considered to be so in a specific domain of validity. Moreover, linear systems can be seen as a very special case of non-linear systems and, therefore, it is indispensable to dedicate a short part of this chapter to the latter.

In order to limit the scope of this work even further, it is necessary to point out that this thesis is mainly concerned with systems described by differential equations rathern than by iterated maps (also called difference equations)(STROGATZ, 2018). Moreover, for the phenomena that will be investigated, there is no need to cover the concepts related to partial differential equations and, therefore, this thesis will be concerned only with ordinary equations, dealing with only one independent variable.

As it was previously mentioned, many devices that are commonly studied using linear dynamics are, in fact, non-linear. The power electronic devices studied in this thesis are not an exception and this fact will be shown later. A non-linear system can be described as a finite set of coupled first-order ordinary differential equations (KHALIL; GRIZZLE, 2002) as shown below.

$$\begin{aligned}
\dot{x}_1(t) &= f_1\left(x_1(t),x_2(t),\ldots,x_n(t),u_1(t),u_2(t),\ldots,u_r(t),t\right),\\
\dot{x}_2(t) &= f_2\left(x_1(t),x_2(t),\ldots,x_n(t),u_1(t),u_2(t),\ldots,u_r(t),t\right),\\
&\vdots \qquad \vdots \qquad\qquad\qquad \vdots\\
\dot{x}_n(t) &= f_n\left(x_1(t),x_2(t),\ldots,x_n(t),u_1(t),u_2(t),\ldots,u_r(t),t\right).
\end{aligned} \tag{2.21}$$

This set of equations can be further simplified into a more compact version, as it is described below.

$$\dot{\mathbf{x}}(t) = \mathbf{f}\left(\mathbf{x},\mathbf{u},t\right), \tag{2.22}$$

where

$$\mathbf{x}(t) = \begin{bmatrix} x_1(t) \\ x_2(t) \\ \vdots \\ x_n(t) \end{bmatrix} \qquad \mathbf{u}(t) = \begin{bmatrix} u_1(t) \\ u_2(t) \\ \vdots \\ u_r(t) \end{bmatrix} \qquad \mathbf{f}\left(\mathbf{x},\mathbf{u},t\right) = \begin{bmatrix} f_1\left(\mathbf{x},\mathbf{u},t\right) \\ f_2\left(\mathbf{x},\mathbf{u},t\right) \\ \vdots \\ f_n\left(\mathbf{x},\mathbf{u},t\right) \end{bmatrix}$$

Note that the elements of the $n \times 1$ state vector $\mathbf{x}(t)$, i.e. $x_1(t),x_2(t),\ldots,x_n(t)$, are called state variables. The elements of the $r \times 1$ input vector $\mathbf{u}(t)$, i.e. $u_1(t),u_2(t),\ldots,u_r(t)$, are called input variables. The elements from the $n \times 1$ vector $\mathbf{f}$ are the non-linear functions that define the dynamic behavior of each state variable.

In (2.22), it is possible to observe an explicit dependency on the time variable $t$. A special case of this system would be the case where (2.22) only implicit depenedency on $t$. In that case the system is said to be autonomous and can be represented by the following equation.

$$\dot{\mathbf{x}}(t) = \mathbf{f}\left(\mathbf{x},\mathbf{u}\right). \tag{2.23}$$

Furthermore, it is also possible to consider systems that does not have any external forces acting on them. Or there might be a case where the vector $\mathbf{f}$ does not have an

explicit dependency on input variables. This means that the dynamic behavior of the state variables can be described by the state variables alone. This type of system is known as unforced system and can be represented as the equation below.

$$\dot{\mathbf{x}}(t) = \mathbf{f}\left(\mathbf{x}\right). \tag{2.24}$$

The reader must notice that the bold font was chosen to represent vector quantities while the normal font was chosen to represent scalar values. In addition to that, this work is mainly concerned with autonomous systems and, therefore, a special attention is given to equations (2.23) and (2.24).

### 2.2.1 **Equilibrium and Stability**

The concept of equilibrium point is very important when studying dynamical systems. In an unforced autonomous system, a vector $\mathbf{x}^*$ is said to be the equilibrium if the following equation is true (KHALIL; GRIZZLE, 2002).

$$\mathbf{f}\left(\mathbf{x}^*\right) = \mathbf{0}. \tag{2.25}$$

The underlaying concept here is that if the system starts at point $\mathbf{x}^*$, it will remain at $\mathbf{x}^*$ for any $t > 0$. Many nonlinear systems exhibit more than one equilibrium points and they can have different properties regarding stability. Now, consider that $\mathbf{x}^*$ is an equilibrium point and that $\mathbf{x}^\dagger$ is a point in the vicinity of $\mathbf{x}^*$. In fact, consider it as close to $\mathbf{x}^*$ as desired. If the dynamical system is started in $\mathbf{x}^\dagger$ and $\mathbf{x}^*$ is a stable equilibrium point, the trajectory of the dynamical system will converge to a region near $\mathbf{x}^*$. On the other hand, if $\mathbf{x}^*$ is an unstable equilibrium point, the trajectory of the dynamical system is likely to diverge from $\mathbf{x}^*$.

The reader must notice that any system with state variables $\mathbf{x}$ can have its variable changed in order to shift the equilibrium point $\mathbf{x}^*$ to the origin $\mathbf{0}$. This will facilitate the understanding of the concepts related to stability and they do not constitute any loss of generality of the concepts described here (KHALIL; GRIZZLE, 2002). In fact, note that if $\bar{\mathbf{x}} = \mathbf{x} - \mathbf{x}^*$, then

$$\dot{\bar{\mathbf{x}}}(t) = \dot{\mathbf{x}}(t) - \dot{\mathbf{x}}^*(t) = \mathbf{f}(\mathbf{x}) - \mathbf{0} = \mathbf{f}(\mathbf{x}) = \dot{\mathbf{x}}(t). \tag{2.26}$$

Therefore, it is more convenient to study the stability of the origin $\mathbf{x} = \mathbf{0}$ than of a particular point $\mathbf{x} = \mathbf{x}^*$. Furthermore, the concept of stability related to the equilibrium point can be formalized as it is done in (KHALIL; GRIZZLE, 2002). Based on this reference, the equilibrium point $\mathbf{x} = \mathbf{0}$ is

- said to be stable if, for each $\varepsilon > 0$, there exists $\delta(\varepsilon) > 0$ such that

$$\|\mathbf{x}(t_0)\| < \delta \Rightarrow \|\mathbf{x}(t)\| < \varepsilon, \quad \forall t \geq 0, \tag{2.27}$$

- said to be unstable if it is not stable,

In addition to that, the system descrbied above is said to be asymptotically stable if it is stable and $\delta$ can be chosen in such way that

$$\|\mathbf{x}(t_0)\| < \delta \Rightarrow \lim_{t\to\infty} \mathbf{x}(t) = \mathbf{0}. \tag{2.28}$$

This mans that the states' trajectory not only stay in the vicinity of $\mathbf{x}^* = \mathbf{0}$ but they converge to it.

### 2.2.2 **Lyapunov Stability**

Now that the definition of stability is stated, it is necessary to answer whether or not a system described by Eq. (2.24) is stable. In order to answer this question, it is important to understand the technique developed by Lyapunov to assess the stability of a system. In fact, the tehorem developed by Lyapunov show the sufficient conditions for an autonomous unforced system to be considered stable or not.

First, consider an autonomous unforced system described by Eq. (2.24) and with equilibrium at the origin $\mathbf{f}(\mathbf{x}^*) = \mathbf{0}$. In his theorem, Lyapunov's shows that a certain class of functions, $V(\mathbf{x}) : \mathcal{S} \mapsto \mathbb{R}$, can be used to determine the stability of such system (KHALIL; GRIZZLE, 2002). In this case, $\mathcal{S} \subset \mathbb{R}^n$ is a domain that contains the point $\mathbf{x}^*$ and $V(\mathbf{x})$ is continuously differentiable. In addition to that, $V(\mathbf{x})$ must be a function such that

$$V(\mathbf{0}) = 0, \tag{2.29}$$

and

$$V(\mathbf{x}) > 0, \quad \forall \mathbf{x} \in \mathcal{S} - \{\mathbf{0}\}. \tag{2.30}$$

Under the conditions stated on equations (2.29) and (2.30), we have that if

$$\dot{V}(\mathbf{x}) = \frac{\partial V}{\partial t} = \frac{\partial V}{\partial \mathbf{x}}\frac{d\mathbf{x}}{dt} = \frac{\partial V}{\partial \mathbf{x}}\mathbf{f}(\mathbf{x}) \leq 0 \text{ in } \mathcal{S}, \tag{2.31}$$

then $\mathbf{x} = \mathbf{0}$ is stable. Furthermore, if

$$\dot{V}(\mathbf{x}) = \frac{\partial V}{\partial t} = \frac{\partial V}{\partial \mathbf{x}}\frac{d\mathbf{x}}{dt} = \frac{\partial V}{\partial \mathbf{x}}\mathbf{f}(\mathbf{x}) < 0 \text{ in } \mathcal{S} - \{\mathbf{0}\}, \tag{2.32}$$

then $\mathbf{x} = \mathbf{0}$ is asymptotically stable. In this work, we are not going to be worried about the proof of this theorem, but the interested reader can find it in (KHALIL; GRIZZLE, 2002).

Now, let us try to understand what the theorem is actually saying. It first states that a real-valued function $V(\mathbf{x})$ that is calculated using the state vector $\mathbf{x}$ of the dynamic system should have value 0 in the origin, which is where we defined our equilibirium, and should have positive values everywhere else. In addition to that, the derivative of $V(\mathbf{x})$ must have a non-positive value for the system to be considered stable or a strict negative value, everywhere but the origin, for the system to be considered asymptotically stable. So, Lyapunov's theorem is actually showing that to determine the stability of a system, it is necessary to design and test functions $V(\mathbf{x})$ to meet the sufficient conditions that will imply in stability or asymptotical stability.

Assessing one system's properties using another function, might be really counterintuitive to some. However, the function $V$ can, many times, be intuitively interpreted as the energy of the system that is being studied. In that case, note that the energy might be set to be the reference value in the equilibrium point and, therefore, it should be positive everywhere else. In addition to that, if the energy of the unforced autonomous system does not increase over time, it means that it is bounded and that the system is stable. Moreover, if the energy decreases over time, it means that the system is asymptotically stable. Of course, this is view is just a raw simplification of what is behind Lyapunov's theorem, but it might help us understand some other fundamental concepts described in this work.

### 2.2.3 **Linearization**

Although many important properties can be analyzed using the theory behind the study of dynamical systems, there are many more consolidated and robust tools developed for the study of linear systems. In fact, many artifacts from linear algebra simplify the analysis of systems with linear dynamics. Furthermore, the dynamics of nonlinear systems, under certain conditions, can be unambiguously mapped into a linear space. Therefore, the study of such nonlinear system can be simplified, what makes the linearization tool is of great interest.

First, consider the unforced autonomous system described by Eq. (2.24), continuously differentiable and that it has its equilibrium point at $\mathbf{x} = \mathbf{0}$. Then, because of the continuity property (KHALIL; GRIZZLE, 2002), we can write that exists a point $\mathbf{z}$ between the origin $\mathbf{0}$ and a general point $\mathbf{x}$, such that

$$\mathbf{f}(\mathbf{x}) - \mathbf{f}(\mathbf{0}) = \left.\frac{\partial \mathbf{f}}{\partial \mathbf{x}}\right|_{\mathbf{x}=\mathbf{z}} (\mathbf{x} - \mathbf{0}) \,. \tag{2.33}$$

However, since $\mathbf{x} = \mathbf{0}$ is the equilibrium, $\mathbf{f}(\mathbf{0}) = \mathbf{0}$ and, therefore,

$$\mathbf{f}(\mathbf{x}) = \left.\frac{\partial \mathbf{f}}{\partial \mathbf{x}}\right|_{\mathbf{x}=\mathbf{z}} \mathbf{x}. \tag{2.34}$$

In addition, notice that Eq. (2.34) can be re-written as

$$\mathbf{f}(\mathbf{x}) = \left.\frac{\partial \mathbf{f}}{\partial \mathbf{x}}\right|_{\mathbf{x}=\mathbf{0}} \mathbf{x} + \left( \left.\frac{\partial \mathbf{f}}{\partial \mathbf{x}}\right|_{\mathbf{x}=\mathbf{z}} - \left.\frac{\partial \mathbf{f}}{\partial \mathbf{x}}\right|_{\mathbf{x}=\mathbf{0}} \right) \mathbf{x}. \tag{2.35}$$

The first term of the right-hand side of Eq. (2.35) can be defined as

$$\left.\frac{\partial \mathbf{f}}{\partial \mathbf{x}}\right|_{\mathbf{x}=\mathbf{0}} \mathbf{x} = \mathbf{A}, \tag{2.36}$$

where $\mathbf{A}$ is a $n \times n$ matrix. The second term of the right-hand side of Eq. (2.35) can be written as

$$\left( \left.\frac{\partial \mathbf{f}}{\partial \mathbf{x}}\right|_{\mathbf{x}=\mathbf{z}} - \left.\frac{\partial \mathbf{f}}{\partial \mathbf{x}}\right|_{\mathbf{x}=\mathbf{0}} \right) \mathbf{x} = \mathbf{g}(\mathbf{x}). \tag{2.37}$$

In (KHALIL; GRIZZLE, 2002), it is shown that $\mathbf{g}(\mathbf{x})$ tends to $\mathbf{0}$ when $\mathbf{x}$ approaches the origin. This suggests that, around the neighborhood of the equilibrium point, the nonlinear dynamics of the unforced autonomous system can be linearly represented as

$$\dot{\mathbf{x}}(t) = \mathbf{f}(\mathbf{x}) \approx \mathbf{A}\mathbf{x}. \tag{2.38}$$

A similar result can be obtained by using Taylor expansion of function $\mathbf{f}(\mathbf{x})$ around the equilibrium point (ÅSTRÖM; MURRAY, 2010). This is, in fact, a more common approach to what it was shown in this work. In addition to that, the Taylor expansion approach can be used to further extend the linearization process to forced autonomous systems, as the one described in Eq. (2.23) (ÅSTRÖM; MURRAY, 2010). This process is known as Jacobian linearization and yields the following approximation around the origin.

$$\dot{\mathbf{x}}(t) = \mathbf{f}(\mathbf{x},\mathbf{u}) \approx \mathbf{A}\mathbf{x} + \mathbf{B}\mathbf{u}, \tag{2.39}$$

where $\mathbf{A}$ is the $n \times n$ matrix defined as

$$\mathbf{A} = \left.\frac{\partial \mathbf{f}}{\partial \mathbf{x}}\right|_{\mathbf{x}=\mathbf{0},\mathbf{u}=\mathbf{u}_{eq}}, \tag{2.40}$$

and $\mathbf{B}$ is the $n \times r$ matrix defined as

$$\mathbf{B} = \left.\frac{\partial \mathbf{f}}{\partial \mathbf{u}}\right|_{\mathbf{x}=\mathbf{0},\mathbf{u}=\mathbf{u}_{eq}}. \tag{2.41}$$

## 2.3 LINEAR SYSTEMS

We therefore have just shown that even nonlinear systems with complicated dynamics can be represented with linear equations under certain conditions. Now, let us analyze the characteristics of these special representations and the simplifications we achieve by working with linear systems. First, consider a linear system represented by

$$\dot{\mathbf{x}}(t) = \mathbf{A}\mathbf{x}(t) + \mathbf{B}\mathbf{u}(t), \tag{2.42}$$

where $\mathbf{A}$ is the $n \times n$ state matrix, $\mathbf{x}$ is the $n \times 1$ state vector, $\mathbf{B}$ is the $n \times r$ input matrix and $\mathbf{B}$ is the $r \times 1$ input vector. In addition, consider that $\mathbf{x}(0) = \mathbf{x}^*$. If the linear system is unforced, i.e. $\mathbf{u} = \mathbf{0}$, we can further simplify the system so it can be represented by an unforced linear system as described below.

$$\dot{\mathbf{x}}(t) = \mathbf{A}\mathbf{x}(t). \tag{2.43}$$

### 2.3.1 **Solution of Linear Systems**

In order to simplify our analysis, consider the dimension of our system to be $n = 1$. In this particular situation, Eq. (2.43) becomes

$$\dot{x}_1(t) = a_{11}x_1(t). \tag{2.44}$$

This differential equation has as solution

$$x_1(t) = x_1(0)e^{a_{11}t}, \tag{2.45}$$

where $e$ is Euler's number. Note that if $a_{11} \in \mathbb{R}$ is greater than zero, $x_1(t)$ grows indefinetely with time while if it is negative, the solution decays with time until it reaches zero. If $a_{11} \in \mathbb{C}$, then we have that our analysis should be done only for the real part of $a_{11}$. This solution can be easily verified because

$$\dot{x}_1(t) = \frac{d}{dt}\left(x_1(0)e^{a_{11}t}\right) = a_{11}x_1(0)e^{a_{11}t} = a_{11}x_1(t). \tag{2.46}$$

This approach is something that we can extend to look for the solution of (2.43). In fact, consider that

$$\mathbf{e}^{\mathbf{A}t} = \mathbf{I} + \mathbf{A}t + \frac{\mathbf{A}^2 t}{2} + \frac{\mathbf{A}^3 t}{6} + \cdots, \tag{2.47}$$

and note that

$$\frac{d}{dt}\mathbf{e}^{\mathbf{A}t} = \mathbf{A} + \mathbf{A}t + \frac{\mathbf{A}^2 t}{2} + \cdots = \mathbf{A}\left(\mathbf{I} + \mathbf{A}t + \frac{\mathbf{A}^2 t}{2} + \frac{\mathbf{A}^3 t}{6} + \cdots\right) = \mathbf{A}\mathbf{e}^{\mathbf{A}t}. \tag{2.48}$$

It is important to observe that, in fact, we have just shown in Eq. (2.48) that the expression in Eq. (2.47) is a candidate solution to the linear system in Eq. (2.43) (DERUSSO; CLOSE; ROY, 1990). Indeed, the solution to the latter is defined as

$$\mathbf{x}(t) = \mathbf{e}^{\mathbf{A}t}\mathbf{x}(0). \tag{2.49}$$

However, observe that if $\mathbf{A}$ is diagonal, then each state has an independent equation like the one presented in Equation (2.44) and, therefore, the matrix exponential can be calculated easily. In fact, note that we can use the eigenvalue decomposition to represent this linear system of differential equations as a diagonal system.

$$\dot{\mathbf{x}}(t) = \mathbf{A}\mathbf{x} = \mathbf{Q}\mathbf{\Lambda}\mathbf{Q}^{-1}\mathbf{x}. \tag{2.50}$$

We can multiply the equation above by $\mathbf{Q}^{-1}$ in the left to obtain

$$\mathbf{Q}^{-1}\dot{\mathbf{x}}(t) = \mathbf{\Lambda}\mathbf{Q}^{-1}\mathbf{x}. \tag{2.51}$$

Therefore, if $\mathbf{z} = \mathbf{Q}^{-1}\mathbf{x}(t)$, then we have that

$$\dot{\mathbf{z}}(t) = \mathbf{\Lambda}\mathbf{z}. \tag{2.52}$$

Note that each non-zero element of $\mathbf{\Lambda}$, i.e. an eigenvalue, is associated with one state of $\mathbf{z}$ and it is called a mode. Therefore, we can conduct a similar analysis to what was done for the scalar case, concluding that the eigenvalues of $\mathbf{A}$ would be crucial for determining the stability of linear systems. In fact, if all eigenvalues from $\mathbf{A}$ have their real part to be less than zero, then $\mathbf{A}$ is said to be Hurwitz (KHALIL; GRIZZLE, 2002; SONTAG, 2013; DULLERUD; PAGANINI, 2013; LIU; YAO, 2016).

### 2.3.2 Linear Systems Stability

Now that we have already discussed how to extract the linear representation of a dynamic system and analyzed how to calculate its solution, it is necessary to talk about the system's stability. In the previous section, we realized that there must be a relation between the eigenvalues of a matrix and stability of the system it represents. In order to understand this relation, let us try to check the stability of a linear system using a Lyapunov function. First, consider the existance of a symmetric matrix $\mathbf{P}$ such that

$$\mathbf{x}^\intercal\mathbf{P}\mathbf{x} > 0, \quad \forall\mathbf{x} - \{\mathbf{0}\}. \tag{2.53}$$

Matrix $\mathbf{P}$ would be then called positive definite. Now, suppose that

$$\mathbf{A}^\intercal\mathbf{P} + \mathbf{P}\mathbf{A} = -\mathbf{Y}, \tag{2.54}$$

where $\mathbf{Y}$ is positive semi-definite, i.e., $\mathbf{x}^\intercal\mathbf{Y}\mathbf{x} \geq 0$ for all $\mathbf{x} - \{\mathbf{0}\}$. If such matrix exists, then, it is possible to declare $V(\mathbf{x})$ such that

$$V(\mathbf{x}) = \mathbf{x}^\intercal\mathbf{P}\mathbf{x}. \tag{2.55}$$

Note that $V(\mathbf{x}) > 0$ for all $\mathbf{x} - \{\mathbf{0}\}$ and that $V(\mathbf{0}) = 0$. In addition, note that

$$\begin{aligned}\dot{V}(\mathbf{x}) = \frac{\partial V}{\partial t} &= \dot{\mathbf{x}}^\intercal\mathbf{P}\mathbf{x} + \mathbf{x}^\intercal\mathbf{P}\dot{\mathbf{x}} = (\mathbf{A}\mathbf{x})^\intercal\mathbf{P}\mathbf{x} + \mathbf{x}^\intercal\mathbf{P}(\mathbf{A}\mathbf{x}), \\ &= \mathbf{x}^\intercal(\mathbf{A}^\intercal\mathbf{P} + \mathbf{P}\mathbf{A})\mathbf{x} = -\mathbf{x}^\intercal\mathbf{Y}\mathbf{x}.\end{aligned} \tag{2.56}$$

Therefore, we have that $\dot{V}(\mathbf{x}) \leq 0$ and that the unforced linear system is stable by Lyapunov's conditions (KHALIL; GRIZZLE, 2002; SONTAG, 2013; DULLERUD;

PAGANINI, 2013; LIU; YAO, 2016). Note that if $\mathbf{Y}$ is positive definite, then $\dot{V}(\mathbf{x}) < 0$ and the system is considered to be asymptotically stable. This result means that in the case of linear systems we can try to find a positive definite matrix $\mathbf{P}$ instead of looking for a specific Lyapunov function $V(\mathbf{x})$.

In addition to that, it is possible to find many equivalent statements to the existence of such matrix $\mathbf{P}$, given a certain linear system characterized by state matrix $\mathbf{A}$(KHALIL; GRIZZLE, 2002; SONTAG, 2013; DULLERUD; PAGANINI, 2013; LIU; YAO, 2016). However, the most interesting one is that

$$\mathbf{A} \text{ is Hurwitz } \Leftrightarrow \exists\ \mathbf{P} \succ 0, \text{ such that } \mathbf{A}^{\intercal}\mathbf{P} + \mathbf{P}\mathbf{A} \prec 0, \tag{2.57}$$

where the relation $\succ 0$ is true for a positive definite matrix, while $\prec 0$ is true for a negative definite matrix. This means that, if $\mathbf{A}$ is Hurwitz, we can find some Lyapunov function using $\mathbf{P}$ that proves the system stability. Therefore, we can verify linear systems' stability just by studying the eigenvalues of their state matrix.

## 2.4 PERTURBATION THEORY AND AVERAGING TECHNIQUE

Up to now, this work covered how to find all necessary attributes to verify the equilibrium and stability of non-linear and linear systems. It is important to understand that the previous analysis is based upon the assumption that a perfect model of a system can be unequivocally obtained and that the analytical solutions for these dynamical systems are easy to find. However, this is not the case (or required) in practical problems. In fact, models and even controllers are simplified and analytical solutions can be approximated in order to facilitate complex analyses in the real world.

Although, it is necessary to highlight that simplifications and approximations can be done with the adequate mathematical rigor. As a matter of fact, there are important analytical theorems behind the approximations based on what is asymptotic method (KHALIL; GRIZZLE, 2002). The asymptotic method is the underlying concept for the perturbation method and the averaging technique that are discussed in this section and it is thoroughly studied in (SANDERS; VERHULST; MURDOCK, 2007).

The main goal in this section is to introduce us to techniques that allow us to:

**i.** approximate the solution of a differential equation describing a switching dynamical system;

**ii.** draw important conclusions about the equilibrium and the stability of a switching dynamical system by analyzing the equilibrium and the stability of its averaged system.

This section, is therefore, extremely important in modeling and designing efficient control systems for high-frequency switching devices such as the voltage-sourced converter studied here. Hence, let us first have a brief introduction to the perturbation theory in order to understand and be ready to use the averaging technique.

### 2.4.1 Perturbation Theory

Suppose a non-autonomous dynamic system described by Equation (2.58).

$$\dot{\mathbf{x}}(t) = \mathbf{f}(\mathbf{x},t,\varepsilon), \tag{2.58}$$

where $\varepsilon$ is a *small* parameter, $\mathbf{x}(t_0) = \eta(\varepsilon)$ and $f : \mathbb{R}^n \times \mathbb{R}^+ \times [-\varepsilon_0,\varepsilon_0] \mapsto \mathbb{R}^n$ is a piece-wise continuous function. The latter condition is important to this study since we are dealing with power electronic switching devices.

The perturbation method aims to approximate the solution of the system described in (2.58) depending on how small the parameter $\varepsilon$ is. In fact, if $\varepsilon = 0$, we have

$$\dot{\mathbf{x}}(t) = \mathbf{f}(\mathbf{x},t,0), \quad \text{and} \quad \mathbf{x}(t_0) = \eta(0) = \boldsymbol{\eta_0}. \tag{2.59}$$

Suppose now that the unperturbed system described in (2.59) has a unique solution $\mathbf{x}_0(t)$ for all $t$ in the time interval $[t_0,t_1]$. Then, there exists $\varepsilon < \varepsilon_0$ and a positive constant $\kappa$ such that (KHALIL; GRIZZLE, 2002):

$$\|\mathbf{x}(t,\varepsilon) - \mathbf{x}_0(t)\| \leq \kappa|\varepsilon|, \ \forall t \in [t_0,t_1]. \tag{2.60}$$

As one can easily see, an error between the solution of the perturbed system and the solution of the unperturbed system can be obtained. Furthermore, it is important to highlight that, although we do not know the value of $\kappa$, we know that for a sufficiently small $|\varepsilon|$, the product $\kappa|\varepsilon|$ will be small enough.

Furthermore, it is of great interest to create better approximations of the solution $\mathbf{x}(t,\varepsilon)$ to reduce the error to fit into a desirable tolerance, independently of the value of $\varepsilon$. In fact, it is possible to show that, under the conditions assumed for the system in Equation (2.58) and supposing that $\eta(\varepsilon)$ and its $N$ first derivatives are continuous over the interval $[-\varepsilon_0,\varepsilon_0]$, an approximation can be derived by using a finite expansion of the Taylor series (KHALIL; GRIZZLE, 2002), as shown in (2.61). Note that the first term of the right-hand side of Equation (2.61) denotes the approximation for solution $\mathbf{x}(t,\varepsilon)$, while the second term, $\mathbf{R_x}$, denotes the remainder of the approximation (KHALIL; GRIZZLE, 2002).

$$\mathbf{x}(t,\varepsilon) = \sum_{k=0}^{N-1} \mathbf{x_k}(t)\varepsilon^k + \varepsilon^N \mathbf{R_x}(t,\varepsilon), \ \forall t \in [t_0,t_1]. \tag{2.61}$$

Moreover, it is possible to show that there exists $\varepsilon \in [-\varepsilon_0,\varepsilon_0]$, such that the error of the approximation will be bounded by the term shown in Equation (2.62) (KHALIL; GRIZZLE, 2002).

$$\left\| \mathbf{x}(t,\varepsilon) - \sum_{k=0}^{N-1} \mathbf{x_k}(t)\varepsilon^k \right\| \leq \kappa|\varepsilon|^N, \ \forall t \in [t_0,t_1]. \tag{2.62}$$

For a practical engineering problem, one may ask what is the real benefit of calculating an approximate solution instead of finding the exact analytical solution of the system in (2.58). The answer for this question lies in how much work it is necessary to create a good approximation. The approximate solution will be effective if a small order for the Taylor series approximation results in a small error and/or if the approximated solution is considerably simpler than the original solution, $\mathbf{x}(t,\varepsilon)$ (KHALIL; GRIZZLE, 2002).

The perturbation theory is much more dense than what was presented here. However, the important concept for this study, is the fact that approximations for solutions can be derived with mathematical rigor. It is also important for the reader to note that the Taylor approximation shown in Equation (2.61) and the error bound shown in (2.62) are valid for all $t$ in the time interval $[t_0,t_1]$. This means that, from what was shown in this study, stability of the approximated solution will not imply in the stability of the exact solution. This is because there is no guarantee that the error bound will be valid for all $t$ in $\mathbb{R}^+$, and therefore, there is no guarantee that the convergence of the approximated solution will imply in the convergence of the original solution $\mathbf{x}(t,\varepsilon)$ to a neighborhood of the stable equilibrium point of the approximated solution. This problem will be further discussed in the next subsection.

### 2.4.2 **Averaging**

The averaging method has many applications in the study of complex dynamical systems, and thus, it is the object of study of many papers and books. The technique is commonly applied to dynamical systems that can be written in the following *standard form* (KHALIL; GRIZZLE, 2002; SANDERS; VERHULST; MURDOCK, 2007):

$$\dot{\mathbf{x}}(t) = \varepsilon\mathbf{f}(\mathbf{x},t,\varepsilon), \ \ 0 < \varepsilon \ll 1, \ \ \mathbf{x}(t_0) = \mathbf{x_0}, \tag{2.63}$$

where $f(\mathbf{x},t,\varepsilon)$ is a continuous and $T$-periodic function, meaning that

$$\mathbf{f}(\mathbf{x},t,\varepsilon) = \mathbf{f}(\mathbf{x},t+T,\varepsilon). \tag{2.64}$$

Note that the periodicity condition is related to the function itself and not to the variables of the function. In addition, it is important to note that, in the *standard form*, the function $\mathbf{f}(\mathbf{x},t,\varepsilon)$ should be continuous. However, important results are obtained

for piece-wise continuous functions in (MEERKOV, 1973) which are verified for power electronic converters in (KREIN *et al.*, 1990).

The averaging method will approximate the original solution of the system, say $\mathbf{x}(t)$, by averaging the function $\mathbf{f}(\mathbf{x},t,\varepsilon)$ at $\varepsilon = 0$, with respect to time $t$ (KHALIL; GRIZZLE, 2002; SANDERS; VERHULST; MURDOCK, 2007). In order to do so, it is necessary to introduce the average operator, that will be used in the right-hand side of Equation (2.63). The average equation can be defined as

$$\mathbf{f_{av}}(\mathbf{x}) = \frac{1}{T}\int_{t-T}^{t} \mathbf{f}(\mathbf{x},\tau,0)d\tau. \tag{2.65}$$

Note that if the average operation is defined as a limit with $T$ tending to infinity, there is no need for function $\mathbf{f}$ to be periodic. The new averaged system can then be defined as the following autonomous system

$$\frac{d}{dt}\bar{\mathbf{x}}(t) = \varepsilon \mathbf{f_{av}}(\bar{\mathbf{x}}), \;\; \bar{\mathbf{x}}(0) = \mathbf{x_0}. \tag{2.66}$$

Hence, as in a specific closed interval of time, it is possible to show the following statement (MEERKOV, 1973; SETHNA; MORAN, 1968).

$$\lim_{\varepsilon \longrightarrow 0} \|\mathbf{x}(t,\varepsilon) - \bar{\mathbf{x}}(t)\| = 0, \, \forall t \in \left[t_0, \frac{\kappa}{\varepsilon}\right], \tag{2.67}$$

for any positive constant $\kappa$. This result is not going to be proven here but the interested reader is referred to Theorem 1.3 in (MEERKOV, 1973) and Theorem A in (SETHNA; MORAN, 1968). Notice that the previous result is an extension of Equations (2.60) and (2.62). It is very important to observe that, as it is shown in Corollary 1.2 of Theorem 1.3 in (MEERKOV, 1973), when the parameter $\varepsilon$ tends to zero, the time interval where the limit is valid tends to $[t_0, +\infty)$. This is extremely important for the study developed in this work and this principle is going to be tested in Subseção 3.4.3. In fact, this result is used in (KREIN *et al.*, 1990) and in (SUN; GROTSTOLLEN, 1992) to show that the average solution of power-electronic-related systems will be arbitrarily close to the original solution if $\varepsilon$ is small enough.

In (KREIN *et al.*, 1990), the Krylov-Bogoliubov-Miltropolsky (KBM) generalized averaging approach is presented as an effective way to calculate a general approximation of the original solution, like the one shown in Equation (2.61), using the average function, in an iterative procedure. The KBM method can be used if better approximations are needed for a fixed parameter $\varepsilon$. The method is based on the following change of variables

$$\mathbf{x}(t) = \bar{\mathbf{x}}(t) + \varepsilon \boldsymbol{\upsilon}_1(t,\bar{\mathbf{x}}) + \varepsilon^2 \boldsymbol{\upsilon}_2(t,\bar{\mathbf{x}}) + \cdots . \tag{2.68}$$

where functions $\upsilon$ are $T-$periodic. The dynamical system will then be describe by the following equation

$$\frac{d}{dt}\bar{\mathbf{x}}(t) = \varepsilon \mathbf{G}_1(\bar{\mathbf{x}}) + \varepsilon^2 \mathbf{G}_2(\bar{\mathbf{x}}) + \varepsilon^3 \mathbf{G}_3(\bar{\mathbf{x}}) + \cdots . \tag{2.69}$$

As it was shown in (2.62), the error for the approximation will be as small as desired by increasing the number of terms used. In this work, the KBM approach is used later in the averaging process for the voltage-sourced converter dynamic equation.

# 3 MODELING METHODOLOGY

This chapter presents the mathematical modeling of power electronic components and some important processes that are essential for their connection to the grid and stable operation. The following sections will describe mathematically how to model the studied converters, their switching behavior and modulation strategy, and, finally, the techniques used to synchronize power electronic converters to the grid. Theoretical concepts that are presented in Chapter 2 are used here for obtaining important mathematical models of the studied power electronic devices.

## 3.1 PULSE-WIDTH MODULATION

In current power applications there are many switching strategies commonly used. The pulse-width modulation, or PWM, is a one of the most common approach used to modulate gate triggering signal in power electronic devices. This subject is well discussed in many references such as (KASSAKIAN; SCHLECHT; VERGHESE, 1991; YAZDANI; IRAVANI, 2010; MOHAN; UNDELAND; ROBBINS, 2003; BACHA *et al.*, 2014; SUNTIO; MESSO; PUUKKO, 2017). In this section, the basic concepts of the Sinusoidal Pulse-Width Modulation (SPWM) are described, the relationship between modulation function and the average of the switching functions is obtained and, finally, the harmonic content of the PWM output is discussed.

### 3.1.1 **Basic Concepts**

The PWM is the switching strategy used in this work and it is fundamental for the development of the voltage-sourced converter's average model, covered in Subseção 3.4.3. The main principle of operation for a pulse-width modulation strategy can be observed in Figura 1. The *modulating* signal, $m(t)$, is compared with the *carrier* signal, $c(t)$ to produce the switching signals $s_1(t)$ and $s_4(t)$. The frequency of the carrier, also known as *switching frequency*, or $f_s$, is usually much higher than the rate of change of the modulating signal, $m(t)$ (YAZDANI; IRAVANI, 2010). It is important to note that the signal $m(t)$ does not need to be a sinusoidal function as depicted in Figure 1 and, in power electronic circuits, this signal is used as a control output (KASSAKIAN; SCHLECHT; VERGHESE, 1991; YAZDANI; IRAVANI, 2010). The carrier signal is a triangular wave in the PWM strategy used with a sinusoidal modulating signal.

The switching signals $s_1(t)$ and $s_4(t)$ are complementary to one another in order to avoid the short circuit of the DC side. These signals can be assigned to have Boolean values, such as *true* or *false* but it is rather usual to attribute integer values to their output, such as 1 for *true* and 0 for *false*. In practical circuits their output is converted into the proper gate voltages or currents levels that are necessary to turn a switch on

Figure 1 – Basic circuit for generating PWM switching signal.

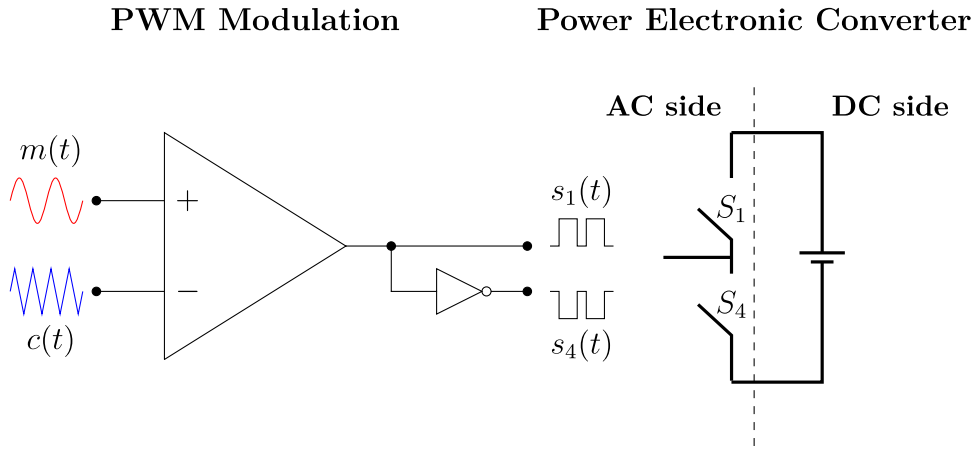


Source: Author (2022).

or off. Considering that $s_1(t)$ and $s_4(t)$ have integer outputs, it is possible to write the following equation to define them:

$$s_1(t) = \begin{cases} 1, \text{ if } m(t) \geq c(t), \\ 0, \text{ if } m(t) < c(t), \end{cases} \tag{3.1}$$

$$s_4(t) = \begin{cases} 0, \text{ if } m(t) \geq c(t), \\ 1, \text{ if } m(t) < c(t), \end{cases} \tag{3.2}$$

In order to illustrate the PWM concept, let us consider a triangular carrier $c(t)$ with frequency $f_s = 1200$ Hz and peak amplitude of 1 V and a sinusoidal modulation signal $m(t)$ as described in Equation 3.3 below.

$$m(t) = 0.9 \sin(2\pi 60t + 0.1) \text{ V}. \tag{3.3}$$

Note that the frequency of $c(t)$ is 20 times higher than the frequency, $f_m = 60$, of $m(t)$. If both signals, $c(t)$ and $m(t)$ were compared in a circuit like the one depicted in Figure 1, they would produce the switching signals $s_1(t)$ and $s_4(t)$ as shown in Figure 2. The curve in red is $m(t)$, while the triangular wave in blue is $c(t)$.

### 3.1.2 Average Over One Period

The average of the switching signals is crucial for the averaging of the power electronic devices, which is absolutely necessary for stability analysis and control design. The average is usually performed over one period of the triangular wave $c(t)$, and commonly called instantaneous average. First, let us consider the period of $c(t)$ depicted in Figure 3. Note that in the upper plot, curve $m(t)$, in red, is almost constant for the time where the inequality $c(t) > m(t)$ holds. This approximation occurs only if the carrier frequency, $f_s$, is large if compared to the modulating signal frequency. Suppose that $c(t) > m(t)$ is

Figure 2 – PWM signal originated by comparing $c(t)$ and $m(t)$.

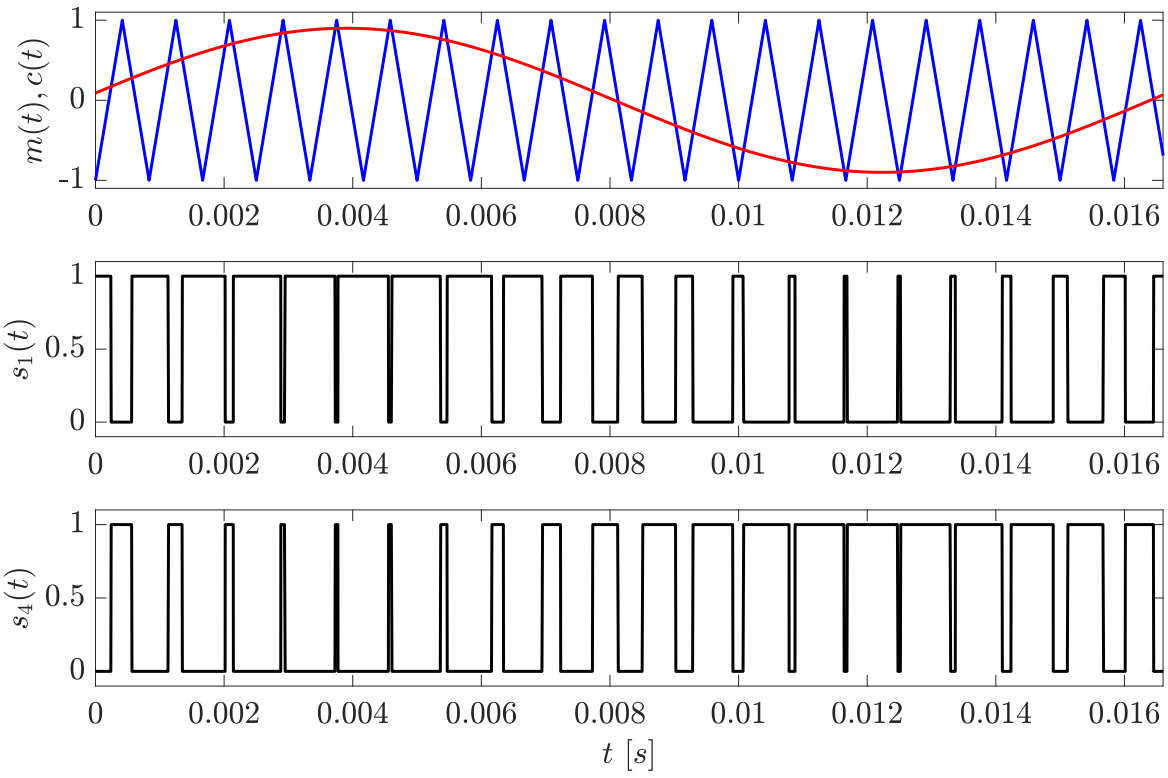


Source: Author (2022).

true for $(1-d)T_s$, where $T_s$ is the period of $c(t)$. The comparison of $m(t)$ with $c(t)$ would result in $s_1(t)$ and $s_4(t)$ shown in central and bottom plots from Figure 3.

Note that, over one period of $c(t)$, $s_1(t)$ is one for $dT_s$, while $s_4(t)$ is one for $(1-d)T_s$. Hence, if both switching functions are averaged over one period $T_s$, it is possible to obtain:

$$\int_t^{t+T_s} s_1(\tau)d\tau = \int_0^{dT_s} d\tau = dT_s, \tag{3.4}$$

$$\int_t^{t+T_s} s_4(\tau)d\tau = \int_0^{(1-d)T_s} d\tau = (1-d)T_s. \tag{3.5}$$

In addition, note that

$$\int_t^{t+T_s} \left[s_1(\tau) - s_4(\tau)\right] d\tau = \left[d-(1-d)\right] T_s = T_s(2d-1). \tag{3.6}$$

Now, let us try to establish a relation between the value of $m(t)$ and the value of $d$ based on triangle symmetry. Observe Figure 4, it was made based on Figure 3.

By triangle symmetry, we can write the following equation

$$\frac{V_{peak} - m(t)}{(1-d)Ts} = \frac{2V_{peak}}{T_s}, \tag{3.7}$$

that can be simplified into

$$m(t) = (2d-1)V_{peak}. \tag{3.8}$$

Figure 3 – Behavior of $m(t)$, $s_1(t)$ and $s_4(t)$ over one period of $c(t)$.

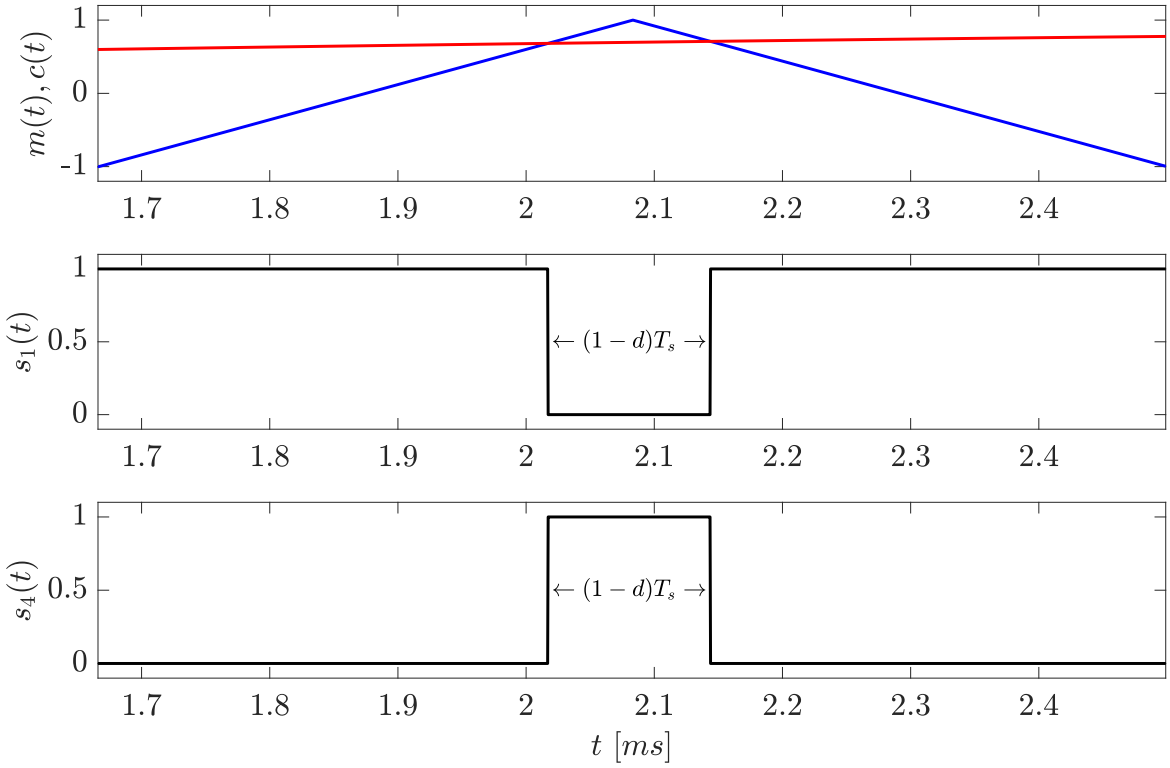


Source: Author (2022).

Figure 4 – Triangle symmetry for averaging switching functions over one period.

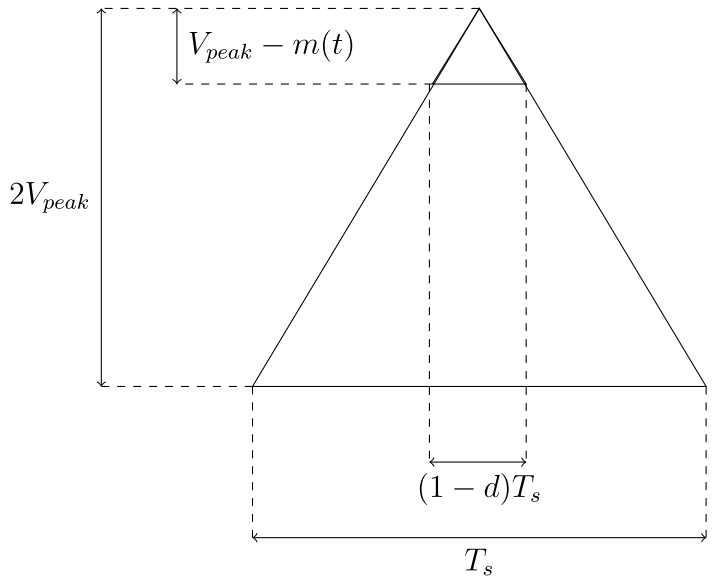


Source: Author (2022).

It is rather common to set the peak amplitude of the triangular wave to be $V_{peak} = 1$, just as the one seen in Figure 3. Hence, over each period $T_s$ of the carrier, it is possible to write that

$$m(t) = \frac{1}{T_s} \int_t^{t+T_s} [s_1(\tau) - s_4(\tau)]\, d\tau = 2d - 1. \tag{3.9}$$

The relation described in Equation (3.9) will be necessary to perform the averaging of the converter and to draw the relation between the switching functions $s_1(t)$, $s_4(t)$ and the control variable, which is the modulation index $m(t)$.

### 3.1.3 Harmonic Content of the Output

In order to analyze the harmonic content of the output determined by the PWM it is necessary to use Fourier Series. Consider the following function $v(t)$ as the output of a PWM switching strategy:

$$v(t) = s_1(t) - s_4(t). \tag{3.10}$$

This function $v(t)$, determined by the modulation index described in (3.3), has the behavior shown in Figure 5.

Figure 5 – Example of output voltage $v(t)$.

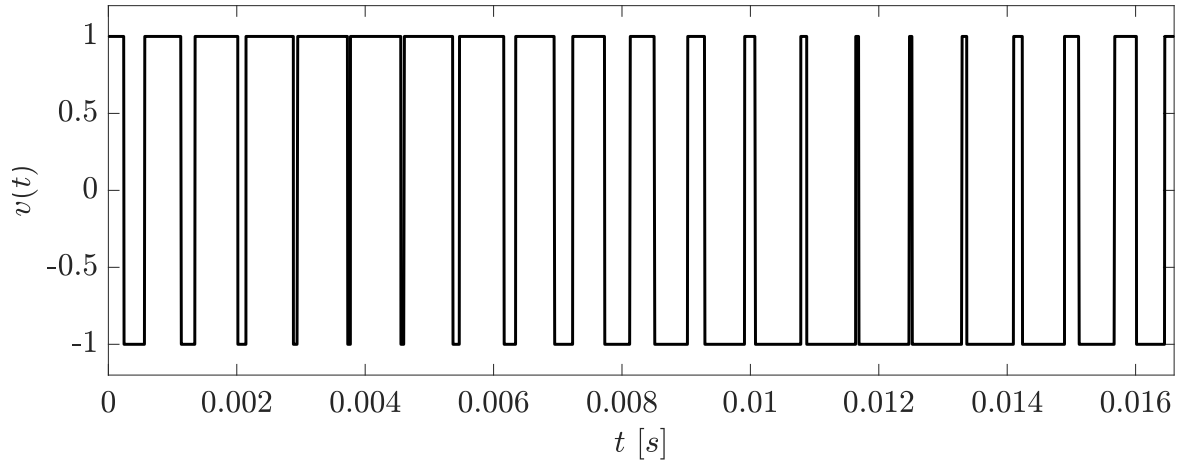


Source: Author (2022).

Recall that the modulation function has frequency $f_m$ while the carrier has a different fundamental frequency, $f_s$. The common Fourier analysis, however, can only describe functions with one fundamental frequency. Therefore, another type of approach is needed. In fact, the double Fourier series deals with that issue (BENNETT, 1933). Suppose a modulation function $m(t)$ as described in Equation (3.11) In addition, consider that the carrier wave has angular frequency $\omega_s$ and initial phase $\theta_c$.

$$m(t) = M \cos\left(\omega_m t + \theta_m\right). \tag{3.11}$$

Then, the double Fourier series associated with $v(t)$ described by (3.10) and generated with the modulation function (3.11) is given by equation (3.12) (BENNETT, 1933; BING; SUN, 2011).

$$v(t) = \overbrace{M\cos\left(\omega_m t + \theta_m\right)}^{v_1(t)} + \overbrace{\sum_{m=1}^{\infty}\left\{\frac{4}{m\pi}J_0\left(\frac{m\pi M}{2}\right)\cdot\sin\left(\frac{m\pi}{2}\right)\cdot\cos\left[m(\omega_s t+\theta_c)\right]\right\}}^{v_2(t)} + \underbrace{+\sum_{m=1}^{\infty}\sum_{n=\pm1}^{\pm\infty}\left\{\frac{4}{m\pi}J_n\left(\frac{m\pi M}{2}\right)\cdot\sin\left[\frac{(m+n)\pi}{2}\right]\cdot\cos\left[m(\omega_s t+\theta_c)+n(\omega_m t+\theta_m)\right]\right\}}_{v_3(t)} \tag{3.12}$$

where $J_n(x)$ are Bessel functions of the first type. Bessel functions are divided into two types, $J_n(x)$ and $Y_n(x)$. The first is known as Bessel function of the first type, while the latter is known as Bessel function of the second type. These function types are the linearly independent solution of the differential equation presented in Equation (3.13), where $n$ is a complex number (WATSON, 1944).

$$x^2\frac{d^2}{dx^2}f(x) + x\frac{d}{dx}f(x) + \left(x^2 - n^2\right)f(x) = 0. \tag{3.13}$$

The solution $f(x) = J_n(x)$ is presented in Equation (3.14), while some examples of that solution are presented in Figure 6. Note that $J_n(-x) = (-1)^n J_n(x)$ (WATSON, 1944).

$$J_n(x) = \frac{(j)^{-n}}{s\pi}\int_0^{2\pi} e^{j(x\cos\theta - n\theta)}d\theta. \tag{3.14}$$

Now, back on the output of the PWM, note that the Fourier series representation of $v(t)$, presented in Equation (3.12), has, essentially, three components. The first term, $v_1(t)$, represents the modulation signal, $m(t)$, that appears in the output voltage $v(t)$. The second term, $v_2(t)$, represents the harmonic content coming from the carrier wave component and its harmonics. The third and final term, $v_3(t)$, represents the harmonic content coming from side-band components. As an example, consider the modulation function described in Equation (3.3) and a carrier function with frequency $f_s = 1200$ Hz. The frequency spectrum of the PWM output $v(t)$ is shown in Figure 7. It is important to note that many of the side-band components have negligible value. In addition, it is important to observe that the PWM strategy induces the harmonic components to appear in very high frequencies, making it easy to filter them without altering the fundamental frequency component. This fact is one of the main reasons why the PWM strategy is very common in industry applications (BING; SUN, 2011).

Figure 6 – Example of Bessel functions of the first type for $n = 0$, $n = 1$, $n = 2$ and $n = 3$.

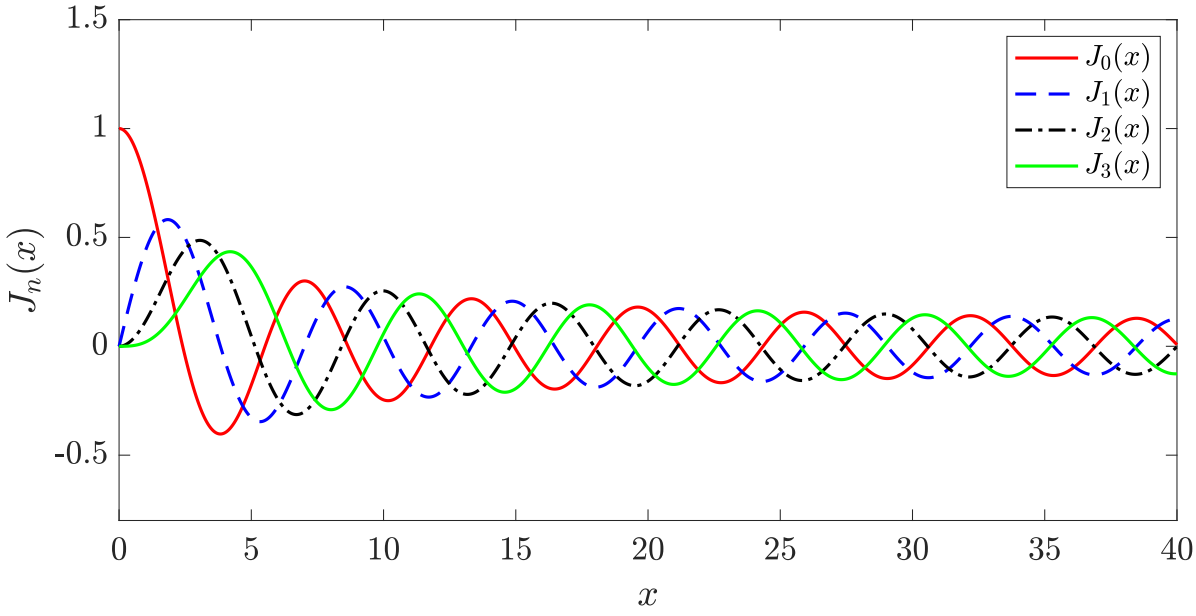


Source: Author (2022).

Figure 7 – Frequency spectrum of the PWM output.

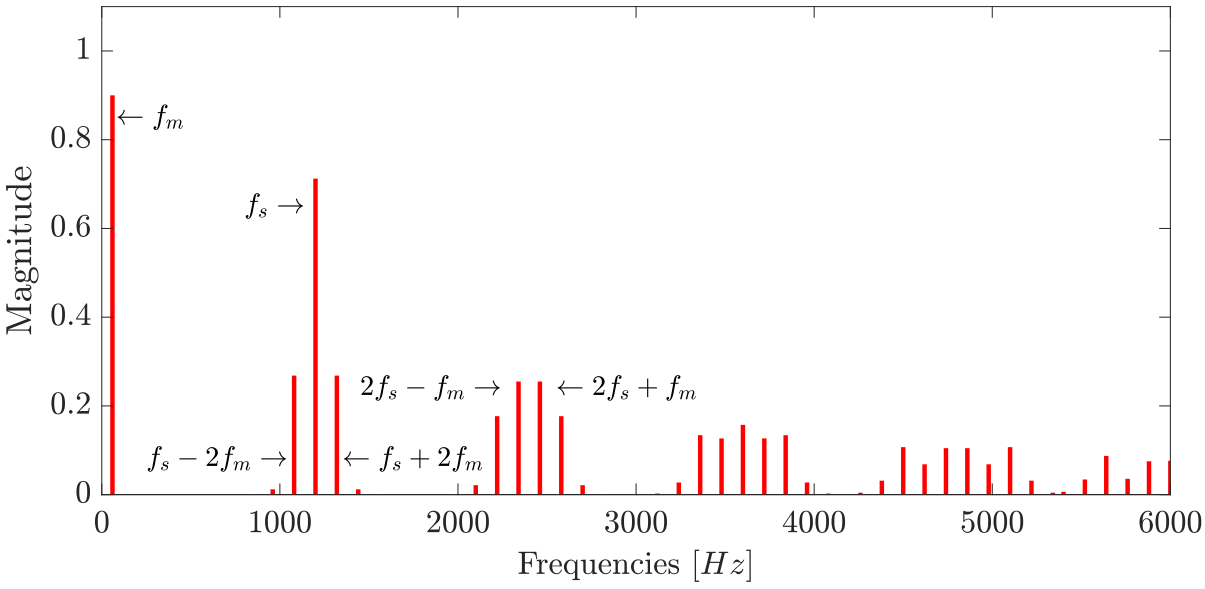


Source: Author (2022).

## 3.2 SPACE PHASOR AND REFERENCE FRAMES

This section discusses the modeling approach by using space phasor representation. This modeling strategy is well described in (YAZDANI; IRAVANI, 2010) and many things from this section can be found in that reference.

### 3.2.1 **Space Phasor**

The space-phasor approach is well suited for the simplification of three-phase system models (YAZDANI; IRAVANI, 2010). The main idea of the approach is to be able to reduce the number of equations describing the system and, therefore, simplify the control design required. This approach can be seen as linear transformation, mapping one function in $\mathbb{R}^3$ into one function in $\mathbb{C}$. In order to understand the mapping, let us consider a balanced three-phase quantity (current, voltage or even time-varying inductances) represented by Equation (3.15).

$$\begin{cases} h_a(t) = A\cos\left(\omega t + \theta_0\right), \\ h_b(t) = A\cos\left(\omega t + \theta_0 - \dfrac{2\pi}{3}\right), \\ h_c(t) = A\cos\left(\omega t + \theta_0 + \dfrac{2\pi}{3}\right), \end{cases} \tag{3.15}$$

where $A$ is the amplitude, $\omega$ is the variable's angular frequency and $\theta_0$ is the initial phase displacement. Note that variables $h_a(t)$, $h_b(t)$ and $h_c(t)$ have a phase displacement of $2\pi/3$ between themselves. The space phasor can be obtained by the following transformation matrix $\mathbf{T}_{sph} : \mathbb{R}^3 \mapsto \mathbb{C}$.

$$\mathbf{T}_{sph} = \frac{2}{3}\begin{bmatrix} e^{j0} & e^{j\frac{2\pi}{3}} & e^{-j\frac{2\pi}{3}} \end{bmatrix}, \tag{3.16}$$

where $e$ is the exponential function and $j$ is the notation of an imaginary number. It should be highlighted that the use of the constant $2/3$ ensures an amplitude invariant transformation. Thus, the space phasor can be represented by

$$\begin{aligned} \overrightarrow{h}(t) &= \mathbf{T_{sph}}\begin{bmatrix} h_a(t) \\ h_b(t) \\ h_c(t) \end{bmatrix} = \frac{2}{3}\begin{bmatrix} e^{j0} & e^{j\frac{2\pi}{3}} & e^{-j\frac{2\pi}{3}} \end{bmatrix}\begin{bmatrix} h_a(t) \\ h_b(t) \\ h_c(t) \end{bmatrix}, \\ \overrightarrow{h}(t) &= \frac{2}{3}\left[\underbrace{h_a(t)e^{j0}}_{g_a(t)} + \underbrace{h_b(t)e^{j\frac{2\pi}{3}}}_{g_b(t)} + \underbrace{h_c(t)e^{-j\frac{2\pi}{3}}}_{g_c(t)}\right]. \end{aligned} \tag{3.17}$$

Recalling the Euler representation for a sinusoidal function, it is possible to write

that:

$$\begin{cases} g_a(t) = \dfrac{A}{2}\left(e^{j\omega t}e^{j\theta_0} + e^{-j\omega t}e^{-j\theta_0}\right)e^{j0} = \dfrac{A}{2}\left(e^{j\omega t}e^{j\theta_0} + e^{-j\omega t}e^{-j\theta_0}\right), \\ g_b(t) = \dfrac{A}{2}\left(e^{j\omega t}e^{j\theta_0}e^{-j\frac{2\pi}{3}} + e^{-j\omega t}e^{-j\theta_0}e^{j\frac{2\pi}{3}}\right)e^{j\frac{2\pi}{3}} = \dfrac{A}{2}\left(e^{j\omega t}e^{j\theta_0} + e^{-j\omega t}e^{-j\theta_0}e^{-j\frac{2\pi}{3}}\right), \\ g_c(t) = \dfrac{A}{2}\left(e^{j\omega t}e^{j\theta_0}e^{j\frac{2\pi}{3}} + e^{-j\omega t}e^{-j\theta_0}e^{-j\frac{2\pi}{3}}\right)e^{-j\frac{2\pi}{3}} = \dfrac{A}{2}\left(e^{j\omega t}e^{j\theta_0} + e^{-j\omega t}e^{-j\theta_0}e^{j\frac{2\pi}{3}}\right). \end{cases} \tag{3.18}$$

Therefore, Equação 3.17 can be rewritten as

$$\begin{aligned} \overrightarrow{h}(t) &= \frac{2}{3}\left[g_a(t) + g_b(t) + g_c(t)\right], \\ &= \frac{2}{3}\left[3\frac{A}{2}e^{j\omega t}e^{j\theta_0} + 3\frac{A}{2}e^{-j\omega t}e^{-j\theta_0}\left(e^{j0} + e^{-j\frac{2\pi}{3}} + e^{j\frac{2\pi}{3}}\right)\right]. \end{aligned} \tag{3.19}$$

Recall that $e^{j0} + e^{-j\frac{2\pi}{3}} + e^{j\frac{2\pi}{3}} \equiv 0$. Thus, the space phasor representation of the system described in Equation 3.15, is:

$$\overrightarrow{h}(t) = \underbrace{Ae^{j\theta_0}}_{\underline{\mathrm{h}}}e^{j\omega t} = \underline{\mathrm{h}}e^{j\omega t}. \tag{3.20}$$

Note that $\underline{\mathrm{h}}$ is a complex number that can be interpreted as a phasor. In addition, it is important that the reader recall that

$$\underline{\mathrm{h}} = A\cos\theta_0 + jA\sin\theta_0. \tag{3.21}$$

Note that the original wave functions $h_a(t)$, $h_b(t)$ and $h_c(t)$, can be easily retrieved from the state phasor by using the following equation.

$$\begin{cases} h_a(t) = \Re\left\{\overrightarrow{h}(t)e^{j0}\right\}, \\ h_b(t) = \Re\left\{\overrightarrow{h}(t)e^{-j\frac{2\pi}{3}}\right\}, \\ h_c(t) = \Re\left\{\overrightarrow{h}(t)e^{j\frac{2\pi}{3}}\right\}. \end{cases} \tag{3.22}$$

Furthermore, it is crucial to describe how power is calculated in space phasors domain. In order to do so, consider a three-phase, three-wire system where $i_a(t) + i_b(t) + i_c(t) = 0$. In the space-phasor representation, instantaneous active, reactive and apparent powers are represented, respectively, by (YAZDANI; IRAVANI, 2010):

$$p(t) = \Re\left\{\frac{3}{2}\overrightarrow{v}(t)\overrightarrow{i}^{*}(t)\right\}, \tag{3.23}$$

$$q(t) = \Im\left\{\frac{3}{2}\overrightarrow{v}(t)\overrightarrow{i}^{*}(t)\right\}, \tag{3.24}$$

$$s(t) = p(t) + jq(t) = \frac{3}{2}\overrightarrow{v}(t)\overrightarrow{i}^{*}(t), \tag{3.25}$$

where the superscript $(^*)$ represents the complex conjugate.

### 3.2.2 Harmonic Representation on Space Phasors

Now, suppose that instead of Equation (3.15), the three-phase quantities are now represented with one additional harmonic component such as in Equation (3.26). Note that the harmonic component has its frequency equal to a multiple of the fundamental frequency $\omega$.

$$\begin{cases} h_a(t) = A\cos(\omega t + \theta_0) + A_n\cos(n\omega t), \\ h_b(t) = A\cos\left(\omega t + \theta_0 - \dfrac{2\pi}{3}\right) + A_n\cos\left(n\omega t - \dfrac{2n\pi}{3}\right), \\ h_c(t) = A\cos\left(\omega t + \theta_0 + \dfrac{2\pi}{3}\right) + A_n\cos\left(n\omega t + \dfrac{2n\pi}{3}\right). \end{cases} \tag{3.26}$$

If the transformation from Equation (3.16) is applied in (3.26), it is possible to obtain (3.27).

$$\overrightarrow{h}(t) = \underline{h}e^{j\omega t} + \overrightarrow{h}_n(t), \tag{3.27}$$

where

$$\overrightarrow{h}_n(t) = \frac{A_n}{3}g_1 e^{jn\omega t} + \frac{A_n}{3}g_2 e^{-jn\omega t}, \tag{3.28}$$

and

$$g_1 = 1 + e^{-j(n-1)\frac{2\pi}{3}} + e^{j(n-1)\frac{2\pi}{3}}, \tag{3.29}$$

$$g_2 = 1 + e^{j(n+1)\frac{2\pi}{3}} + e^{-j(n+1)\frac{2\pi}{3}}. \tag{3.30}$$

Note that the term $\frac{A_n}{3}g_1 e^{jn\omega t}$ rotates in counterclockwise direction while the term $\frac{A_n}{3}g_2 e^{-jn\omega t}$ rotates in clockwise direction. This is the reason why reference (YAZDANI; IRAVANI, 2010) names the first term "positive-sequence" and the second term "negative-sequence". Now note that:

- if $n = 3m + 1$, where $m = 1,2,\ldots$, it is possible to observe that $g_1 = 3$ and $g_2 = 0$. Hence, harmonics such as $4^{th}$, $7^{th}$, $10^{th}$, $13^{th}$, $16^{th}\ldots$ rotate in counterclockwise direction and, therefore, are considered "positive-sequence" harmonics;

- if $n = 3m + 2$, where $m = 0,1,2,\ldots$, it is possible to observe that $g_1 = 0$ and $g_2 = 3$. Hence, harmonics such as $2^{nd}$,$5^{th}$, $8^{th}$, $11^{th}$, $14^{th}$, $17^{th}\ldots$ rotate in clockwise direction and, therefore, are considered "negative-sequence" harmonics;

- and if $n = 3m$, where $m = 1,2,\ldots$, it is possible to observe that $g_1 = g_2 = 0$. Hence, harmonics such as $3^{th}$, $6^{th}$, $9^{th}$, $12^{th}$, $15^{th}\ldots$ do not rotate and, therefore, $\overrightarrow{h}_n(t) \equiv 0$ for those components.

In addition, note that the system presented in Equation (3.26) presents harmonics that are multiple from the fundamental frequency $\omega$. However, as it was seen in Section 3.1, PWM strategies induces harmonics to appear in multiples of the carrier's frequency and in its side-bands. Therefore, the space-phasor harmonic representation that was derived here is not well-suited for dealing with PWM-based switched models. Instead, the representation here can be of great advantage for modeling systems where harmonics which are multiple from the fundamental frequency appear.

### 3.2.3 $\alpha\beta$ - Frame Representation

The $\alpha\beta$-frame representation is focused on the fact that you can decompose the space phasor representation into two orthogonal waves. Therefore, the transformation matrix called $\mathbf{T}_{\alpha\beta}$ maps a function from $\mathbb{R}^3$ into another function at $\mathbb{R}^2$. Consider that

$$\overrightarrow{h}(t) = h_\alpha(t) + jh_\beta(t). \tag{3.31}$$

Therefore, we can write that

$$\begin{aligned} h_\alpha(t) + jh_\beta(t) &= \frac{2}{3}\begin{bmatrix} e^{j0} & e^{j\frac{2\pi}{3}} & e^{-j\frac{2\pi}{3}} \end{bmatrix}\begin{bmatrix} h_a(t) \\ h_b(t) \\ h_c(t) \end{bmatrix}, \\ h_\alpha(t) + jh_\beta(t) &= \frac{2}{3}\begin{bmatrix} 1 & \left(-\frac{1}{2} + j\frac{\sqrt{3}}{2}\right) & \left(-\frac{1}{2} - j\frac{\sqrt{3}}{2}\right) \end{bmatrix}\begin{bmatrix} h_a(t) \\ h_b(t) \\ h_c(t) \end{bmatrix}. \end{aligned} \tag{3.32}$$

By separating real and imaginary parts, it is possible to write that

$$\begin{bmatrix} h_\alpha(t) \\ h_\beta(t) \end{bmatrix} = \frac{2}{3}\overbrace{\begin{bmatrix} 1 & -\frac{1}{2} & -\frac{1}{2} \\ 0 & \frac{\sqrt{3}}{2} & -\frac{\sqrt{3}}{2} \end{bmatrix}}^{\mathbf{T}_{\alpha\beta}}\begin{bmatrix} h_a(t) \\ h_b(t) \\ h_c(t) \end{bmatrix}. \tag{3.33}$$

Since, functions $h_\alpha(t)$ and $h_\beta(t)$ are orthogonal, they can be represented through cosine and sine functions. Hence, define

$$A(t) = \sqrt{h_\alpha^2(t) + h_\beta^2(t)}, \tag{3.34}$$

and

$$\begin{cases} \cos\left(\theta(t)\right) &= \dfrac{h_\alpha(t)}{A(t)} = \dfrac{h_\alpha(t)}{\sqrt{h_\alpha^2(t) + h_\beta^2(t)}}, \\ \sin\left(\theta(t)\right) &= \dfrac{h_\beta(t)}{A(t)} = \dfrac{h_\beta(t)}{\sqrt{h_\alpha^2(t) + h_\beta^2(t)}}. \end{cases} \tag{3.35}$$

Therefore, it is possible to write that

$$\begin{cases} h_\alpha(t) &= A(t)\cos\left(\theta(t)\right), \\ h_\beta(t) &= A(t)\sin\left(\theta(t)\right). \end{cases} \tag{3.36}$$

It is important to highlight that if and only if the three-phase variable set $\{h_a(t),h_b(t),h_c(t)\}$ is balanced and free of harmonic components, $A(t)$ is a constant and $\theta(t)$ is a ramp function. As a consequence, the signals $h_\alpha(t)$ and $h_\beta(t)$ becomes orthogonal sinusoidal signals. Furthermore, according to (3.23) and (3.24), if a three-phase system is represented in its $\alpha\beta$-frame equivalent, the power can be represented by

$$p(t) = \frac{3}{2}\left[v_\alpha(t)i_\alpha(t) + v_\beta(t)i_\beta(t)\right], \tag{3.37}$$

$$q(t) = \frac{3}{2}\left[-v_\alpha(t)i_\beta(t) + v_\beta(t)i_\alpha(t)\right]. \tag{3.38}$$

### 3.2.4 *dq* - Frame Representation

In $dq$-frame representation, another mapping will be adopted. In this case, the reference frame rotates. The angular frequency is usually chosen to be equal to the fundamental frequency of the quantities $h_\alpha(t)$ and $h_\beta(t)$, reducing the the variability of the result. First, let us analyze how to obtain the $dq$-frame representation from $\alpha\beta$-frame. In this case, the transformation $R_{dq}[\varepsilon(t)]$ will map the functions $h_\alpha(t)$ and $h_\beta(t)$ from $\mathbb{R}^2$ back into $\mathbb{R}^2$, by using the following

$$h_d(t) + jh_q(t) = \overrightarrow{h}(t)e^{-j\varepsilon(t)} = \left[h_\alpha(t) + jh_\beta(t)\right]e^{-j\varepsilon(t)}, \tag{3.39}$$

where

$$\varepsilon(t) = \varepsilon_0 + \int_0^t \omega(\tau)d\tau. \tag{3.40}$$

Note that this mapping actually reduces the variability of the $\alpha\beta$-frame representation by rotating the reference axis with the factor $e^{-j\varepsilon(t)}$. By separating real and imaginary parts, we have that the transformation $\mathbf{R}_{dq}[\varepsilon(t)] : \mathbb{R}^2 \mapsto \mathbb{R}^2$ is represented by:

$$\begin{bmatrix} h_d(t) \\ h_q(t) \end{bmatrix} = \overbrace{\begin{bmatrix} \cos\varepsilon(t) & \sin\varepsilon(t) \\ -\sin\varepsilon(t) & \cos\varepsilon(t) \end{bmatrix}}^{\mathbf{R}_{dq}[\varepsilon(t)]} \begin{bmatrix} h_\alpha(t) \\ h_\beta(t) \end{bmatrix}. \tag{3.41}$$

If the transformation from Equation (3.33) is used in (3.41), the result will describe transformation $\mathbf{T}_{dq}[\varepsilon(t)]$ that maps from $\mathbb{R}^3$ to $\mathbb{R}^2$ as described below.

$$\begin{bmatrix} h_d(t) \\ h_q(t) \end{bmatrix} = \frac{2}{3}\overbrace{\begin{bmatrix} \cos\varepsilon(t) & \cos\left(\varepsilon(t) - \frac{2\pi}{3}\right) & \cos\left(\varepsilon(t) + \frac{2\pi}{3}\right) \\ \sin\varepsilon(t) & \sin\left(\varepsilon(t) - \frac{2\pi}{3}\right) & \sin\left(\varepsilon(t) + \frac{2\pi}{3}\right) \end{bmatrix}}^{\mathbf{T}_{dq}[\varepsilon(t)]} \begin{bmatrix} h_a(t) \\ h_b(t) \\ h_c(t) \end{bmatrix}. \tag{3.42}$$

In addition, note that

$$\mathbf{R}_{dq}[\varepsilon(t)]^{-1} = \mathbf{R}_{dq}[-\varepsilon(t)] = \mathbf{R}_{dq}^{\intercal}[\varepsilon(t)], \tag{3.43}$$

and

$$\mathbf{T}_{dq}[\varepsilon(t)]^{-1} = \mathbf{T}_{dq}[-\varepsilon(t)] = \mathbf{T}_{dq}^{\intercal}[\varepsilon(t)]. \tag{3.44}$$

Moreover, if $A(t)$ is defined as

$$A(t) = \sqrt{h_d^2(t) + h_q^2(t)}, \tag{3.45}$$

the $dq$ reference frame becomes

$$h_d(t) + jh_q(t) = A(t)e^{j(\theta_0 - \varepsilon_0)}. \tag{3.46}$$

Note that, if $\varepsilon_0$ is set to be equal to $\theta_0$, then $h_q(t) = 0$. Furthermore, the three-phase power represented in $dq$ reference frame is

$$p(t) = \frac{3}{2}\left[v_d(t)i_d(t) + v_q(t)i_q(t)\right], \tag{3.47}$$

$$q(t) = \frac{3}{2}\left[-v_d(t)i_q(t) + v_q(t)i_d(t)\right]. \tag{3.48}$$

Now, let us turn our attention back to $\varepsilon(t)$. This angle, which is described in Equation (3.40), varies with time and it is core principle of setting a rotating reference frame. In fact, there are different ways to set function $\varepsilon(t)$ depending on the application. For instance, in grid-connected converters, it is rather usual to set $\varepsilon(t)$ to be equal the grid angle $\theta(t) = \omega t + \theta_0$. When doing so, the active power, which is described in Equation (3.48), is proportional to $i_d(t)$ current while reactive power is proportional to $i_q(t)$. This will be explored in a further chapter of this work.

## 3.3 RESISTOR-INDUCTANCE BRANCHES

This section describes the modeling of resistor-inductance branches which are essential for the modelling of the converter's dynamic.

### 3.3.1 **Transformer**

The first resistor-inductance branch that need to be described is the transformer. A transformer is a very important device in a power system because it allows the connection of two AC subsystems with different voltage levels. A simple single-phase transformer is basically composed of two coils of copper wire wrapped around a single core made of magnetic material (CHAPMAN, 2005; KRAUSE *et al.*, 2002). The most famous single-phase transformer model is the Steinmetz model (STEINMETZ, 1895), which is represented by the circuit depicted in Figure 8.

Figure 8 – Single-phase transformer circuit from Steinmetz model.

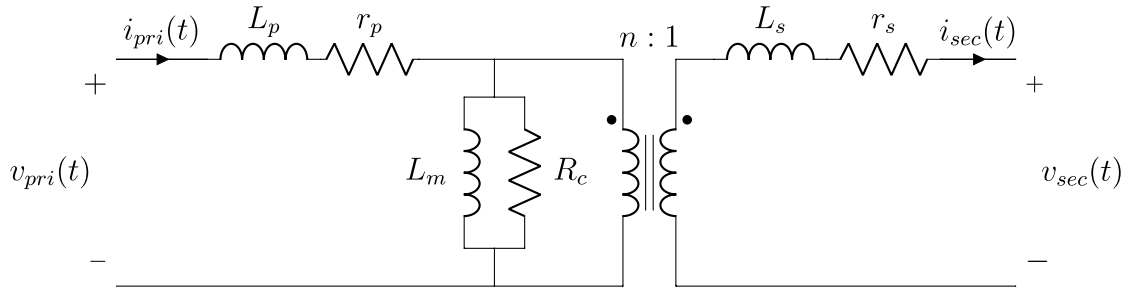


Source: Author (2022).

The transformer circuit is composed of inductances $L_p$ and $L_s$ that represent the leakage flux that does not flow through the core. Resistances $r_p$ and $r_s$ are placed to represent copper losses due to Joule effect on coil winding wires. The parallel branch, here called excitation branch, is made of two components connected in parallel, inductance $L_m$ and resistance $R_c$. The former is placed in the model in order to account for the effect of magnetizing the ferromagnetic core. The latter is a way to take into account core losses due to hysteresis and eddy currents. Finally, the ideal transformer performs the last connection to establish a relation between the the quantities in the primary and secondary side. A more detailed explanation for each component of this model can be found in (CHAPMAN, 2005).

Although the model is shown to be very accurate in many occasions, non-linearities are not taken into account. The non-linear behavior occurs in the components represented in the excitation branch and are basically due to the saturation of the ferromagnetic core. These effects are briefly described in (CHAPMAN, 2005), but are thoroughly examined in (ENRIGHT, 1996). However, the linear Steinmetz model is preferred for this work because saturation effects are not very meaningful for control design purposes.

In addition to neglecting the saturation effects happening in the ferromagnetic core, other aspects can be simplified. In fact, the excitation current, i.e. the current flowing through the excitation branch, is very small if compared to the current flowing to the ideal transformer. Therefore, the excitation branch can be omitted and the single-phase transformer becomes the system depicted in Figure 9 below.

Figure 9 – Single-phase transformer circuit without excitation branch.

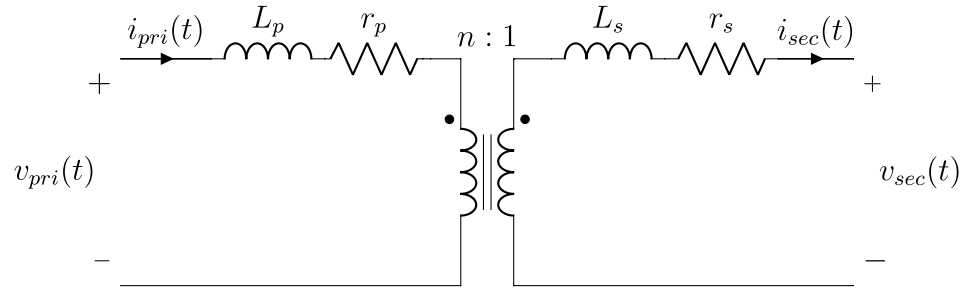


Source: Author (2022).

Furthermore, the inductor and resistor from the secondary side can be referred to the primary by using the transformer ratio. This will make the single-phase transformer to be modeled as a simple resistor-inductance branch, with $R_t = r_p + n^2 r_s$ and $L_t = L_p + n^2 L_s$. The simplified transformer is depicted in Figure 10 below.

Figure 10 – Simplified single-phase transformer model.

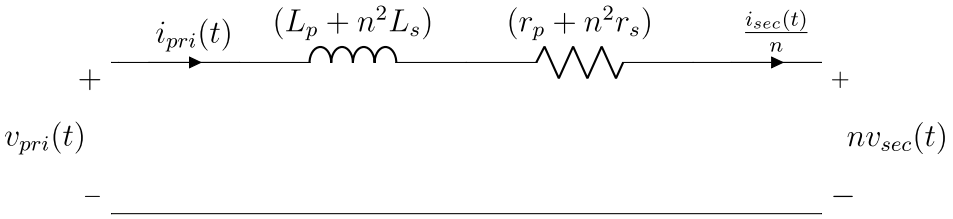


Source: Author (2022).

The circuits presented in Figures 8, 9 and 10 represent the behavior in individual phases only. The association of this circuits into three-phase schemes are well-suited for modeling multi-phase banks of single-phase transformers, where each phase is magnetically independent from the other (ENRIGHT, 1996). Furthermore, in studies involving transient studies, often consider transformers with magnetically independent units (ENRIGHT, 1996; BICKFORD; HEATON, 1986). Three-limb transformers have a different type of modelling that what was presented in this work up to now. This is because the different magnetic fields will result in self- and mutual-inductances. These transformers are well described in references (CHERRY, 1949; ENRIGHT, 1996; ENRIGHT *et al.*, 1997) and the representation of a multi-limb transformer is shown in Figure 11.

Figure 11 – Representation of a three-limb three-phase transformer.

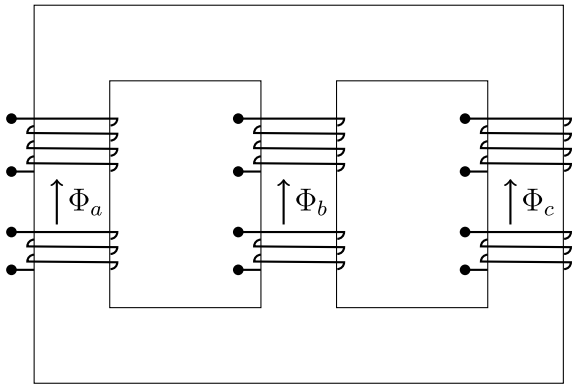


Source: Author (2022).

Therefore, if each phase is modeled by an independent magnetic circuit, a three-phase transformer can be represented by equation (3.49). Note that, since three magnetically independent units were used to represent the three-phase transformer, each phase

has an independent equation.

$$\frac{d}{dt}\begin{bmatrix} i_a(t) \\ i_b(t) \\ i_c(t) \end{bmatrix} = \begin{bmatrix} \frac{-R_t}{L_t} & 0 & 0 \\ 0 & \frac{-R_t}{L_t} & 0 \\ 0 & 0 & \frac{-R_t}{L_t} \end{bmatrix} \begin{bmatrix} i_a(t) \\ i_b(t) \\ i_c(t) \end{bmatrix} + \frac{1}{L_t}\begin{bmatrix} v_{pri,a}(t) - nv_{sec,a}(t) \\ v_{pri,b}(t) - nv_{sec,b}(t) \\ v_{pri,c}(t) - nv_{sec,c}(t) \end{bmatrix}. \tag{3.49}$$

### 3.3.2 Grid Equivalent

In order to perform an adequate study of a device that is connected to the power grid, it is necessary to represent the mains by an equivalent circuit. This is normally done by using a Thévenin equivalent (DOMMEL, 1986). The Thévenin equivalent circuit is basically a voltage source, $V_{TH}$, connected to an equivalent impedance, $Z_{th}$. In three-phase systems, the impedance can be represented by phase resistors connected to magnetically-coupled inductors. The representation of such equivalent system is displayed in Figure 12 below. Note that the block is made to represent the three-phase magnetically-coupled inductors.

Figure 12 – Thévenin equivalent in a three-phase system.

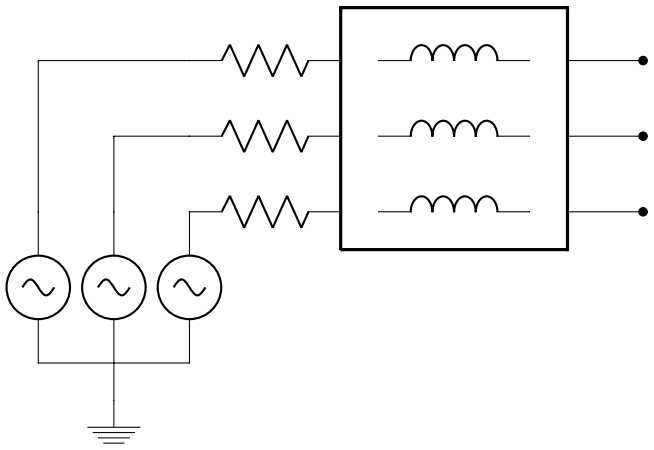

Source: Author (2022).

If the system is symmetrical, the Thévenin equivalent system would also result in a symmetrical equation, which is represented in equation (3.50).

$$\begin{bmatrix} L_s & L_m & L_m \\ L_m & L_s & L_m \\ L_m & L_m & L_s \end{bmatrix} \frac{d}{dt}\begin{bmatrix} i_a(t) \\ i_b(t) \\ i_c(t) \end{bmatrix} = \begin{bmatrix} -R_{th} & 0 & 0 \\ 0 & -R_{th} & 0 \\ 0 & 0 & -R_{th} \end{bmatrix} \begin{bmatrix} i_a(t) \\ i_b(t) \\ i_c(t) \end{bmatrix} + \begin{bmatrix} v_{a,1}(t) - v_{a,2}(t) \\ v_{b,1}(t) - v_{b,2}(t) \\ v_{c,1}(t) - v_{c,2}(t) \end{bmatrix}. \tag{3.50}$$

where $R_{th}$ is the Thévenin equivalent resistance, $L_s$ is the equivalent self inductance, and $L_m$ is the equivalent mutual inductance.

### 3.3.3 Balanced Equivalent System Representation

Equivalent systems can be obtained with an association of the transformer equation presented in (3.49) and the grid equivalent equation presented in (3.50). First, suppose

that

$$i_a + i_b + i_c = 0. \tag{3.51}$$

This equation is true for symmetrical balanced cases and for unbalanced cases with no zero-sequence component, i.e., three-phase three-wire systems. Therefore, equation presented in (3.50) can be written as:

$$\begin{cases} L_s \dfrac{d}{dt} i_a(t) + L_m \dfrac{d}{dt} \left[ i_b(t) + i_c(t) \right] & = -R_{th} i_a(t) + v_{a,1}(t) - v_{a,2}(t), \\ L_s \dfrac{d}{dt} i_b(t) + L_m \dfrac{d}{dt} \left[ i_a(t) + i_c(t) \right] & = -R_{th} i_b(t) + v_{b,1}(t) - v_{b,2}(t), \\ L_s \dfrac{d}{dt} i_c(t) + L_m \dfrac{d}{dt} \left[ i_a(t) + i_b(t) \right] & = -R_{th} i_c(t) + v_{c,1}(t) - v_{c,2}(t). \end{cases} \tag{3.52}$$

Which can be further simplified into

$$\begin{cases} (L_s - L_m) \dfrac{d}{dt} i_a(t) & = -R_{th} i_a(t) + v_{a,1}(t) - v_{a,2}(t), \\ (L_s - L_m) \dfrac{d}{dt} i_b(t) & = -R_{th} i_b(t) + v_{b,1}(t) - v_{b,2}(t), \\ (L_s - L_m) \dfrac{d}{dt} i_c(t) & = -R_{th} i_c(t) + v_{c,1}(t) - v_{c,2}(t). \end{cases} \tag{3.53}$$

Furthermore, if the transformer, described by (3.49), and the balanced symmetrical Thévenin equivalent, described by (3.53), are connected in series, it is possible to write that:

$$\begin{cases} (L_s - L_m + L_t) \dfrac{d}{dt} i_a(t) & = -\left(R_{th} + R_t\right) i_a(t) + v_{p,a}(t) - n v_{a,2}(t), \\ (L_s - L_m + L_t) \dfrac{d}{dt} i_b(t) & = -\left(R_{th} + R_t\right) i_b(t) + v_{p,b}(t) - n v_{b,2}(t), \\ (L_s - L_m + L_t) \dfrac{d}{dt} i_c(t) & = -\left(R_{th} + R_t\right) i_c(t) + v_{p,c}(t) - n v_{c,2}(t). \end{cases} \tag{3.54}$$

If $L_{eq} = L_s - L_m + L_t$, $R_{eq} = R_{th} + R_t$, then

$$\begin{cases} L_{eq} \dfrac{d}{dt} i_a(t) & = -R_{eq} i_a(t) + v_{p,a}(t) - n v_{a,2}(t), \\ L_{eq} \dfrac{d}{dt} i_b(t) & = -R_{eq} i_b(t) + v_{p,b}(t) - n v_{b,2}(t), \\ L_{eq} \dfrac{d}{dt} i_c(t) & = -R_{eq} i_c(t) + v_{p,c}(t) - n v_{c,2}(t). \end{cases} \tag{3.55}$$

Since the system is considered to be balanced, it is possible to use the Space Phasor theory presented in Section 3.2 to simplify equation (3.55) even further. In fact, by using

$T_{sph}$ transformation and selecting $n\overrightarrow{v}_2 = \overrightarrow{v}_g$, it is possible to write the following space phasor representation for equation (3.55):

$$L_{eq}\frac{d}{dt}\overrightarrow{i}(t) = -R_{eq}\overrightarrow{i}(t) + \overrightarrow{v}_p(t) - \overrightarrow{v}_g(t). \tag{3.56}$$

At this point, it is important to highlight a partial conclusions that can be drawn from this section. The connection of a three-phase transformer, built with individual and independent magnetic structures per phase, connected to a magnetically coupled three-phase Thévenin equivalent could be simplified into a simple resistor-inductor branch. Moreover, the three-phase equation could be re-written as a single equation by using the space phasor methodology. This fact actually makes the analysis on three-phase converter, on Section 3.4, more simple and concise.

## 3.4 VOLTAGE-SOURCED CONVERTER

In order to describe a correct and adequate model of the VSC and of the BTB converter, its fundamental components need to be well described. Therefore, this section will start by describing switching device model, then it will introduce the switching and the average model of the half-bridge converter. Later, the half-bridge converter model will be extended to the voltage-sourced converter (VSC). The state-space approach will be preferred due to the advantages that we can extract from that representation. Furthermore, in this section, the reader will see analysis that are based in the discussion conducted in all previous sections of this chapter.

### 3.4.1 **Switching Device Model**

One of the most common example of switches used in VSCs is the Insulated-Gate Bipolar Transistor, or IGBT (BALIGA, 1979). Another example is the Integrated Gate Commutated Thyristor, or IGCT. These switches should be fully-controllable, meaning that both *turn-on* and *turn-off* moments are controlled by a signal in its gate. Besides, the switch should be a reverse-conducting device, usually achieved by connecting a transistor and a diode in anti-parallel (MILANO; MANJAVACAS, 2019). In this study, IGBT switches are going to be used. They are well suited for voltage levels up to 6.5 kV and moderate switching frequency ($<$ 50 kHz) (KASSAKIAN; SCHLECHT; VERGHESE, 1991).

Figure 13 depicts a representation of a non-ideal switch. The diode $D$ is an ideal diode, meaning that it starts conducting when the anode-cathode voltage is greater than zero. The DC-source connected to the diode's anode, $v_{di}$, represents the forward threshold voltage. It means that when a voltage greater than $v_{di}$ is applied to the diode it will be turned-on and a current $i_{di}$ will flow through it. The value of $v_{di}$ may vary due to the composition of the diode but it is typically very small, specially if compared to the

Figure 13 – Diagram of a non-ideal IGBT.

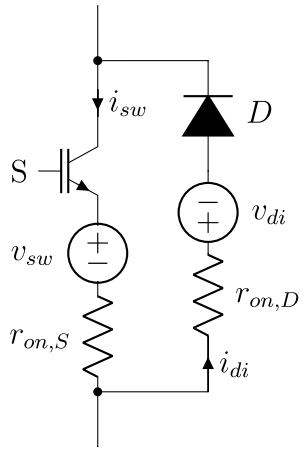


Source: Author (2022).

voltage applied over the entire switch (MOHAN; UNDELAND; ROBBINS, 2003). The transistor denoted by $S$ is also an ideal component, meaning that when the appropriate voltage signal is applied in its gate, the transistor starts conducting current $i_{sw}$. The DC-source connected in series with $S$ represents the occurring on-state voltage drop. For both components, the resistance $r_{on}$ represents the voltage drop proportional to the current that appear when those components are turned-on.

In this work, the on-state voltage drop $v_{sw}$ of the transistor $S$ and the forward threshold voltage $v_{di}$ of the diode $D$ are negligible if compared to the voltage level of the converters (YAZDANI; IRAVANI, 2010). Therefore these values are going to be ignored and set to be $v_{sw} = v_{di} = 0$. For a more detailed representation, these values can be added to the model. The resistances $r_{on,S}$ and $r_{on,D}$ are going to be considered as having the same value, $r_{on}$. Next section will describe how this resistance can be included in the model.

### 3.4.2 **Half-bridge Converter Switching Model**

The half-bridge converter is a DC/AC converter and its operation is essential for the study of three-phase VSCs. This converter is composed of two switching devices as the non-ideal IGBT described in last section. Upper IGBT is composed of transistor $S_1$ and diode $D_1$, while lower IGBT is composed of $S_4$ and $D_4$. In addition, two DC voltage sources are connected to the DC terminal of this converter. The AC terminal is connected to a AC voltage source through an RL branch. Figure 14 depicts the half-bridge converter and all of its devices and connections.

Now, let us derive the mathematical equations that fully characterize the dynamic behavior of the half-bridge converter. This analysis is made based on (YAZDANI; IRAVANI,

Figure 14 – Half-bridge converter with non-ideal IGBTs.

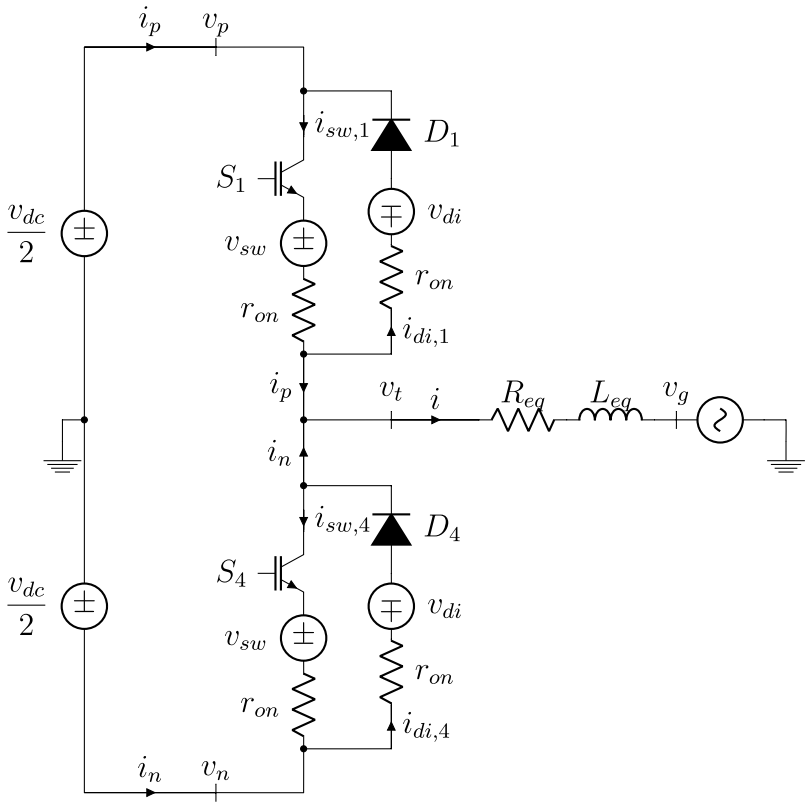


Source: Author (2022).

2010). First, note that the upper current and lower current can be described as

$$i_p(t) = i_{sw,1}(t) - i_{di,1}(t), \tag{3.57}$$

$$i_n(t) = -i_{sw,4}(t) + i_{di,4}(t). \tag{3.58}$$

In addition, note that

$$i(t) = i_p(t) + i_n(t). \tag{3.59}$$

Now, let us make an analysis supposing that $i > 0$. In this case, consider that $S_1$ is on, while $S_4$ is off. Both diodes $D_1$ and $D_4$ are reverse biased and, therefore, they do not conduct. In addition, $S_4$ is off and, hence, $i_{sw,4} = 0$. This will result in $i_p(t) = i_{sw,1}(t)$ and $i_n(t) = 0$. With respect to $v_t(t)$ we can write the following equation:

$$v_t(t) = v_p(t) - v_{sw} - r_{on} i_{sw,1}(t) = \frac{v_{dc}}{2} - v_{sw} - r_{on} i_{sw,1}(t). \tag{3.60}$$

Note that $i(t) = i_p(t) = i_{sw,1}(t)$. Therefore, the dynamic equation for the VSC connected to the grid is

$$\begin{aligned} v_t(t) &= R_{eq} i(t) + L_{eq} \frac{di(t)}{dt} + v_g(t), \\ \frac{v_{dc}}{2} - v_{sw} - r_{on} i_{sw,1}(t) &= R_{eq} i_{sw,1}(t) + L_{eq} \frac{di_{sw,1}(t)}{dt} + v_g(t), \\ \frac{v_{dc}}{2} - v_{sw} - v_g(t) &= (R_{eq} + r_{on})\, i_{sw,1}(t) + L_{eq} \frac{di_{sw,1}(t)}{dt}. \end{aligned} \tag{3.61}$$

When $S_1$ turns off and $S_4$ turns on, there is a moment where $S_1$ and $D_4$ conduct at the same moment for a brief time interval. This small time interval where both devices are conducting is essential to the development of a non-ideal model for the half-bridge converter. This effect will result in power losses that will be ignored in this study. After that, $i_{sw,1}(t) = i_p(t)$ will become zero and $i_n(t) = i_{di,4}$. Therefore, the equation for $v_t(t)$ becomes:

$$v_t(t) = v_n(t) - v_{di} - r_{on} i_{di,4}(t) = -\frac{v_{dc}}{2} - v_{di} - r_{on} i_{di,4}(t). \tag{3.62}$$

Now, $i(t) = i_n(t) = i_{di,4}(t)$. Hence, the differential equation can be written as

$$-\frac{v_{dc}}{2} - v_{di} - v_g(t) = (R_{eq} + r_{on})\, i_{di,4}(t) + L_{eq}\frac{di_{di,4}(t)}{dt}. \tag{3.63}$$

It is possible to perform a similar analysis for $i(t) < 0$ yielding

$$v_t(t) = v_p(t) + v_{sw} + r_{on} i_{di,1}(t) = \frac{v_{dc}}{2} + v_{sw} + r_{on} i_{di,1}(t), \tag{3.64}$$

and

$$\frac{v_{dc}}{2} + v_{di} - v_g(t) = -(R_{eq} + r_{on})\, i_{di,1}(t) - L_{eq}\frac{di_{di,1}(t)}{dt}, \tag{3.65}$$

for $S_1$ on and $S_4$ off, and

$$v_t(t) = v_n(t) + v_{sw} + r_{on} i_{sw,4}(t) = -\frac{v_{dc}}{2} + v_{sw} + r_{on} i_{sw,4}(t), \tag{3.66}$$

and

$$-\frac{v_{dc}}{2} + v_{sw} - v_g(t) = -(R_{eq} + r_{on})\, i_{sw,4}(t) - L_{eq}\frac{di_{sw,4}(t)}{dt}, \tag{3.67}$$

for $S_4$ on and $S_1$ off. As it was discussed in previous section $v_{sw}$ and $v_{di}$ are small, specially if compared to $v_{dc}/2$ and, hence, let us assume $v_{sw} = v_{di} = 0$. Under this reasonable assumption, let us analyze the equations for $v(t)$ when $S_1$ is on and $S_4$ is off

$$\begin{cases} v(t) = \dfrac{v_{dc}}{2} - r_{on} i_{sw,1}(t) = \dfrac{v_{dc}}{2} - r_{on} i_p(t), \\ v(t) = \dfrac{v_{dc}}{2} + r_{on} i_{di,1}(t) = \dfrac{v_{dc}}{2} - r_{on} i_p(t). \end{cases} \tag{3.68}$$

Therefore, both equations described the same identity for $v(t)$ and the differential equation describing the dynamic behavior of the half-bridge converter is

$$\begin{aligned} \frac{v_{dc}}{2} - v_g(t) &= (R_{eq} + r_{on})\, i_{sw,1}(t) + L_{eq}\frac{di_{sw,1}(t)}{dt}, \\ &= -(R_{eq} + r_{on})\, i_{di,1}(t) - L_{eq}\frac{di_{di,1}(t)}{dt}, \\ &= (R_{eq} + r_{on})\, i_p(t) + L_{eq}\frac{di_p(t)}{dt}. \end{aligned} \tag{3.69}$$

Similarly, we can perform a similar analysis for $v(t)$ when $S_4$ is on and $S_1$ is off, resulting in

$$\begin{cases} v(t) = -\dfrac{v_{dc}}{2} - r_{on} i_{di,4}(t) = -\dfrac{v_{dc}}{2} - r_{on} i_n(t), \\ v(t) = -\dfrac{v_{dc}}{2} + r_{on} i_{sw,4}(t) = -\dfrac{v_{dc}}{2} - r_{on} i_n(t). \end{cases} \tag{3.70}$$

Which will lead to the following dynamic equation

$$\begin{aligned} -\frac{v_{dc}}{2} - v_g(t) &= (R_{eq} + r_{on})\, i_{di,4}(t) + L_{eq} \frac{di_{di,4}(t)}{dt}, \\ &= -(R_{eq} + r_{on})\, i_{sw,4}(t) - L_{eq} \frac{di_{sw,4}(t)}{dt}, \\ &= (R_{eq} + r_{on})\, i_n(t) + L_{eq} \frac{di_n(t)}{dt}. \end{aligned} \tag{3.71}$$

Now, consider the following switching functions

$$s_1(t) = \begin{cases} 1, & \text{when } S_1 \text{ is } \textbf{on}, \\ 0, & \text{when } S_1 \text{ is } \textbf{off}. \end{cases} \tag{3.72}$$

and

$$s_4(t) = \begin{cases} 1, & \text{when } S_4 \text{ is } \textbf{on}, \\ 0, & \text{when } S_4 \text{ is } \textbf{off}. \end{cases} \tag{3.73}$$

Note that $s_1(t) + s_4(t) = 1$ and that $s_1(t)s_4(t) = 0$ for all $t$. In addition, note that $i_p(t) = i(t)s_1(t)$ and that $i_n(t) = i(t)s_4(t)$. Hence,

$$\begin{aligned} v(t) &= \left[\frac{v_{dc}}{2} - r_{on} i_p(t)\right] s_1(t) + \left[-\frac{v_{dc}}{2} - r_{on} i_n(t)\right] s_4(t), \\ v(t) &= \frac{v_{dc}}{2} \left[s_1(t) - s_4(t)\right] - r_{on} \left[i_p(t) s_1(t) + i_n(t) s_4(t)\right], \\ v(t) &= \frac{v_{dc}}{2} \left[s_1(t) - s_4(t)\right] - r_{on} \left[i(t) s_1^2(t) + i(t) s_4^2(t)\right], \\ v(t) &= \frac{v_{dc}}{2} \left[s_1(t) - s_4(t)\right] - r_{on} i(t) \left[s_1(t) + s_4(t)\right]^2, \\ v(t) &= \frac{v_{dc}}{2} \left[s_1(t) - s_4(t)\right] - r_{on} i(t). \end{aligned} \tag{3.74}$$

Which will lead us to the following differential equation

$$\frac{v_{dc}}{2} \left[s_1(t) - s_4(t)\right] - v_g(t) = (R_{eq} + r_{on})\, i(t) + L_{eq} \frac{di(t)}{dt}. \tag{3.75}$$

Finally, the model can be completely characterized by the following set of equations

$$\begin{cases} \dfrac{di(t)}{dt} &= -\dfrac{(R_{eq} + r_{on})}{L_{eq}} i(t) + \dfrac{v_{dc}}{2L_{eq}} \left[s_1(t) - s_4(t)\right] - \dfrac{v_g(t)}{L_{eq}}, \\ v(t) &= \dfrac{v_{dc}}{2} \left[s_1(t) - s_4(t)\right] - r_{on} i(t), \\ i_p(t) &= s_1(t) i(t), \\ i_n(t) &= s_4(t) i(t). \end{cases} \tag{3.76}$$

The power can be divided into three stages: the DC power coming from the DC source, or $P_{DC}(t)$, the AC power observed in the terminals of the VSC, or $P_t(t)$, and the AC power in the terminals of the AC source, or $P_s(t)$. For $P_{DC}(t)$ we can write that

$$\begin{aligned} P_{DC}(t) &= v_p(t)i_p(t) + v_n(t)i_n(t) = \frac{v_{dc}}{2}i(t)s_1(t) - \frac{v_{dc}}{2}i(t)s_4(t), \\ P_{DC}(t) &= \frac{v_{dc}}{2}i(t)\left[s_1(t) - s_4(t)\right]. \end{aligned} \tag{3.77}$$

For $P_t(t)$, it is possible to derive that

$$\begin{aligned} P_t(t) &= v_t(t)i(t) = \frac{v_{dc}}{2}\left[s_1(t) - s_4(t)\right]i(t) - r_{on}i^2(t), \\ P_t(t) &= P_{DC}(t) - r_{on}i^2(t). \end{aligned} \tag{3.78}$$

Note that the power loss $P_{loss}(t) = P_{DC}(t) - P_t(t)$ is equal to $r_{on}i^2(t)$. Therefore, using this representation, it is possible to account for losses in the converter and the representation of the half-bridge is not fully ideal. For the value of $P_g(t)$ it is possible to write that

$$P_g(t) = v_g(t)i(t). \tag{3.79}$$

All these equations will correctly represent a switching half-bridge converter, but the model can still be enhanced to represent other types of phenomenon (YAZDANI; IRAVANI, 2010) ignored in this study. In fact, the set of equations in (3.76) is considered to be suitable for the analysis performed in this work. In addition, it is very important to note, at this point, that there's no explicit relationship between the modulation index $m(t)$, which is the only control variable in a half-bridge converter, and the state variables (YAZDANI; IRAVANI, 2010). Therefore, it is necessary to work on (3.76) in order to express the dynamic behavior of the system as a function of its state and control variables. This is the main motivation behind the average model for the half-bridge converter, discussed in next subsection.

### 3.4.3 **Half-bridge Converter Averaged Model**

The averaging of fast-switching devices is a well known strategy to represent a circuit's dynamic behavior in a very convenient manner for control design (KASSAKIAN; SCHLECHT; VERGHESE, 1991). The average representation of a circuit is well-suited for the study conducted here, since closed-loop control systems often present great attenuation for high frequencies (YAZDANI; IRAVANI, 2010). Therefore, dynamics in low frequencies are more relevant for the process of designing an adequate controller.

In the literature, it is possible to find the averaging process of power electronic converters in different ways. References such as (KASSAKIAN; SCHLECHT; VERGHESE, 1991; YAZDANI; IRAVANI, 2010; MOHAN; UNDELAND; ROBBINS, 2003; BACHA *et al.*,

2014; SUNTIO; MESSO; PUUKKO, 2017; SHARIFABADI *et al.*, 2016; TEODORESCU; LISERRE; RODRIGUEZ, 2011) develop the process in a less mathematically rigid manner. In these references, the averaging of a variable is presented and the technique is applied to the differential equation without showing any restrictions to the method. In this work, however, the averaging process is carried out in a more rigid manner, as it is shown in (KREIN *et al.*, 1990; SUN; GROTSTOLLEN, 1992). This is done by taking into account the theory presented in Section 2.4 and some results obtained in Subsection 3.1.2.

Hence, let us first consider the differential equation that was presented in (3.76):

$$\frac{di(t)}{dt} = -\frac{(R_{eq} + r_{on})}{L_{eq}} i(t) + \frac{v_{dc}}{2L_{eq}} \left[s_1(t) - s_4(t)\right] - \frac{v_g(t)}{L_{eq}}. \tag{3.80}$$

Note that this equation does not have the form required for the application of the averaging process as it was shown in Section 2.4, i.e. $\dot{x} = \varepsilon f(x,u,\varepsilon)$. To apply the averaging, a small parameter $\varepsilon$ needs to be introduced in (3.80) (KREIN *et al.*, 1990). In this work, this small parameter is set to be the switching period, i.e. $\varepsilon = T_s$ and, to do so, it is necessary to scale the time frame as shown in (3.81). Recall that $T_s = \frac{1}{f_s}$.

$$\tau T_s = t. \tag{3.81}$$

By using the scale in (3.81), differential equation (3.80) can be re-written as (KREIN *et al.*, 1990):

$$\frac{di(\tau)}{d\tau} = \frac{dt}{d\tau}\frac{di(t)}{dt} = T_s \left\{ -\frac{(R_{eq} + r_{on})}{L_{eq}} i(\tau) + \frac{v_{dc}}{2L_{eq}} \left[s_1(\tau) - s_4(\tau)\right] - \frac{v_g(\tau)}{L_{eq}} \right\}. \tag{3.82}$$

Note that $T_s$ is, in fact, a very small parameter when the switching frequency $f_s$ is very large. Therefore, it is possible to apply the averaging in equation (3.82), as described in equations (2.68) and (2.69), yielding the following KBM equations.

$$i(\tau) = \bar{i}(\tau) + T_s\Psi_1(\tau,\bar{i}(\tau)) + T_s^2\Psi_2(\tau,\bar{i}(\tau)) + T_s^3\Psi_3(\tau,\bar{i}(\tau)) + \cdots, \tag{3.83}$$

$$\frac{d\bar{i}(\tau)}{d\tau} = T_sG_1(\bar{i}(\tau)) + T_s^2G_2(\bar{i}(\tau)) + T_s^3G_3(\bar{i}(\tau)) + \cdots. \tag{3.84}$$

In order to make annotations easier to follow, let us omit the arguments of functions $\Psi$ and $G$. If equation (3.83) is differentiated with respect to $\tau$, it is possible to write

$$\frac{di(\tau)}{d\tau} = \frac{d\bar{i}(\tau)}{d\tau} + T_s\frac{d\Psi_1}{d\tau} + T_s^2\frac{d\Psi_2}{d\tau} + T_s^3\frac{d\Psi_3}{d\tau} + \cdots. \tag{3.85}$$

The left side of equation (3.85) can be replaced by the following equation.

$$\begin{aligned}\frac{di(\tau)}{d\tau} &= T_s \left\{ -\frac{(R + r_{on})}{L} i(\tau) + \frac{v_{dc}}{2L} \left[s_1(\tau) - s_4(\tau)\right] - \frac{v_g(\tau)}{L} \right\}, \\ &= T_s \left\{ -\frac{(R + r_{on})}{L} \left[\bar{i}(\tau) + T_s\Psi_1 + T_s^2\Psi_2 + \cdots\right] + \frac{v_{dc}}{2L} \left[s_1(\tau) - s_4(\tau)\right] - \frac{v_g(\tau)}{L} \right\}\end{aligned} \tag{3.86}$$

In order to simplify the right-hand side of Equation (3.85) it is important to recall that

$$\frac{d\Psi_x}{d\tau} = \frac{d\Psi_x}{d\tau} + \frac{d\Psi_x}{d\bar{i}}\frac{d\bar{i}}{d\tau} = \frac{d\Psi_x}{d\tau} + \frac{d\Psi_x}{d\bar{i}}\left(T_sG_1 + T_s^2G_2 + \cdots\right). \tag{3.87}$$

where $x = 1,2,3,\cdots$. Hence, the right-hand side of Equation (3.85) can be re-written as:

$$\begin{aligned}\frac{d\bar{i}(\tau)}{d\tau} + T_s\frac{d\Psi_1}{d\tau} + T_s^2\frac{d\Psi_2}{d\tau} + \cdots = &\left[T_sG_1 + T_s^2G_2 + \cdots\right] + \\ &+ T_s\left[\frac{d\Psi_1}{d\tau} + \frac{d\Psi_1}{d\bar{i}}\left(T_sG_1 + T_s^2G_2 + \cdots\right)\right] + \\ &+ T_s^2\left[\frac{d\Psi_2}{d\tau} + \frac{d\Psi_2}{d\bar{i}}\left(T_sG_1 + T_s^2G_2 + \cdots\right)\right] + \cdots\end{aligned} \tag{3.88}$$

Replacing (3.86) and (3.88) in (3.85) yields

$$\begin{aligned}&T_s\left\{-\frac{(R+r_{on})}{L}\left[\bar{i}(\tau) + T_s\Psi_1 + T_s^2\Psi_2 + \cdots\right] + \frac{v_{dc}}{2L}\left[s_1(\tau) - s_4(\tau)\right] - \frac{v_g(\tau)}{L}\right\} = \\ &= \left[T_sG_1 + T_s^2G_2 + \cdots\right] + T_s\left[\frac{d\Psi_1}{d\tau} + \frac{d\Psi_1}{d\bar{i}}\left(T_sG_1 + T_s^2G_2 + \cdots\right)\right] + \\ &+T_s^2\left[\frac{d\Psi_2}{d\tau} + \frac{d\Psi_2}{d\bar{i}}\left(T_sG_1 + T_s^2G_2 + \cdots\right)\right] + \cdots\end{aligned} \tag{3.89}$$

To find functions $G$ or $\Psi$ one needs to separate Equation (3.89) using polynomial identity. A large order KBM equation, i.e. solving (3.89) for a large number of terms, would give as a result an incredible refined approximation. However, for this work, we only need to find $G_1$, which should be equal to the first order average of the dynamic system described by Equation (3.80). Function $\Psi_1$ is also calculated here, but for a different reason. Hence, for term $T_s$ it is possible to write the following equation:

$$-\frac{(R_{eq}+r_{on})}{L_{eq}}\bar{i}(\tau) + \frac{v_{dc}}{2L_{eq}}\left[s_1(\tau) - s_4(\tau)\right] - \frac{v_g(\tau)}{L_{eq}} = G_1(\bar{i}) + \frac{d\Psi_1}{d\tau}. \tag{3.90}$$

Here, let us solve for $G_1$ by taking the average of (3.90) over one period with respect to $\tau$ (KREIN *et al.*, 1990).

$$\frac{1}{T_s}\int_{t-T_s}^{t} = \frac{1}{T_s}\int_{t-T_s}^{t}\left[G_1(\bar{i})\frac{d\Psi_1}{d\tau}\right]d\tau. \tag{3.91}$$

Recall that $\Psi_1$ is $T_s-$periodic and that the average of $s_1(\tau) - s_4(\tau)$ is given in Equation (3.6). Hence

$$G_1(\bar{i}) = -\frac{(R_{eq}+r_{on})}{L_{eq}}\bar{i}(\tau) + \frac{v_{dc}}{2L_{eq}}(2d-1) - \frac{v_g(\tau)}{L_{eq}}. \tag{3.92}$$

Note that replacing (3.92) in (3.90) yields

$$\frac{d\Psi_1}{d\tau} = \frac{v_{dc}}{2L_{eq}}\left[s_1(\tau) - s_4(\tau) - 2d + 1\right]. \tag{3.93}$$

Therefore

$$\Psi_1(\tau) = \frac{v_{dc}}{2L_{eq}} \int \left[ s_1(\tau) - s_4(\tau) - 2d + 1 \right] d\tau = \frac{v_{dc}}{2L_{eq}} w(\tau) - \frac{v_{dc}}{2L_{eq}} (2d-1)\tau, \tag{3.94}$$

where

$$w(\tau) = \begin{cases} \tau, \text{ when } s_1(\tau) = 1, \\ -\tau, \text{ otherwise.} \end{cases} \tag{3.95}$$

Finally, by replacing (3.92) and (3.94) in equations (3.84) and (3.83), it is possible to obtain the following approximate KBM equations

$$i(\tau) \approx \bar{i}(\tau) + T_s \Psi_1(\tau) = \bar{i}(\tau) + T_s \left[ \frac{v_{dc}}{2L_{eq}} w(\tau) - \frac{v_{dc}}{2L_{eq}} (2d-1)\tau \right], \tag{3.96}$$

$$\frac{d\bar{i}(\tau)}{d\tau} \approx T_s G_1(\bar{i}) = T_s \left[ -\frac{(R_{eq} + r_{on})}{L_{eq}} \bar{i}(\tau) + \frac{v_{dc}}{2L_{eq}} (2d-1) - \frac{v_g(\tau)}{L_{eq}} \right]. \tag{3.97}$$

Note that, on (3.96), the first term describes the average value of the current, while the second term describes a first order approximation of the current ripple over one switching period $T_s$. In addition, if Equation (3.97) is re-scaled to time frame again, it gives as result the following equation

$$\frac{d\bar{i}(t)}{dt} = -\frac{(R_{eq} + r_{on})}{L_{eq}} \bar{i}(t) + \frac{v_{dc}}{2L_{eq}} m(t) - \frac{v_g(t)}{L_{eq}} \tag{3.98}$$

where $m(t) = 2d - 1$ as it was shown in (3.9).

As one can see, Equation (3.98) is exactly the same equation obtained when applying the less rigorous averaging process found in (YAZDANI; IRAVANI, 2010). However, in the present work, it is possible to use perturbation theory to extract important conclusion from the averaged system. In fact, since the KBM approach was used, an error bound between the actual and the average system can be calculated using Equation (2.62). In addition, note that Equation (3.97) is true within the frame of one time-period, but its re-scaled counterpart, (3.98), is valid for every $t^+ \in \mathbb{R}$. Hence, using perturbation theory, it is possible to guarantee that the error will remain bounded and stability of the approximated solution will imply in the stability of the exact solution.

The KBM approach is also interesting because it allows the original signal $i(t)$ to be reconstructed from $\bar{i}(t)$ by adding functions $\Psi$, as described in (3.83). In order to show how this could be done, $\Psi_1(\tau)$ was calculated as it is described in (3.96). In fact, a comparison between average, approximate and exact solutions is depicted in Figure 15.

Note that the in the upper part of the figure, a comparison between solutions $i(t)$ and $\bar{i}(t)$ is presented. In the lower part, a comparison between the exact solution and the approximate value presented in equation (3.96) is displayed. Note that the average value is, indeed, smoother than $i(t)$ and that the approximation using (3.96) is very close

Figure 15 – Comparison of average, approximate and exact solutions for current behavior.

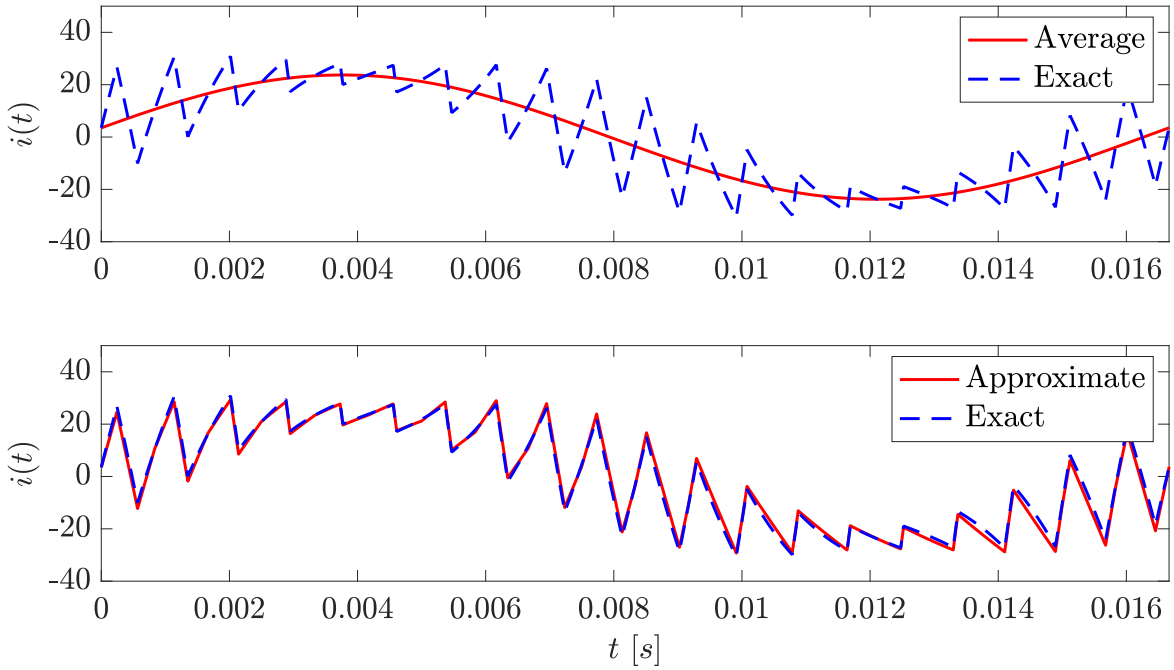


Source: Author (2022).

to the exact solution. In order to reproduce these results, the reader should consider a system where $R_{eq} + r_{on} = 75.4m\Omega$, $L_{eq} = 2mH$, $v_s(t) = 180\sin(2\pi 60t)\,V$, $v_{dc} = 200V$, $m(t) = 0.9\sin(2\pi 60t + 0.1)\,V$, and switching frequency equal to $f_s = 1200\ Hz$. The reader should also consider initial state as $i(0) = 3.499A$ and an appropriate small time step to integrate both equations.

### 3.4.4 Averaged Three-Phase Two-Level VSC

The three-phase, two-level, VSC is presented in Figure 16 and it is basically composed of three half-bridge converters associated to the same capacitor (YAZDANI; IRAVANI, 2010). Transformer and grid equivalent resistors, which are presented in Sub-section 3.3, can be added together with $r_{on}$, lumping them into $R$. On a similar way, it is possible to obtain inductance $L$ by lumping all magnetic effects from transformer and the three-phase grid Thévenin equivalent presented in Sub-section 3.3. As it was shown previously, all these effects can be represented by an $RL$ branch like the one depicted in Figure 16.

Moreover, it is possible to use the results from subsections 3.3 and 3.4.3 to describe the three-phase, two-level, VSC in an average space-phasor equation as

$$L\frac{d}{dt}\overrightarrow{i}(t) = -R\overrightarrow{i}(t) + \frac{\bar{v}_{dc}(t)}{2}\overrightarrow{m}(t) - \overrightarrow{v}_g(t). \tag{3.99}$$

where the average value of the DC bus voltage $\bar{v}_{dc}$ can also be adopted by using the KGM approach. Equation (3.99) can be transformed into $\alpha\beta$-reference frame by using the

Figure 16 – Diagram representing a three-phase voltage-sourced converter.

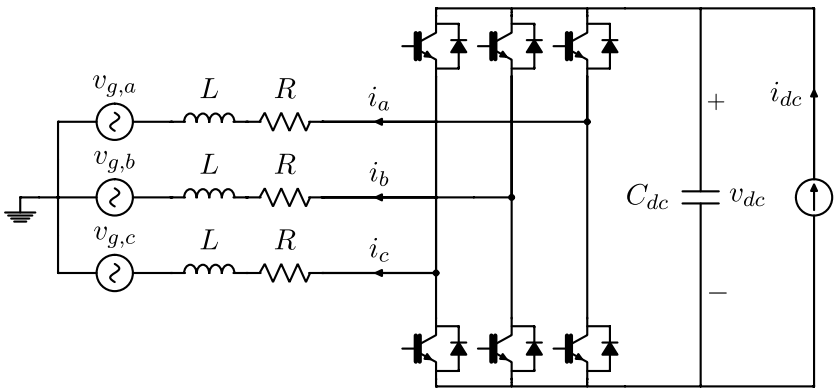


Source: Author (2022).

relation stated in (3.31), as follows.

$$L\frac{d}{dt}\left[\bar{i}_\alpha(t)+j\bar{i}_\beta(t)\right] = -R\left[\bar{i}_\alpha(t)+j\bar{i}_\beta(t)\right]+\frac{\bar{v}_{dc}(t)}{2}\left[m_\alpha(t)+jm_\beta(t)\right]- \\ -\left[\bar{v}_{g,\alpha}(t)+j\bar{v}_{g,\beta}(t)\right]. \tag{3.100}$$

By separating real and imaginary components from equation (3.100) it is possible to assemble the dynamic equation system that represents the three-phase VSC in $\alpha\beta$-frame:

$$\begin{cases} \dfrac{d}{dt}\bar{i}_\alpha(t) = -\dfrac{R}{L}\bar{i}_\alpha(t)+\dfrac{\bar{v}_{dc}(t)}{2L}m_\alpha(t)-\dfrac{1}{L}\bar{v}_{g,\alpha}(t), \\ \dfrac{d}{dt}\bar{i}_\beta(t) = -\dfrac{R}{L}\bar{i}_\beta(t)+\dfrac{\bar{v}_{dc}(t)}{2L}m_\beta(t)-\dfrac{1}{L}\bar{v}_{g,\beta}(t). \end{cases} \tag{3.101}$$

Alternatively, it is also possible to transform equation (3.99) into $dq$-reference frame by using relation stated in Equation (3.39). First let us consider the left-hand side of equation (3.99).

$$L\frac{d}{dt}\left\{\left[\bar{i}_d(t)+j\bar{i}_q(t)\right]e^{j\varepsilon(t)}\right\} = L\frac{d}{dt}\left[\bar{i}_d(t)+j\bar{i}_q(t)\right]-\frac{d}{dt}\varepsilon(t)L\bar{i}_q(t)+j\frac{d}{dt}\varepsilon(t)L\bar{i}_d(t). \tag{3.102}$$

However, if the angle $\varepsilon(t)$ comes from a Phase-Locked Loop, its derivative is the angular speed of the grid, $\omega(t)$. Hence

$$L\frac{d}{dt}\left\{\left[\bar{i}_d(t)+j\bar{i}_q(t)\right]e^{j\varepsilon(t)}\right\} = \left\{L\frac{d}{dt}\left[\bar{i}_d(t)+j\bar{i}_q(t)\right]-\omega(t)L\bar{i}_q(t)+j\omega(t)L\bar{i}_d(t)\right\}e^{j\varepsilon(t)}. \tag{3.103}$$

Furthermore, the right-hand side of equation (3.99), in $dq$-frame, becomes

$$L\left\{\frac{d}{dt}\left[\bar{i}_d(t)+j\bar{i}_q(t)\right]-\omega(t)L\bar{i}_q(t)+j\omega(t)L\bar{i}_d(t)\right\}e^{j\varepsilon(t)}=-R\left[\bar{i}_d(t)+j\bar{i}_q(t)\right]e^{j\varepsilon(t)}+ \\ +\frac{\bar{v}_{dc}(t)}{2}\left[m_d(t)+jm_q(t)\right]e^{j\varepsilon(t)}-\left[\bar{v}_{g,d}(t)+j\bar{v}_{g,q}(t)\right]e^{j\varepsilon(t)}. \tag{3.104}$$

Finally, by separating real and imaginary components from equation (3.104) it is possible to assemble the dynamic equation system that represents the three-phase VSC in $dq$-frame:

$$\begin{cases}\dfrac{d}{dt}\bar{i}_d(t)=-\dfrac{R}{L}\bar{i}_d(t)+\omega(t)\bar{i}_q(t)+\dfrac{\bar{v}_{dc}(t)}{2L}m_d(t)-\dfrac{1}{L}\bar{v}_{g,d}(t),\\ \dfrac{d}{dt}\bar{i}_q(t)=-\omega(t)\bar{i}_d(t)-\dfrac{R}{L}\bar{i}_q(t)+\dfrac{\bar{v}_{dc}(t)}{2L}m_q(t)-\dfrac{1}{L}\bar{v}_{g,q}(t).\end{cases} \tag{3.105}$$

Now, it is important to derive the equation which describes the transient behavior for the DC capacitor. In order to do so, it is necessary to perform a simple analysis on the power flowing through the converter. The power coming from the DC current source, $P_{in}$, is divided into two. The first term goes to the capacitor and it is named $P_{cap}$. The second term goes to the converter and, if the VSC device is modeled as ideal, the power goes to the AC system as $P_{out}$. Figure 17 depicts this phenomena.

Figure 17 – Representation of the power flowing through the converter.

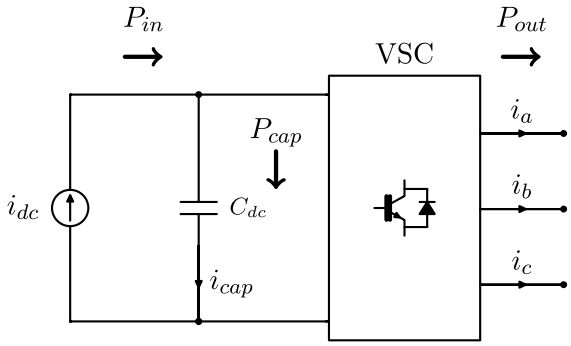


Source: Author (2022).

The power balance equation can be easily obtained and it is given by

$$P_{in}=P_{cap}+P_{out}. \tag{3.106}$$

However, the power coming from the DC source can be written as

$$P_{in}=i_{dc}(t)\bar{v}_{dc}(t), \tag{3.107}$$

where $\bar{v}_{dc}$ is the averaged voltage over the DC capacitor denoted in Figures 16 and 17. The power flowing through the capacitor, $P_{cap}$, can be described as

$$P_{cap} = i_{cap}(t)v_{dc}(t) = \left[C_{dc}\frac{d}{dt}\bar{v}_{dc}(t)\right]\bar{v}_{dc}(t). \tag{3.108}$$

In addition, the power flowing out of the VSC to the AC side can be derived from Equations (3.38) and (3.48), and recalling that the voltage synthesized by the VSC can be written as a function of the modulating signal $m(t)$ and the DC voltage $v_{dc}(t)$. In $\alpha\beta$-frame, it is possible to write

$$P_{out} = \frac{3\bar{v}_{dc}(t)}{4}\left[m_\alpha(t)\bar{i}_\alpha(t) + m_\beta(t)\bar{i}_\beta(t)\right], \tag{3.109}$$

while in $dq$-frame, the output power can be expressed as

$$P_{out} = \frac{3\bar{v}_{dc}(t)}{4}\left[m_d(t)\bar{i}_d(t) + m_q(t)\bar{i}_q(t)\right]. \tag{3.110}$$

Therefore, if Equations (3.107),(3.108) and (3.109) are replaced in Equation (3.106), it is possible to write the following equation.

$$i_{dc}(t)\bar{v}_{dc}(t) = \left[C_{dc}\frac{d}{dt}\bar{v}_{dc}(t)\right]\bar{v}_{dc}(t) + \frac{3\bar{v}_{dc}(t)}{4}\left[m_\alpha(t)\bar{i}_\alpha(t) + m_\beta(t)\bar{i}_\beta(t)\right]. \tag{3.111}$$

By dividing the entire equation by $v_{dc}(t)$ and recollecting the terms, it is possible to write the differential equation that describes the DC capacitor behavior in $\alpha\beta$-frame as shown below.

$$\frac{d}{dt}\bar{v}_{dc}(t) = -\frac{3}{4C_{dc}}m_\alpha(t)\bar{i}_\alpha(t) - \frac{3}{4C_{dc}}m_\beta(t)\bar{i}_\beta(t) + \frac{i_{dc}(t)}{C_{dc}}. \tag{3.112}$$

On the other hand, if Equations (3.107),(3.108) and (3.110) are replaced in Equation (3.106), the following equation can be written.

$$i_{dc}(t)\bar{v}_{dc}(t) = \left[C_{dc}\frac{d}{dt}\bar{v}_{dc}(t)\right]\bar{v}_{dc}(t) + \frac{3\bar{v}_{dc}(t)}{4}\left[m_d(t)\bar{i}_d(t) + m_q(t)\bar{i}_q(t)\right]. \tag{3.113}$$

Once again, by dividing the entire equation by $v_{dc}(t)$ and collecting the terms, it is possible to write a differential equation describing the dynamic behavior of the DC capacitor, but in $dq$-frame this time.

$$\frac{d}{dt}\bar{v}_{dc}(t) = -\frac{3}{4C_{dc}}m_d(t)\bar{i}_d(t) - \frac{3}{4C_{dc}}m_q(t)\bar{i}_q(t) + \frac{i_{dc}(t)}{C_{dc}}. \tag{3.114}$$

Hence, if the model of a VSC is required in $\alpha\beta$-frame, it is possible to put Equations (3.101) and (3.112) to write the system of equations described in (3.115).

$$\begin{cases} \dfrac{d}{dt}\bar{i}_\alpha(t) = -\dfrac{R}{L}\bar{i}_\alpha(t) + \dfrac{\bar{v}_{dc}(t)}{2L}m_\alpha(t) - \dfrac{1}{L}\bar{v}_{g,\alpha}(t), \\ \dfrac{d}{dt}\bar{i}_\beta(t) = -\dfrac{R}{L}\bar{i}_\beta(t) + \dfrac{\bar{v}_{dc}(t)}{2L}m_\beta(t) - \dfrac{1}{L}\bar{v}_{g,\beta}(t), \\ \dfrac{d}{dt}\bar{v}_{dc}(t) = -\dfrac{3}{4C_{dc}}m_\alpha(t)\bar{i}_\alpha(t) - \dfrac{3}{4C_{dc}}m_\beta(t)\bar{i}_\beta(t) + \dfrac{i_{dc}(t)}{C_{dc}}. \end{cases} \tag{3.115}$$

If the $dq$-frame model is required, it is necessary to put Equations (3.105) and (3.114) to write Equation (3.116).

$$\begin{cases} \dfrac{d}{dt}\bar{i}_d(t) = -\dfrac{R}{L}\bar{i}_d(t) + \omega(t)\bar{i}_q(t) + \dfrac{\bar{v}_{dc}(t)}{2L}m_d(t) - \dfrac{1}{L}\bar{v}_{g,d}(t), \\ \dfrac{d}{dt}\bar{i}_q(t) = -\omega(t)\bar{i}_d(t) - \dfrac{R}{L}\bar{i}_q(t) + \dfrac{\bar{v}_{dc}(t)}{2L}m_q(t) - \dfrac{1}{L}\bar{v}_{g,q}(t), \\ \dfrac{d}{dt}\bar{v}_{dc}(t) = -\dfrac{3}{4C_{dc}}m_d(t)\bar{i}_d(t) - \dfrac{3}{4C_{dc}}m_q(t)\bar{i}_q(t) + \dfrac{i_{dc}(t)}{C_{dc}}. \end{cases} \tag{3.116}$$

Note that Equations (3.115) and (3.116) have multiplications between control variables and state variables and, thus, both system of equations are considered to be nonlinear. In addition, this study is focused on control using $dq$-frame and, therefore, system (3.116) will be the only set of equations describing the VSC dynamic behavior that will be considered from now on.

## 3.5 BACK-TO-BACK CONVERTER

The Back-To-Back (BTB) converter is very straight forward to describe. Two VSCs are connected, back-to-back, having one common DC link and capacitor between them. A BTB converter connecting two different AC systems is depicted in Figure 18.

If the two AC systems are independent, the mathematical dynamical model of each VSC is rather simple to be obtained. Each converter can be modeled as an independent VSC, as described in set of equations (3.105). Hence, the AC dynamic for each VSC in $dq$-frame can be written as

Figure 18 – Diagram representing the BTB-VSC interconnecting systems 1 and 2.

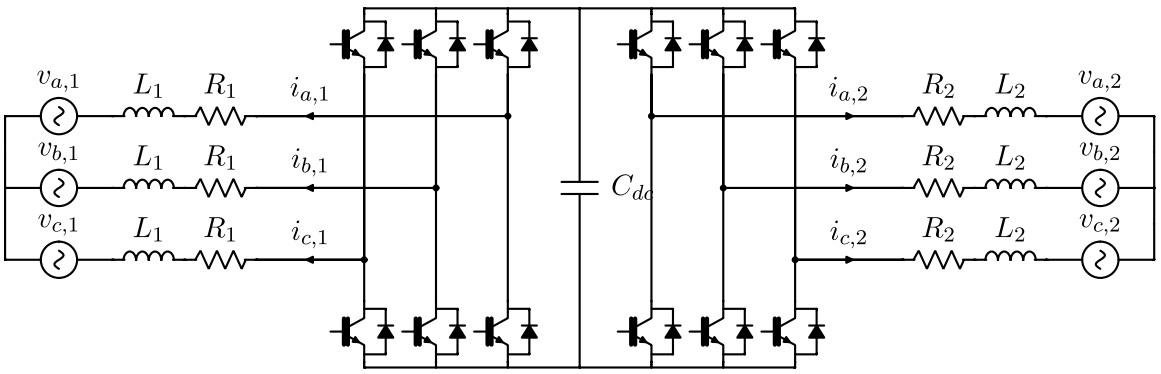


Source: Author (2022).

$$\begin{cases} \frac{d}{dt}\bar{i}_{d,1}(t) = -\frac{R_1}{L_1}\bar{i}_{d,1}(t) + \omega_1(t)\bar{i}_q(t) + \frac{\bar{v}_{dc}(t)}{2L_1}m_{d,1}(t) - \frac{1}{L_1}\bar{v}_{g,d,1}(t), \\ \frac{d}{dt}\bar{i}_{q,1}(t) = -\omega_1(t)\bar{i}_{d,1}(t) - \frac{R_1}{L_1}\bar{i}_{q,1}(t) + \frac{\bar{v}_{dc}(t)}{2L_1}m_{q,1}(t) - \frac{1}{L_1}\bar{v}_{g,q,1}(t), \\ \frac{d}{dt}\bar{i}_{d,2}(t) = -\frac{R_2}{L_2}\bar{i}_{d,2}(t) + \omega_2(t)\bar{i}_{q,2}(t) + \frac{\bar{v}_{dc}(t)}{2L_2}m_{d,2}(t) - \frac{1}{L_2}\bar{v}_{g,d,2}(t), \\ \frac{d}{dt}\bar{i}_{q,2}(t) = -\omega_2(t)\bar{i}_{d,2}(t) - \frac{R_2}{L_2}\bar{i}_{q,2}(t) + \frac{\bar{v}_{dc}(t)}{2L_2}m_{q,2}(t) - \frac{1}{L_2}\bar{v}_{g,q,2}(t). \end{cases} \tag{3.117}$$

Note that there's only one equation missing: the equation that determines the dynamic behavior of the DC capacitor. In order to find such equation it is, once again, necessary to look into the power flowing through the converter, as it was done with the VSC. This time, the power flow through the BTB is depicted by Figure 19. Note that the power coming out of VSC 1, $P_1$, going to the capacitor, $P_{cap}$, and the power going out of VSC 2, $P_2$, add up to be equal to zero.

Figure 19 – Diagram showing the power flow through the BTB-VSC.

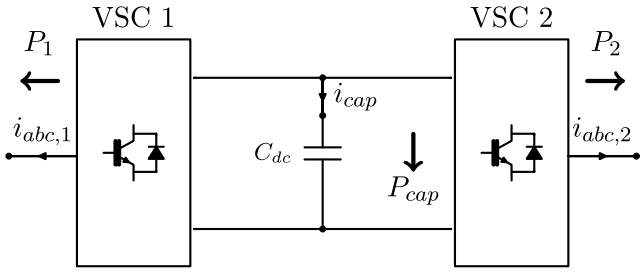


Source: Author (2022).

Based on this Figure, it is easy to write the following power balance equation

$$P_1 + P_{cap} + P_2 = 0. \tag{3.118}$$

The power flowing out of each converter can be written using Equation (3.110), while the power flowing through the capacitor can be described, once again, by (3.108). Hence, it is possible to rewrite Equation (3.118) as

$$\begin{aligned}&\frac{3\bar{v}_{dc}(t)}{4}\left[m_{d,1}(t)\bar{i}_{d,1}(t) + m_{q,1}(t)\bar{i}_{q,1}(t)\right] + \left[C_{dc}\frac{d}{dt}\bar{v}_{dc}(t)\right]\bar{v}_{dc}(t) + \\ &+\frac{3\bar{v}_{dc}(t)}{4}\left[m_{d,2}(t)\bar{i}_{d,2}(t) + m_{q,2}(t)\bar{i}_{q,2}(t)\right] = 0.\end{aligned} \tag{3.119}$$

By dividing the entire equation by $C_{dc}v_{dc}(t)$ and collecting the terms, it is possible to write a differential equation describing the dynamic behavior of the DC capacitor of the BTB converter, in $dq$-frame.

$$\frac{d}{dt}\bar{v}_{dc}(t) = -\frac{3m_{d,1}(t)}{4C_{dc}}\bar{i}_{d,1}(t) - \frac{3m_{q,1}(t)}{4C_{dc}}\bar{i}_{q,1}(t) - \frac{3m_{d,2}(t)}{4C_{dc}}\bar{i}_{d,2}(t) - \frac{3m_{q,2}(t)}{4C_{dc}}\bar{i}_{q,2}(t). \tag{3.120}$$

Hence, the set of equations that describes the dynamical behavior of a BTB converter can be written when putting together equations (3.120) and (3.117), as it is shown in

$$\begin{cases}\dfrac{d}{dt}\bar{i}_{d,1}(t) = -\dfrac{R_1}{L_1}\bar{i}_{d,1}(t) + \omega_1(t)\bar{i}_q(t) + \dfrac{\bar{v}_{dc}(t)}{2L_1}m_{d,1}(t) - \dfrac{1}{L_1}\bar{v}_{g,d,1}(t), \\ \dfrac{d}{dt}\bar{i}_{q,1}(t) = -\omega_1(t)\bar{i}_{d,1}(t) - \dfrac{R_1}{L_1}\bar{i}_{q,1}(t) + \dfrac{\bar{v}_{dc}(t)}{2L_1}m_{q,1}(t) - \dfrac{1}{L_1}\bar{v}_{g,q,1}(t), \\ \dfrac{d}{dt}\bar{v}_{dc}(t) = -\dfrac{3m_{d,1}(t)}{4C_{dc}}\bar{i}_{d,1}(t) - \dfrac{3m_{q,1}(t)}{4C_{dc}}\bar{i}_{q,1}(t) - \dfrac{3m_{d,2}(t)}{4C_{dc}}\bar{i}_{d,2}(t) - \dfrac{3m_{q,2}(t)}{4C_{dc}}\bar{i}_{q,2}(t), \\ \dfrac{d}{dt}\bar{i}_{d,2}(t) = -\dfrac{R_2}{L_2}\bar{i}_{d,2}(t) + \omega_2(t)\bar{i}_{q,2}(t) + \dfrac{\bar{v}_{dc}(t)}{2L_2}m_{d,2}(t) - \dfrac{1}{L_2}\bar{v}_{g,d,2}(t), \\ \dfrac{d}{dt}\bar{i}_{q,2}(t) = -\omega_2(t)\bar{i}_{d,2}(t) - \dfrac{R_2}{L_2}\bar{i}_{q,2}(t) + \dfrac{\bar{v}_{dc}(t)}{2L_2}m_{q,2}(t) - \dfrac{1}{L_2}\bar{v}_{g,q,2}(t).\end{cases} \tag{3.121}$$

## 3.6 PHASE-LOCKED LOOP

The controllers for all converters studied here are designed in synchronous reference frame, i.e., $dq$-frame. In this coordinate system, the representation of quantities in $d$ and $q$ axis are expected to be stationary under steady state condition (ALMEIDA, 2011; YAZDANI; IRAVANI, 2010). In order to be able to create such control systems, it is

necessary to leverage some special devices called Phase-Locked Loop (PLL) systems. Although PLLs are absolutely fundamental for the development of control systems in $dq$-axis, the main purpose of the PLL system is to synchronize the quantities synthesized by the converter to the respective quantities observed in the grid in which the converter is connected.

Because of these important functions, PLLs have been extensively studied and their implementation scrutinized in the past decades. Therefore, this section aims to briefly describe one robust and easy-to-implement technique that has been quite successful in many different applications. The rather simple PLL structure presented here is, indeed, shown to reject distortions while detecting the correct positive sequence component. In addition, the system has a robust performance even under unbalanced conditions (LIMONGI *et al.*, 2007).

The system presented here is the DSOGI-PLL (RODRIGUEZ *et al.*, 2006) and it has mainly two components: the Synchronous Reference Frame PLL (SRF-PLL) structure and the Double Second Order Generalized Integrator (DSOGI). First, let us describe the former.

### 3.6.1 **Synchronous Reference Frame Based Design**

This PLL's first structure is actually its core. In grid-connected converters, the SRF-PLL is used to find frequency and phase of the grid's voltage. This allows the converter to synthesize its quantities accordingly and in synchrony with the grid. The mechanism behind its working procedure lies in the Synchronous Reference Frame or, the $dq$ space. As it was previously mentioned, the Park transform is designed in a way that the axes move at the same speed as the voltage quantities. When this happens, the decomposition of the voltage quantities becomes quasi-static and the representation of the quantities becomes stationary. In addition to that, a compensator $C_{PI}(s)$ is used in order to find the $\rho$ angle used in Park transform in order to synchronize the $q$ axis in such way that the voltage quantity is completely aligned with the $d$ axis, leaving the $q$ component null.

Figure 20 depicts the usual SRF structure. Note that the compensator is placed on the $q$ axis in order to make it to be 0 in steady state. The compensator used in an SRF can be as simple as a proportional-integral compensator that will drive the error ($q$ quantity) to zero.

In order to tune the parameters for the compensator is necessary to, first, understand the $dq$ quantities outputted by the $\alpha\beta$-block. They can be described as

Figure 20 – Diagram representing a PLL based on Synchronous Reference Frame (SRF).

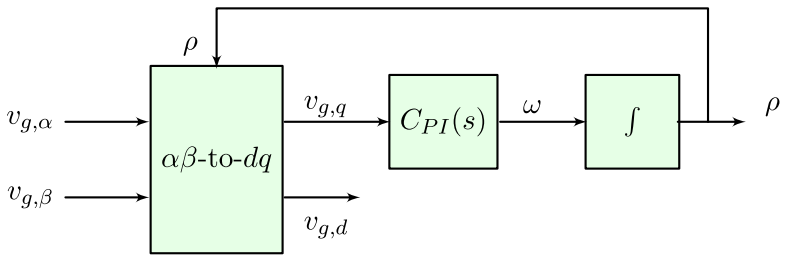


Source: Author (2022).

$$\begin{cases} v_{g,d} &= \hat{V}_g \cos\left(\omega_g t + \phi_v - \rho\right), \\ v_{g,q} &= \hat{V}_g \sin\left(\omega_g t + \phi_v - \rho\right), \end{cases} \tag{3.122}$$

where $\hat{V}_g$ is the amplitude of the grid's voltage, $\omega_g$ is the grid's angular frequency and $\phi_v$ is the voltage's fundamental component phase. The compensator should then be such that it can track the following equation

$$\rho = \omega_g t + \phi_v. \tag{3.123}$$

If this is done successfully, the $dq$ quantities become

$$\begin{cases} v_{g,d} &= \hat{V}_g \cos\left(\omega_g t + \phi_v - \rho\right) = \hat{V}_g \cos\left(0\right) = \hat{V}_g, \\ v_{g,q} &= \hat{V}_g \sin\left(\omega_g t + \phi_v - \rho\right) = \hat{V}_g \sin\left(0\right) = 0. \end{cases} \tag{3.124}$$

If the controller's transfer function is determined by

$$C_{PI}(s) = K_{pi}\left(1 + \frac{1}{sT_{pi}}\right), \tag{3.125}$$

and by using the linear approximation which considers that $\rho \approx \omega_g t + \phi_v$, we can write the closed loop transfer function as

$$G_{PLL}(s) = \frac{K_{pi}\left(1 + \dfrac{1}{sT_{pi}}\right)\hat{V}_g}{s + K_{pi}\left(1 + \dfrac{1}{sT_{pi}}\right)\hat{V}_g} = \frac{K_{pi}\hat{V}_g s + \frac{K_{pi}\hat{V}_g}{T_{pi}}}{s^2 + K_{pi}\hat{V}_g s + \frac{K_{pi}\hat{V}_g}{T_{pi}}}. \tag{3.126}$$

All the details of this process and an in depth discussion on how to tune the parameters of an SRF are available at (ALMEIDA, 2011). The main idea is that Eq. (3.126) can be compared to the following transfer function

$$G(s) = \frac{2\xi\omega_n s + \omega_n^2}{s^2 + 2\xi\omega_n s + \omega_n^2}, \tag{3.127}$$

where $\omega_n$ is the undamped natural frequency and $\xi$ represents the damping. Comparing Equations (3.126) and (3.127), it is possible to obtain the following relation.

$$\begin{cases} K_{pi} = \dfrac{2\omega_n\xi}{\hat{V}_g}, \\ T_{pi} = \dfrac{K_{pi}\hat{V}_g}{\omega_n^2}. \end{cases} \tag{3.128}$$

It is also important to note that a good dynamic performance can be achieved with $\xi = 0.7$ and $\omega_n = 100$ radians per second (ALMEIDA, 2011).

### 3.6.2 **Double Second Order Generalized Integrator**

The SRF-PLL described in the previous subsection performs really well when the voltage is balanced and has very low distortion. However, this is not encountered in practical scenarios. Especially considering the fact that voltage measured in the Point of Common Coupling (PCC) presents distortions coming from the connection with the VSC. Hence, it is desireable to add some robustness in the SRF structure. This is done by adding two band-pass filters called Second Order Generalized Integrator (SOGI) in order to filter fundamental components the $\alpha$ and $\beta$ quantities calculated from measured values. The common structure for a SOGI is presented in Figure 21. Note that it has two outputs: $v'_{\alpha\beta}$ and $qv'_{\alpha\beta}$. The first is supposed to be the component of $v_{\alpha\beta}$ in $\omega_r$ and the latter is quadrature version of the first output, but lagging in 90 degrees.

The parameters $\omega_r$ and $k$ can be set for the desired performance. Since this band-pass system is used to filter the fundamental component of $\alpha$ and $\beta$ axes, it is reasonable to think that $\omega_r$ should correspond to the fundamental angular frequency of the grid $\omega_r = 2\pi 60 \approx 376.99$. In addition, this band-pass filter could have an adaptive structure, where $\omega_r$ comes from the SRF (RODRIGUEZ *et al.*, 2006). In this present study, $\omega_r$ is kept constant in $\omega_r = 377$. Moreover, the performance of the SOGI filter can be improved by choosing a good value for $k$. In (ALMEIDA, 2011) and in (RODRIGUEZ *et al.*, 2006) analyses are conducted and, in both, it is concluded that $k = \sqrt{2}$ is, indeed, an appropriate value for the gain.

Furthermore, if one SOGI is deployed in the $\alpha$ axis and another one in $\beta$ axis, then a positive sequence circuit detector can be easily implemented. The analysis for such

Figure 21 – Diagram representing a Second Order Generalized Integrator (SOGI).

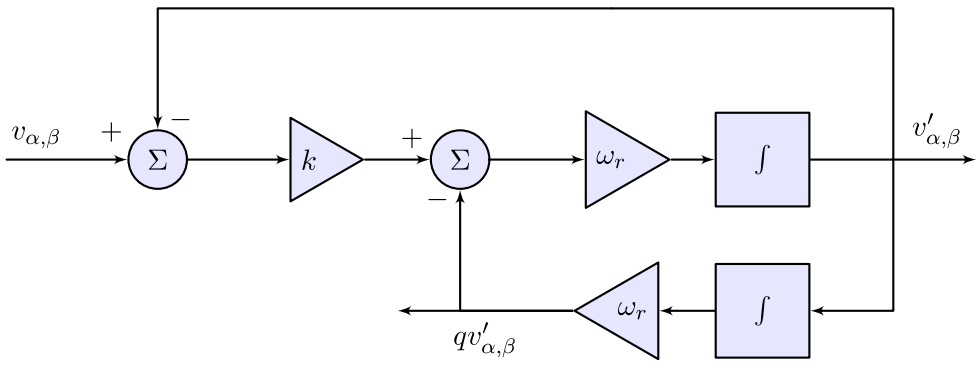


Source: Author (2022).

circuit is presented in (ALMEIDA, 2011) and in (RODRIGUEZ *et al.*, 2006) and only the final result will be presented here. It is possible to demonstrate mathematically that

$$v_{\alpha}^{+} = \frac{1}{2}\left(v'_{\alpha} - qv'_{\beta}\right), \tag{3.129}$$

$$v_{\beta}^{+} = \frac{1}{2}\left(v'_{\beta} - qv'_{\alpha}\right), \tag{3.130}$$

where $v_{\alpha}^{+}$ and $v_{\beta}^{+}$ are the positive sequence components in $\alpha-$ and $\beta-$axis, respectively.

### 3.6.3 **DSOGI-PLL**

The DSOGI-PLL (RODRIGUEZ *et al.*, 2006) can finally be assembled by combining the structures presented previously and its structure is presented in Figure 22. Note that Double SOGI (DSOGI) architecture is used in order to filter the fundamental component of $\alpha-$ and $\beta-$axis from the grid voltage. The outputs from DSOGI structure are used to compute the positive sequence component in $\alpha-$ and $\beta-$axis which are then used as input in the SRF-based PLL. This structure is found to be robust and to perform well under different types of disturbances, unbalances and distortions (ALMEIDA, 2011; RODRIGUEZ *et al.*, 2006) and, therefore, it is the PLL structure used in this work.

Figure 22 – Diagram for the Double SOGI-based SRF-PLL (DSOGI-PLL).

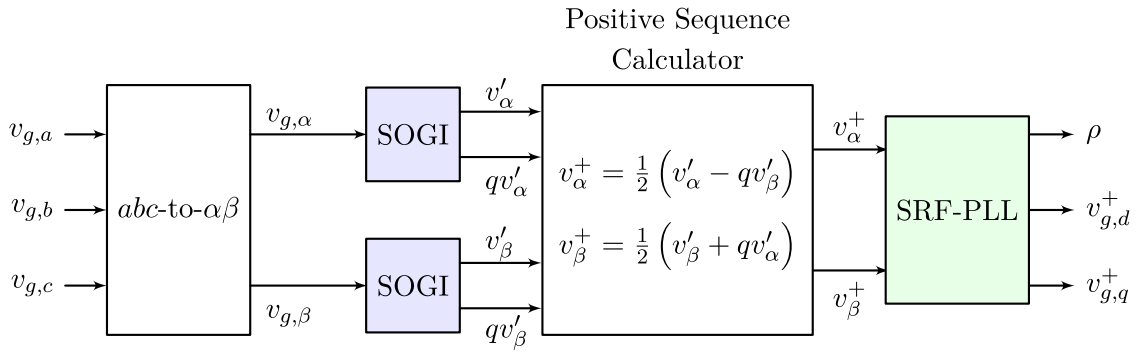


Source: Author (2022).

# 4 LINEAR SYSTEMS AND LINEAR CONTROL

This chapter aims at using the outcomes from previous chapters, especially the models for single VSC and BTB converter, in order to obtain linear models that are appropriate for the control techniques that are presented here. To address this goal, the chapter first presents the single VSC model together with its linearization, the control strategy modeling and the final augmented state-space system, which condenses not only the dynamic process of the converter but also the controller dynamics in one single linear representation. Later on, the BTB converter undergoes the same procedure, resulting in an augmented system representing not only the BTB converter but its controllers as well. Finally, the chapter presents linear control strategies that have major importance for this study, i.e., Linear Quadratic Regulators and LMI-based Robust Pole Placement strategies. The outcomes of this chapter are promptly used in the following steps of this research which are presented in the next chapter.

## 4.1 SINGLE VSC

This first section starts by using the single VSC converter model which is presented in the previous chapters. The linearization procedure is succeded by the selection of control signals, the description of its linear representation in state variables and the incorporation of the controller into the system's linear representation, resulting in an augmented system. This augmented representation is then used in the controller design procedure that has its fundamentals presented in the third section of this chapter.

### 4.1.1 Equilibrum and Linearization

Consider the system of dynamic equations that is presented in (3.116) and is now re-written in (4.1). Note that the frequency $\omega(t)$ is now represented as a constant value, meaning that the frequency imposed by the grid is considered to be constant during the analysis period or to have negligible variance. Moreover, note that the states are $\bar{i}_d(t)$, $\bar{i}_q(t)$ and $\bar{v}_{dc}(t)$; the control variables are $m_d(t)$ and $m_q(t)$; the variables $\bar{v}_{g,d}(t)$, $\bar{v}_{g,q}(t)$ and $i_{dc}(t)$ are considered to be disturbances to the VSC system.

$$\begin{cases} \dfrac{d}{dt}\bar{i}_d(t) = -\dfrac{R}{L}\bar{i}_d(t) + \omega\bar{i}_q(t) + \dfrac{\bar{v}_{dc}(t)}{2L}m_d(t) - \dfrac{1}{L}\bar{v}_{g,d}(t), \\ \dfrac{d}{dt}\bar{i}_q(t) = -\omega\bar{i}_d(t) - \dfrac{R}{L}\bar{i}_q(t) + \dfrac{\bar{v}_{dc}(t)}{2L}m_q(t) - \dfrac{1}{L}\bar{v}_{g,q}(t), \\ \dfrac{d}{dt}\bar{v}_{dc}(t) = -\dfrac{3}{4C_{dc}}m_d(t)\bar{i}_d(t) - \dfrac{3}{4C_{dc}}m_q(t)\bar{i}_q(t) + \dfrac{i_{dc}(t)}{C_{dc}}. \end{cases} \tag{4.1}$$

In last subsection the system model was shown to be nonlinear and, in order to use linear controllers, it is necessary to linearize the equations. The nonlinear system

can have its dynamic behavior approximated to a linear system in a region around the equilibrium (KHALIL; GRIZZLE, 2002). Therefore, for the linearization process the value of any variables in the linearized operation point is needed. In addition, any averaged variable (state, input or disturbance) $\bar{z}(t)$ can be written as the sum of its steady state component $Z$ with its small-signal variation $\tilde{z}(t)$.

$$\bar{z}(t) = Z + \tilde{z}(t) \Rightarrow \tilde{z}(t) = \bar{z}(t) - Z. \tag{4.2}$$

Recall that

$$\frac{d}{dt}\bar{z}(t) = \frac{d}{dt}\left(Z + \tilde{z}\right) = \frac{d}{dt}\tilde{z}. \tag{4.3}$$

Also recall that, derivative terms are equal to zero at the equilibrium point, and, hence, the states, inputs and disturbances can be calculated using only their steady state values for obtaining the equlibrium point. By using an appropriate PLL system such as the one described in Subsection 3.6.1, quadrature axis voltage $V_{g,q}$ is equal to zero while the direct axis voltage $V_{g,d}$ is equal to the peak value of the wave in steady state (RODRIGUEZ *et al.*, 2006). The voltage over the capacitor $V_{dc}$ is kept constant in the operation of the BTB in a predetermined value. Furthermore, in this study, the reference value of reactive power is set to be zero. Hence, the quadrature current $I_q$ is also equal to zero as it is shown in Eq. (3.48) (YAZDANI; IRAVANI, 2010). The initial DC current $I_{dc}$ is the last variable that is needed for finding the equilibrium point and it must be known beforehand. Hence, all the other missing variables can be calculated as listed in Eq. (4.4) (SUNTIO; MESSO; PUUKKO, 2017).

$$\begin{cases} M_d = \dfrac{V_{g,d} + \sqrt{(\frac{8}{3})I_{dc}V_{dc}R + V_{g,d}^2}}{V_{dc}}, \\ I_d = \dfrac{4I_{dc}}{3M_d}, \\ M_q = \dfrac{2LI_d\omega}{V_{dc}}. \end{cases} \tag{4.4}$$

Using all assumptions described above, the system can be linearized around a determined equilibrium point given by grid and the converter's parameters and the DC bus current $I_{dc}$. The resulting set of equations, written in a state-space representation,

that shows the small-signal behavior for the whole system is shown in equation (4.5).

$$\frac{d}{dt}\begin{bmatrix}\tilde{i}_d\\ \tilde{i}_q\\ \tilde{v}_{dc}\end{bmatrix} = \begin{bmatrix}-\frac{R}{L} & \omega & \frac{M_d}{2L}\\ -\omega & -\frac{R}{L} & \frac{M_q}{2L}\\ -\frac{3M_d}{4C_{dc}} & -\frac{3M_q}{4C_{dc}} & 0\end{bmatrix}\begin{bmatrix}\tilde{i}_d\\ \tilde{i}_q\\ \tilde{v}_{dc}\end{bmatrix} + \begin{bmatrix}\frac{V_{dc}}{2L} & 0\\ 0 & \frac{V_{dc}}{2L}\\ -\frac{3I_d}{4C_{dc}} & -\frac{3I_q}{4C_{dc}}\end{bmatrix}\begin{bmatrix}\tilde{m}_d\\ \tilde{m}_q\end{bmatrix} + \begin{bmatrix}0 & -\frac{1}{L} & 0\\ 0 & 0 & -\frac{1}{L}\\ \frac{1}{C_{dc}} & 0 & 0\end{bmatrix}\begin{bmatrix}\tilde{i}_{dc}\\ \tilde{v}_{g,d}\\ \tilde{v}_{g,q}\end{bmatrix}. \tag{4.5}$$

### 4.1.2 **Modeling Integral Action and Control Variables**

The model is written using a synchronous reference frame and hence, all variables that had a sine-like oscillatory natural behavior, such as average terminal voltage and currents have now a stationary behavior. This means that, instead of using resonant controllers which are able to meet sinusoidal references, the designed controllers must be able to follow a stationary-value reference (YAZDANI; IRAVANI, 2010). According to the internal model principle (LIU; YAO, 2016), just an integral action is sufficient to meet a null steady state error condition. In this study, variables $\bar{i}_q$ and $\bar{v}_{dc}$ are going to be controlled for meeting an appropriate reference. The $q-$ axis current has its value proportional to reactive power being injected by the converter at the point of common coupling (YAZDANI; IRAVANI, 2010). The DC bus voltage indirectly controls the $d-$axis current and, in relatively lower frequencies, such as the grid's synchronous frequency, it is the most appropriate variable to be controlled (SOUZA *et al.*, 2021). The DC bus voltage is usually controlled to have its value constant throughout the entire time, allowing a stable and safe operation for the power-electronic converters. In addition, recall that there are two controlled variables because there are two control actions, the modulation indices $\tilde{m}_d$ and $\tilde{m}_q$.

Consider now the $q-$axis control loop, where an integral action is used to reduce the steady-state error to zero. The block diagram that represents this action is shown in Figure 23 . Note that $\dot{x}_1$ is the error between averaged quadrature-axis output current reference value, $\bar{i}_q^*$ and the measured averaged value.

Hence, it is possible to translate the block diagram into an equation as in

$$\dot{x}_1 = \bar{i}_q^* - \bar{i}_q = \bar{i}_q^* - (I_q + \tilde{i}_q). \tag{4.6}$$

where overscript ( $^*$ ) means the reference value. Similarly, it is possible to write an analogous equation for the DC bus voltage as it is shown in Equation (4.7).

$$\dot{x}_2 = \bar{v}_{dc}^* - \bar{v}_{dc} = \bar{v}_{dc}^* - (V_{dc} + \tilde{v}_{dc}). \tag{4.7}$$

Figure 23 – Diagram representing an integrator control for the $q-$axis current.

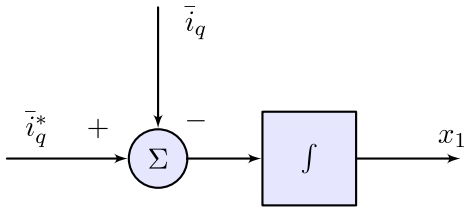


Source: Author (2022).

Equations (4.6) and (4.7) can be rewritten with a state-space representation as it is shown in equation (4.8)

$$\frac{d}{dt}\begin{bmatrix} x_1 \\ x_2 \end{bmatrix} = \begin{bmatrix} 0 & -1 & 0 \\ 0 & 0 & -1 \end{bmatrix}\begin{bmatrix} \tilde{i}_d \\ \tilde{i}_q \\ \tilde{v}_{dc} \end{bmatrix} + \begin{bmatrix} 1 & 0 \\ 0 & 1 \end{bmatrix}\begin{bmatrix} \bar{i}_q^* - I_q \\ \bar{v}_{dc}^* - V_{dc} \end{bmatrix}. \tag{4.8}$$

Moreover, note that variables $\tilde{v}_{g,d}$ and $\tilde{v}_{g,q}$ are outputs of the PLL system and, therefore, these variables that are normally associated with disturbances to the system can be readily used in a feed-forward scheme. In fact, suppose that

$$\begin{cases} \tilde{m}_d = \tilde{u}_d + \dfrac{2}{V_{dc}}\tilde{v}_{g,d}, \\ \\ \tilde{m}_q = \tilde{u}_q + \dfrac{2}{V_{dc}}\tilde{v}_{g,q}. \end{cases} \tag{4.9}$$

in which $\tilde{u}_d$ and $\tilde{u}_q$ are the auxiliary new control variables. Hence, the system becomes more resilient against disturbances coming from the AC grid side, as shown in Equation (4.10).

$$\begin{bmatrix} \frac{V_{dc}}{2L} & 0 \\ 0 & \frac{V_{dc}}{2L} \\ -\frac{3I_d}{4C_{dc}} & -\frac{3I_q}{4C_{dc}} \end{bmatrix}\begin{bmatrix} \tilde{m}_d \\ \tilde{m}_q \end{bmatrix} + \begin{bmatrix} 0 & -\frac{1}{L} & 0 \\ 0 & 0 & -\frac{1}{L} \\ \frac{1}{C_{dc}} & 0 & 0 \end{bmatrix}\begin{bmatrix} \tilde{i}_{in} \\ \tilde{v}_{g,d} \\ \tilde{v}_{g,q} \end{bmatrix} = \begin{bmatrix} \frac{V_{dc}}{2L} & 0 \\ 0 & \frac{V_{dc}}{2L} \\ -\frac{3I_d}{4C_{dc}} & -\frac{3I_q}{4C_{dc}} \end{bmatrix}\begin{bmatrix} \tilde{u}_d \\ \tilde{u}_q \end{bmatrix} + \begin{bmatrix} 0 \\ 0 \\ \frac{1}{C_{dc}} \end{bmatrix}\tilde{i}_{dc}. \tag{4.10}$$

### 4.1.3 **Augmented System**

Now that the controller action is also written in state-space form, it is possible to integrate its matrix equation into the system's dynamic behaviorial equations. This is

done by augmenting the original linear system presented in Eq. (4.5) for including Eq. (4.8). In addition to that, it is also interesting to change the control variables to $\tilde{u}_d$ and $\tilde{u}_q$ from Eq. (4.9) in order to be less susceptible to disturbances, as shown in Eq. (4.10). Therefore combination of all equations results in the augmented system matrix equation shown in (4.11).

$$\begin{aligned}\frac{d}{dt}\begin{bmatrix}\tilde{i}_d\\ \tilde{i}_q\\ \tilde{v}_{dc}\\ x_1\\ x_2\end{bmatrix} = &\overbrace{\begin{bmatrix}-\frac{R}{L} & \omega & \frac{M_d}{2L} & 0 & 0\\ -\omega & -\frac{R}{L} & \frac{M_q}{2L} & 0 & 0\\ -\frac{3M_d}{4C} & -\frac{3M_q}{4C} & 0 & 0 & 0\\ 0 & -1 & 0 & 0 & 0\\ 0 & 0 & -1 & 0 & 0\end{bmatrix}}^{\mathbf{A_{vsc}}}\overbrace{\begin{bmatrix}\tilde{i}_d\\ \tilde{i}_q\\ \tilde{v}_{dc}\\ x_1\\ x_2\end{bmatrix}}^{\mathbf{x_{vsc}}} + \overbrace{\begin{bmatrix}\frac{V_{dc}}{2L} & 0\\ 0 & \frac{V_{dc}}{2L}\\ -\frac{3I_d}{4C} & -\frac{3I_q}{4C}\\ 0 & 0\\ 0 & 0\end{bmatrix}}^{\mathbf{B_{vsc}}}\overbrace{\begin{bmatrix}\tilde{u}_d\\ \tilde{u}_q\end{bmatrix}}^{\mathbf{u_{vsc}}}\\ &+\overbrace{\begin{bmatrix}0 & 0 & 0\\ 0 & 0 & 0\\ 0 & 0 & \frac{1}{C}\\ 1 & 0 & 0\\ 0 & 1 & 0\end{bmatrix}}^{\mathbf{F_{vsc}}}\overbrace{\begin{bmatrix}\bar{i}_q^* - I_q\\ \bar{v}_{dc}^* - V_{dc}\\ \tilde{i}_{dc}\end{bmatrix}}^{\mathbf{v_{vsc}}}.\end{aligned} \tag{4.11}$$

In addition to that, it is necessary to find an output matrix that represents the quantities that are being measured in our system. For this particular study, all augmented states can be directly measured and, therefore, the outputs can be determined as

$$\overbrace{\begin{bmatrix}y_{vsc,1}\\ y_{vsc,2}\\ y_{vsc,3}\\ y_{vsc,4}\\ y_{vsc,5}\end{bmatrix}}^{\mathbf{y_{vsc}}} = \overbrace{\begin{bmatrix}1 & 0 & 0 & 0 & 0\\ 0 & 1 & 0 & 0 & 0\\ 0 & 0 & 1 & 0 & 0\\ 0 & 0 & 0 & 1 & 0\\ 0 & 0 & 0 & 0 & 1\end{bmatrix}}^{\mathbf{C_{vsc}}}\overbrace{\begin{bmatrix}\tilde{i}_d\\ \tilde{i}_q\\ \tilde{v}_{dc}\\ x_1\\ x_2\end{bmatrix}}^{\mathbf{x_{vsc}}}. \tag{4.12}$$

where the subscript **vsc** is used to identify the set of matrices that is used for the single VSC system presented in this subsection. Both Equations (4.11) and (4.12) are used in posterior analyses for designing and tuning the VSC controller. In fact, note that it is possible to write the system of equations shown in (4.13).

$$\begin{cases}\dot{\mathbf{x}}_{\mathbf{vsc}} &= \mathbf{A_{vsc}x_{vsc}} + \mathbf{B_{vsc}u_{vsc}} + \mathbf{F_{vsc}v_{vsc}},\\ \mathbf{y_{vsc}} &= \mathbf{C_{vsc}x_{vsc}}.\end{cases} \tag{4.13}$$

## 4.2 BTB SYSTEM

Similarly to what is done with the single VSC system, this section aims at using the BTB model presented in previous chapters for obtaining a linear model that is ideal for the controller design. Besides that, a model for the integral action and the control variables is done and presented in its state-space representation. The combination of these two linear models results in an augmented system which is used in later chapters for an appropriate controller strategy implementation and tuning.

### 4.2.1 **Equilibrum and Linearization**

For the BTB, consider the set of Equations (3.121) which is now rewritten as (4.14). Note that angular frequencies from both BTB's sides are now considered to be constant and that the order of the equations is now restructured.

$$\begin{cases} \frac{d}{dt}\bar{i}_{d,1}(t) = -\frac{R_1}{L_1}\bar{i}_{d,1}(t) + \omega_1\bar{i}_q(t) + \frac{\bar{v}_{dc}(t)}{2L_1}m_{d,1}(t) - \frac{1}{L_1}\bar{v}_{g,d,1}(t), \\ \frac{d}{dt}\bar{i}_{q,1}(t) = -\omega_1\bar{i}_{d,1}(t) - \frac{R_1}{L_1}\bar{i}_{q,1}(t) + \frac{\bar{v}_{dc}(t)}{2L_1}m_{q,1}(t) - \frac{1}{L_1}\bar{v}_{g,q,1}(t), \\ \frac{d}{dt}\bar{i}_{d,2}(t) = -\frac{R_2}{L_2}\bar{i}_{d,2}(t) + \omega_2\bar{i}_{q,2}(t) + \frac{\bar{v}_{dc}(t)}{2L_2}m_{d,2}(t) - \frac{1}{L_2}\bar{v}_{g,d,2}(t), \\ \frac{d}{dt}\bar{i}_{q,2}(t) = -\omega_2\bar{i}_{d,2}(t) - \frac{R_2}{L_2}\bar{i}_{q,2}(t) + \frac{\bar{v}_{dc}(t)}{2L_2}m_{q,2}(t) - \frac{1}{L_2}\bar{v}_{g,q,2}(t), \\ \frac{d}{dt}\bar{v}_{dc}(t) = -\frac{3m_{d,1}(t)}{4C_{dc}}\bar{i}_{d,1}(t) - \frac{3m_{q,1}(t)}{4C_{dc}}\bar{i}_{q,1}(t) - \frac{3m_{d,2}(t)}{4C_{dc}}\bar{i}_{d,2}(t) - \frac{3m_{q,2}(t)}{4C_{dc}}\bar{i}_{q,2}(t). \end{cases} \tag{4.14}$$

This set of equation can then undergo the same procedure applied to the linearization of the single VSC, recalling that average values (denoted by a bar over the variable) can be written as the sum of their steady state component (denoted by capital letter) with its small-signal variation (denoted by the tilde over the variable). By using an appropriate PLL system, quadrature-axis voltages $V_{g,q,1}$ and $V_{g,q,2}$ measured at the point of common coupling are equal to zero while the direct axis voltages $V_{g,d,1}$ and $V_{g,d,2}$ are equal to the peak value of the phase-to-ground AC wave in steady state (RODRIGUEZ *et al.*, 2006). The voltage over the capacitor $V_{dc}$ is kept constant in the operation of the BTB in a predetermined value, guaranteeing a safe operation for both converters. In addition, in this study, the reference value of reactive power is set to be zero on both sides and, therefore, the quadrature-axis currents $I_{q,1}$ and $I_{q,2}$ are also equal to zero. Finally, by setting a power reference $P_1^*$, the steady state values of all other variables can be calculated as listed in

(4.15) (SUNTIO; MESSO; PUUKKO, 2017).

$$\begin{cases} I_{d,1} = \dfrac{2P_1^*}{3V_{g,d,1}}, \\ M_{d,1} = \dfrac{2V_{g,d,1} + 2R_1 I_{d,1}}{V_{dc}}, \\ M_{q,1} = \dfrac{2L_1 I_{d,1}\omega_1}{V_{dc}}, \\ M_{d,2} = \dfrac{V_{g,d,2} + \sqrt{V_{g,d,2}^2 + 2V_{dc}R_2 M_{d,1} I_{d,1}}}{V_{dc}}, \\ I_{d,2} = -\dfrac{M_{d,1} I_{d,1}}{M_{d,2}}, \\ M_{q,2} = \dfrac{2L_2 I_{d,2}\omega_2}{V_{dc}}. \end{cases} \tag{4.15}$$

By using the principles of linearization that are presented in previous chapters and recalling equations (4.2) and (4.3) that are applied to the single VSC example, it is possible to find the linear system presented in Equation (4.16). Note that, in this case, there are four control variables and five states. Grid voltage quantities can be interpreted as disturbances to the system's dynamics.

$$\begin{aligned} \frac{d}{dt}\begin{bmatrix} \tilde{i}_{d,1} \\ \tilde{i}_{q,1} \\ \tilde{i}_{d,2} \\ \tilde{i}_{q,2} \\ \tilde{v}_{dc} \end{bmatrix} = &\begin{bmatrix} -\frac{R_1}{L_1} & \omega_1 & 0 & 0 & \frac{M_{d,1}}{2L_1} \\ -\omega_1 & -\frac{R_1}{L_1} & 0 & 0 & \frac{M_{q,1}}{2L_1} \\ 0 & 0 & -\frac{R_2}{L_2} & \omega_2 & \frac{M_{d,2}}{2L_2} \\ 0 & 0 & -\omega_2 & -\frac{R_2}{L_2} & \frac{M_{q,2}}{2L_2} \\ -\frac{3M_{d,1}}{4C} & -\frac{3M_{q,1}}{4C} & -\frac{3M_{d,2}}{4C} & -\frac{3M_{q,2}}{4C} & 0 \end{bmatrix}\begin{bmatrix} \tilde{i}_{d,1} \\ \tilde{i}_{q,1} \\ \tilde{i}_{d,2} \\ \tilde{i}_{q,2} \\ \tilde{v}_{dc} \end{bmatrix} + \\ &+ \begin{bmatrix} \frac{V_{dc}}{2L_1} & 0 & 0 & 0 \\ 0 & \frac{V_{dc}}{2L_1} & 0 & 0 \\ 0 & 0 & \frac{V_{dc}}{2L_2} & 0 \\ 0 & 0 & 0 & \frac{V_{dc}}{2L_2} \\ -\frac{3I_{d,1}}{4C} & -\frac{3I_{q,1}}{4C} & -\frac{3I_{d,2}}{4C} & -\frac{3I_{q,2}}{4C} \end{bmatrix}\begin{bmatrix} \tilde{m}_{d,1} \\ \tilde{m}_{q,1} \\ \tilde{m}_{d,2} \\ \tilde{m}_{q,2} \end{bmatrix} + \begin{bmatrix} -\frac{1}{L_1} & 0 & 0 & 0 \\ 0 & -\frac{1}{L_1} & 0 & 0 \\ 0 & 0 & -\frac{1}{L_2} & 0 \\ 0 & 0 & 0 & -\frac{1}{L_2} \\ 0 & 0 & 0 & 0 \end{bmatrix}\begin{bmatrix} \tilde{v}_{g,d,1} \\ \tilde{v}_{g,q,1} \\ \tilde{v}_{g,d,2} \\ \tilde{v}_{g,q,2} \end{bmatrix}. \end{aligned} \tag{4.16}$$

### 4.2.2 **Modeling Integral Action and Control Variables**

Once again, it is important to recall that the model is written using a synchronous reference frame and, therefore, the designed controllers must be able to follow a stationary-value reference (YAZDANI; IRAVANI, 2010). Once again, an integral action is sufficient for meeting a null steady state error condition (LIU; YAO, 2016). In this study, the reactive power of both sides must be kept under the desired condition, which means that

$\bar{i}_{q,1}$ and $\bar{i}_{q,2}$ must be controlled. In addition, the voltage over the DC link, $\bar{v}_{dc}$ must be controlled to an appropriate constant value during the operation. Finally, it is necessary to meet a reference value for power set to one of the sides of the BTB converter. If the first side is chosen, the current $\bar{i}_{d,1}$ must be controlled, which is the case in this study. Therefore four integral actions are added for reducing steady state errors to zero and, once again, the controller state variable is chosen to be the output of the integral block acting on the error, just like in Figure 23. Hence, it is possible to write equation (4.17) for the controller.

$$\frac{d}{dt}\begin{bmatrix} x_1 \\ x_2 \\ x_3 \\ x_4 \end{bmatrix} = \begin{bmatrix} -1 & 0 & 0 & 0 & 0 \\ 0 & -1 & 0 & 0 & 0 \\ 0 & 0 & 0 & -1 & 0 \\ 0 & 0 & 0 & 0 & -1 \end{bmatrix} \begin{bmatrix} \tilde{i}_{d,1} \\ \tilde{i}_{q,1} \\ \tilde{i}_{d,2} \\ \tilde{i}_{q,2} \\ \tilde{v}_{dc} \end{bmatrix} + \begin{bmatrix} 1 & 0 & 0 & 0 \\ 0 & 1 & 0 & 0 \\ 0 & 0 & 1 & 0 \\ 0 & 0 & 0 & 1 \end{bmatrix} \begin{bmatrix} i^*_{d,1} - I_{d,1} \\ i^*_{q,1} - I_{q,1} \\ i^*_{q,2} - I_{q,2} \\ v^*_{dc} - V_{dc} \end{bmatrix}. \tag{4.17}$$

where over-script ( $^*$ ) means the reference value. Once again, note that variables corresponding to the voltage at the point of common coupling such as $\tilde{v}_{g,d,1}$, $\tilde{v}_{g,q,1}$, $\tilde{v}_{g,d,2}$ and $\tilde{v}_{g,q,2}$ are outputs of the PLL system. Thus they can be readily used in a feed-forward scheme as it was shown for the single VSC system. Therefore

$$\begin{cases} \tilde{m}_{d,1} = \tilde{u}_{d,1} + \dfrac{2}{V_{dc}}\tilde{v}_{g,d,1}, \\ \tilde{m}_{q,1} = \tilde{u}_{q,1} + \dfrac{2}{V_{dc}}\tilde{v}_{g,q,1}, \\ \tilde{m}_{d,2} = \tilde{u}_{d,2} + \dfrac{2}{V_{dc}}\tilde{v}_{g,d,2}, \\ \tilde{m}_{q,2} = \tilde{u}_{q,2} + \dfrac{2}{V_{dc}}\tilde{v}_{g,q,2}. \end{cases} \tag{4.18}$$

in which $\tilde{u}_{d,1}$ and $\tilde{u}_{q,1}$ are the auxiliary new control variables for VSC-1 and $\tilde{u}_{d,2}$ and $\tilde{u}_{q,2}$ are the new control variables for VSC-2. Hence, the system becomes more resilient against disturbances coming from the AC grid side. In fact, note that the term

$$\begin{bmatrix} \frac{V_{dc}}{2L_1} & 0 & 0 & 0 \\ 0 & \frac{V_{dc}}{2L_1} & 0 & 0 \\ 0 & 0 & \frac{V_{dc}}{2L_2} & 0 \\ 0 & 0 & 0 & \frac{V_{dc}}{2L_2} \\ -\frac{3I_{d,1}}{4C} & -\frac{3I_{q,1}}{4C} & -\frac{3I_{d,2}}{4C} & -\frac{3I_{q,2}}{4C} \end{bmatrix} \begin{bmatrix} \tilde{m}_{d,1} \\ \tilde{m}_{q,1} \\ \tilde{m}_{d,2} \\ \tilde{m}_{q,2} \end{bmatrix} + \begin{bmatrix} -\frac{1}{L_1} & 0 & 0 & 0 \\ 0 & -\frac{1}{L_1} & 0 & 0 \\ 0 & 0 & -\frac{1}{L_2} & 0 \\ 0 & 0 & 0 & -\frac{1}{L_2} \\ 0 & 0 & 0 & 0 \end{bmatrix} \begin{bmatrix} \tilde{v}_{g,d,1} \\ \tilde{v}_{g,q,1} \\ \tilde{v}_{g,d,2} \\ \tilde{v}_{g,q,2} \end{bmatrix} \tag{4.19}$$

can be simplified into the term

$$\begin{bmatrix} \frac{V_{dc}}{2L_1} & 0 & 0 & 0 \\ 0 & \frac{V_{dc}}{2L_1} & 0 & 0 \\ 0 & 0 & \frac{V_{dc}}{2L_2} & 0 \\ 0 & 0 & 0 & \frac{V_{dc}}{2L_2} \\ -\frac{3I_{d,1}}{4C} & -\frac{3I_{q,1}}{4C} & -\frac{3I_{d,2}}{4C} & -\frac{3I_{q,2}}{4C} \end{bmatrix} \begin{bmatrix} \tilde{u}_{d,1} \\ \tilde{u}_{q,1} \\ \tilde{u}_{d,2} \\ \tilde{u}_{q,2} \end{bmatrix}. \tag{4.20}$$

### 4.2.3 **Augmented System**

Now that the integral action has its dynamic behavior written in state-space form and the control variables are re-written, it is possible to expand the original system to include these modifications. Hence, the augmented state-space system can be written as it is shown in equation (4.21) below by combining equations (4.16), (4.17) and by noticing that (4.19) and (4.20) are equivalent.

$$\begin{aligned} \frac{d}{dt}\begin{bmatrix} \tilde{i}_{d,1} \\ \tilde{i}_{q,1} \\ \tilde{i}_{d,2} \\ \tilde{i}_{q,2} \\ \tilde{v}_{dc} \\ x_1 \\ x_2 \\ x_3 \\ x_4 \end{bmatrix} &= \overbrace{\begin{bmatrix} -\frac{R_1}{L_1} & \omega_1 & 0 & 0 & \frac{M_{d,1}}{2L_1} & 0 & 0 & 0 & 0 \\ -\omega_1 & -\frac{R_1}{L_1} & 0 & 0 & \frac{M_{q,1}}{2L_1} & 0 & 0 & 0 & 0 \\ 0 & 0 & -\frac{R_2}{L_2} & \omega_2 & \frac{M_{d,2}}{2L_2} & 0 & 0 & 0 & 0 \\ 0 & 0 & -\omega_2 & -\frac{R_2}{L_2} & \frac{M_{q,2}}{2L_2} & 0 & 0 & 0 & 0 \\ -\frac{3M_{d,1}}{4C} & -\frac{3M_{q,1}}{4C} & -\frac{3M_{d,2}}{4C} & -\frac{3M_{q,2}}{4C} & 0 & 0 & 0 & 0 & 0 \\ -1 & 0 & 0 & 0 & 0 & 0 & 0 & 0 & 0 \\ 0 & -1 & 0 & 0 & 0 & 0 & 0 & 0 & 0 \\ 0 & 0 & 0 & -1 & 0 & 0 & 0 & 0 & 0 \\ 0 & 0 & 0 & 0 & -1 & 0 & 0 & 0 & 0 \end{bmatrix}}^{\mathbf{A_{btb}}} \overbrace{\begin{bmatrix} \tilde{i}_{d,1} \\ \tilde{i}_{q,1} \\ \tilde{i}_{d,2} \\ \tilde{i}_{q,2} \\ \tilde{v}_{dc} \\ x_1 \\ x_2 \\ x_3 \\ x_4 \end{bmatrix}}^{\mathbf{x_{btb}}} + \\ &\overbrace{\begin{bmatrix} \frac{V_{dc}}{2L_1} & 0 & 0 & 0 \\ 0 & \frac{V_{dc}}{2L_1} & 0 & 0 \\ 0 & 0 & \frac{V_{dc}}{2L_2} & 0 \\ 0 & 0 & 0 & \frac{V_{dc}}{2L_2} \\ -\frac{3I_{d,1}}{4C} & -\frac{3I_{q,1}}{4C} & -\frac{3I_{d,2}}{4C} & -\frac{3I_{q,2}}{4C} \\ 0 & 0 & 0 & 0 \\ 0 & 0 & 0 & 0 \\ 0 & 0 & 0 & 0 \\ 0 & 0 & 0 & 0 \end{bmatrix}}^{\mathbf{B_{btb}}} \overbrace{\begin{bmatrix} \tilde{u}_{d,1} \\ \tilde{u}_{q,1} \\ \tilde{u}_{d,2} \\ \tilde{u}_{q,2} \end{bmatrix}}^{\mathbf{u_{btb}}} + \overbrace{\begin{bmatrix} 0 & 0 & 0 & 0 \\ 0 & 0 & 0 & 0 \\ 0 & 0 & 0 & 0 \\ 0 & 0 & 0 & 0 \\ 0 & 0 & 0 & 0 \\ 1 & 0 & 0 & 0 \\ 0 & 1 & 0 & 0 \\ 0 & 0 & 1 & 0 \\ 0 & 0 & 0 & 1 \end{bmatrix}}^{\mathbf{F_{btb}}} \overbrace{\begin{bmatrix} i^*_{d,1} - I_{d,1} \\ i^*_{q,1} - I_{q,1} \\ i^*_{q,2} - I_{q,2} \\ v^*_{dc} - V_{dc} \end{bmatrix}}^{\mathbf{v_{btb}}}. \end{aligned} \tag{4.21}$$

In addition to that, the output matrix can, once again, be written as an identity

matrix, meaning that all states can be measured, as it is depicted in Eq. (4.22).

$$\overbrace{\begin{bmatrix} y_{btb,1} \\ y_{btb,2} \\ y_{btb,3} \\ y_{btb,4} \\ y_{btb,5} \\ y_{btb,6} \\ y_{btb,7} \\ y_{btb,8} \\ y_{btb,9} \end{bmatrix}}^{\mathbf{y_{btb}}} = \overbrace{\begin{bmatrix} 1 & 0 & 0 & 0 & 0 & 0 & 0 & 0 & 0 \\ 0 & 1 & 0 & 0 & 0 & 0 & 0 & 0 & 0 \\ 0 & 0 & 1 & 0 & 0 & 0 & 0 & 0 & 0 \\ 0 & 0 & 0 & 1 & 0 & 0 & 0 & 0 & 0 \\ 0 & 0 & 0 & 0 & 1 & 0 & 0 & 0 & 0 \\ 0 & 0 & 0 & 0 & 0 & 1 & 0 & 0 & 0 \\ 0 & 0 & 0 & 0 & 0 & 0 & 1 & 0 & 0 \\ 0 & 0 & 0 & 0 & 0 & 0 & 0 & 1 & 0 \\ 0 & 0 & 0 & 0 & 0 & 0 & 0 & 0 & 1 \end{bmatrix}}^{\mathbf{C_{btb}}} \overbrace{\begin{bmatrix} \tilde{i}_{d,1} \\ \tilde{i}_{q,1} \\ \tilde{i}_{d,2} \\ \tilde{i}_{q,2} \\ \tilde{v}_{dc} \\ x_1 \\ x_2 \\ x_3 \\ x_4 \end{bmatrix}}^{\mathbf{x_{btb}}} \tag{4.22}$$

where the subscript **btb** is used to identify the set of matrices that is used for the BTB-VSC system presented in this subsection. Finally it is possible to write the system of equations shown in (4.23).

$$\begin{cases} \dot{\mathbf{x}}_{\mathbf{btb}} &= \mathbf{A_{btb}x_{btb}} + \mathbf{B_{btb}u_{btb}} + \mathbf{F_{btb}v_{btb}}, \\ \mathbf{y_{btb}} &= \mathbf{C_{btb}x_{btb}}. \end{cases} \tag{4.23}$$

## 4.3 LINEAR SYSTEM CONTROL

In the previous sections of this chapter, the basis to understand the criteria necessary for stability of a system was established. In this section, however, we study ways of controlling and stablizing systems. This section will be the cornerstone of the control design proposed in this very document.

### 4.3.1 **Observability and Controllability**

The concepts of observability and controllability are extremely important for linear multivariable control system design and, therefore, they can be found in almost every control engineering book (ÅSTRÖM; MURRAY, 2010; DERUSSO; CLOSE; ROY, 1990; ZHOU; DOYLE, 1998). Hence, there is no need to go in depth to each of these concepts but to merely describe it and show a way to verify if a system is observable and/or controllable. First, consider a linear system to be defined as

$$\begin{cases} \dot{\mathbf{x}}(t) = \mathbf{A}\mathbf{x}(t) + \mathbf{B}\mathbf{u}(t) + \mathbf{F}\mathbf{v}(t), \\ \mathbf{y}(t) = \mathbf{C}\mathbf{x}(t), \end{cases} \tag{4.24}$$

where $\mathbf{y}(t)$ is the $p \times 1$ output vector, $\mathbf{C}$ is the $p \times n$ output matrix, $\mathbf{v}(t)$ is the $l \times 1$ disturbance input, $\mathbf{F}$ is the $n \times l$ disturbance gain matrix and $\mathbf{x}(t)$, $\mathbf{u}(t)$, $\mathbf{A}$ and $\mathbf{B}$ are the vectors and matrices already discussed in Equation (2.42). For observability and controllability tests, the system is considered to have negligible disturbances and, therefore, the disturbance input and its associated gain matrix are ignored.

Let us start with observability. A system is said to observable when all of its modes, i.e. dynamical behavior that compose each state, are present in $\mathbf{y}(t)$. This means that the output vector is formed by a combination of the states and there is no state that is not represented in the ouput. Hence, no zero columns must be present in the output matrix $\mathbf{C}$ (DERUSSO; CLOSE; ROY, 1990) and in order to test if the pair ($\mathbf{C}$,$\mathbf{A}$) is observable, it is sufficient and necessary that

$$\mathcal{O} = \begin{bmatrix} \mathbf{C} \\ \mathbf{CA} \\ \mathbf{CA}^2 \\ \vdots \\ \mathbf{CA}^{n-1} \end{bmatrix} \tag{4.25}$$

is full-column rank (ZHOU; DOYLE, 1998). Otherwise, the pair ($\mathbf{C}$,$\mathbf{A}$) is said to be unobservable.

On the other hand, controllability is related to the impact that inputs have on state variables. Loosely, a dynamical system is said to be controllable if, for any state variable with specified initial and final conditions, there exists an input signal that can drive the state from its initial value to its determined final value using a finite and specified amount of time (ZHOU; DOYLE, 1998). It means that the influence the input vector has on state variables does not vanish with time. Hence, controllability is a way of determining the coupling between inputs and states or, even more specifically, the modes of the system (DERUSSO; CLOSE; ROY, 1990). The input matrix $\mathbf{B}$, then, cannot have zero rows in order the system to be considered controllable. In addition, to be sure that the pair ($\mathbf{A}$,$\mathbf{B}$) is controllable, it is sufficient and necessary that

$$\mathcal{C} = \begin{bmatrix} \mathbf{B} & \mathbf{AB} & \mathbf{A}^2\mathbf{B} & \cdots & \mathbf{A}^{n-1}\mathbf{B} \end{bmatrix} \tag{4.26}$$

is full-row rank (ZHOU; DOYLE, 1998). Otherwise, the pair ($\mathbf{A}$,$\mathbf{B}$) is said to be uncontrollable.

### 4.3.2 **Full-State Feedback Control**

The main control strategy that is used in this study is the full-state feedback. This type of controller uses all the state variables in the feedback loop and it can be really

valuable in systems where all the states need to be measured for other reasons, such as protection. In these situations, there would not be any additional efforts in adding new measurement units and the full-state feedback controller could be rather useful. In this control strategy, the input signal is defined as

$$\mathbf{u}(t) = \mathbf{K}\mathbf{x}(t), \tag{4.27}$$

where $\mathbf{K}$ is the $r \times n$ control gain matrix. Now, if we replace equation (4.27) in the first equation of (4.24) we have that

$$\dot{\mathbf{x}}(t) = \mathbf{A}\mathbf{x}(t) + \mathbf{B}\mathbf{K}\mathbf{x}(t) + \mathbf{F}\mathbf{v}(t), \tag{4.28}$$

which can be further simplified into the following closed-loop system representation

$$\dot{\mathbf{x}}(t) = \overbrace{[\mathbf{A} + \mathbf{B}\mathbf{K}]}^{\mathbf{A_{CL}}}\mathbf{x}(t) + \mathbf{F}\mathbf{v}(t). \tag{4.29}$$

where the subscript **CL** stands closed-loop. This means that the dynamics of the closed loop system is determined by the eigenvalues of $\mathbf{A_{CL}}$. In addition, if the pair (**A**,**B**) is completely controllable, then **K** can be found such that all eigenvalues of $\mathbf{A_{CL}}$ can be arbitrarily placed in the complex plane (DERUSSO; CLOSE; ROY, 1990). By finding an appropriate controll gain matrix **K** it is possible to drive the system to be asymptotically stable and to behave dynamically according to some specifications that are previously set. It is also worth mentioning that while the full-state feedback strategy does not alter controllability, it can destroy observability of a system (DERUSSO; CLOSE; ROY, 1990) because the observability pair to be tested would change to ($\mathbf{C}$,$\mathbf{A_{CL}}$).

### 4.3.3 **Linear Quadratic Regulators**

This optimal control strategy is well-known and it concerns finding an input $\mathbf{u}$(t) that can drive the state vector $\mathbf{x}$(t) to a small neighborhood of the origin (i.e. equilibrium point) at some time instant (ZHOU; DOYLE, 1998). In addition to that, practical systems do not have infinite amount of energy to spend on control actions. Therefore, it is also necessary to minimize the energy spent on driving the system to equilibrium (ZHOU; DOYLE, 1998). In addition to that, some performance requirements on the states might also be desired.

The Linear Quadratic Regulator (LQR) problem, then, becomes to find input $\mathbf{u}(t)$ that minimizes the function

$$J = \int_0^\infty \begin{bmatrix} \mathbf{x}(t) \\ \mathbf{u}(t) \end{bmatrix}^\intercal \begin{bmatrix} \mathbf{Q} & \mathbf{0} \\ \mathbf{0} & \mathbf{R} \end{bmatrix} \begin{bmatrix} \mathbf{x}(t) \\ \mathbf{u}(t) \end{bmatrix} dt, \tag{4.30}$$

where the weight matrix for state variables $\mathbf{Q}$ is positive semi-definite and the weight matrix for manipulated variables $\mathbf{R}$ is positive definite matrices (ZHOU; DOYLE, 1998; SONTAG, 2013; RODRÍGUEZ-CABERO; SÁNCHEZ; PRODANOVIC, 2016; ANDERSON; MOORE, 2007). Note that equation (4.30) can be re-written to become

$$J = \int_0^\infty \left(\mathbf{x}^\intercal \mathbf{Q}\mathbf{x} + \mathbf{u}^\intercal \mathbf{R}\mathbf{u}\right) dt. \tag{4.31}$$

Note that if the state vector is driven to equilibrium, then the first term inside the integral, $\mathbf{x}^\intercal\mathbf{Q}\mathbf{x}$, would vanish, making $J$ to be finite-valued. In addition to that, note that minimizing the second term inside the integral is to minimize the energy spent on the control action trhoughout the process of driving the state vector to the equilibrium. In addition, note that if we use a full-state feedback law and ignore the terms related to the reference, we would end up minimizing the following function:

$$\begin{aligned} J &= \int_0^\infty \left[\mathbf{x}^\intercal \mathbf{Q}\mathbf{x} + (\mathbf{K}\mathbf{x})^\intercal \mathbf{R}\mathbf{K}\mathbf{x}\right] dt, \\ J &= \int_0^\infty \left(\mathbf{x}^\intercal \mathbf{Q}\mathbf{x} + \mathbf{x}^\intercal \mathbf{K}^\intercal \mathbf{R}\mathbf{K}\mathbf{x}\right) dt, \\ J &= \int_0^\infty \mathbf{x}^\intercal \left(\mathbf{Q} + \mathbf{K}^\intercal \mathbf{R}\mathbf{K}\right) \mathbf{x}\ dt. \end{aligned} \tag{4.32}$$

It is important to observe that the problem of finding the input vector $\mathbf{u}(t)$ was now replaced by finding the control gain matrix $\mathbf{K}$. This gain matrix can be tuned by adopting different values to matrices $\mathbf{Q}$ and $\mathbf{R}$. These matrices can be determined in such way that the closed loop control system performs as desired. The entire problem is, then, narrowed to finding $\mathbf{K}$ that stabilizes the closed loop state matrix $\mathbf{A_{CL}}$ and minimizes

$$\min_{\mathbf{K}} \quad \int_0^\infty \mathbf{x}^\intercal \left(\mathbf{Q} + \mathbf{K}^\intercal \mathbf{R}\mathbf{K}\right) \mathbf{x}\ dt. \tag{4.33}$$

If the linear system described by the pair ($\mathbf{A}$,$\mathbf{B}$) is controllable, then it is guaranteed that a gain matrix $\mathbf{K}$ exists such that the constrains listed above are satisfied (ANDERSON; MOORE, 2007).

### 4.3.4 **Robust Pole Placement**

Strategies concerning pole placement are rather common in linear systems. However, the strategy here discussed makes usage of Linear Matrices Inequalities or LMI (DUAN;

YU, 2013). For example, the matrix inequality regarding the stability of a linear system, presented in Equation (2.57), is an LMI. This is because given $\mathbf{A}$, we want to find a positive-definite $\mathbf{P}$ such that

$$\mathbf{A}^\intercal\mathbf{P} + \mathbf{P}\mathbf{A} \prec 0, \tag{4.34}$$

or, in other words, we want to find $\mathbf{P}$ such that, for every $\mathbf{x} \neq \mathbf{0}$, we have that

$$\mathbf{x}^\intercal \left(\mathbf{A}^\intercal\mathbf{P} + \mathbf{P}\mathbf{A}\right) \mathbf{x} \prec 0. \tag{4.35}$$

In fact, consider that a full-state feedback control strategy is applied and disconsider the terms related to the references. If that is case, we have that

$$\mathbf{A_{CL}} = \mathbf{A} + \mathbf{B}\mathbf{K}, \tag{4.36}$$

as we have already described previously. Hence, to guarantee that $\mathbf{A_{CL}}$ is stable, we would neet it to be Hurwitz. As it is stated in (2.57), we then need to find a positive-definite $\mathbf{P}$ such that

$$\mathbf{A}_{\mathbf{CL}}^\intercal\mathbf{P} + \mathbf{P}\mathbf{A_{CL}} \prec 0. \tag{4.37}$$

If we replace (4.36) in (4.37) we would have that

$$\begin{aligned} \left(\mathbf{A} + \mathbf{B}\mathbf{K}\right)^\intercal \mathbf{P} + \mathbf{P}\left(\mathbf{A} + \mathbf{B}\mathbf{K}\right) &\prec 0, \\ \mathbf{A}^\intercal\mathbf{P} + \mathbf{P}\mathbf{A} + \mathbf{K}^\intercal\mathbf{B}^\intercal\mathbf{P} + \mathbf{P}\mathbf{B}\mathbf{K} &\prec 0. \end{aligned} \tag{4.38}$$

At this point it is important to highlight two interesting properties. One is that, if you multiply one LMI by a positive-definite matrix, then the relation expressed in the LMI will remain unchanged (LIU; YAO, 2016). The second property is that if $\mathbf{P}$ is a positive-definite matrix, then its inverse $\mathbf{P}^{-1}$ is also positive-definite (LIU; YAO, 2016). Therefore, if we multiply Equation (4.38) by $\mathbf{P}^{-1}$ on the left and on the right, we would end up with

$$\begin{aligned} \mathbf{P}^{-1}\mathbf{A}^\intercal\mathbf{P}\mathbf{P}^{-1} + \mathbf{P}^{-1}\mathbf{P}\mathbf{A}\mathbf{P}^{-1} + \mathbf{P}^{-1}\mathbf{K}^\intercal\mathbf{B}^\intercal\mathbf{P}\mathbf{P}^{-1} + \mathbf{P}^{-1}\mathbf{P}\mathbf{B}\mathbf{K}\mathbf{P}^{-1} &\prec 0, \\ \mathbf{P}^{-1}\mathbf{A}^\intercal + \mathbf{A}\mathbf{P}^{-1} + \mathbf{P}^{-1}\mathbf{K}^\intercal\mathbf{B}^\intercal + \mathbf{B}\mathbf{K}\mathbf{P}^{-1} &\prec 0. \end{aligned} \tag{4.39}$$

Equation (4.39) is said to be a bilinear matrix inequality, because it has the multiplication of two matrices that are actually unknowns of our problem (LIU; YAO, 2016). Therefore, in order to solve this issue, it is possible to make a variable change. We can, for example, make that $\mathbf{W} = \mathbf{K}\mathbf{P}^{-1}$. In addition, let us use $\mathbf{P_I} = \mathbf{P}^{-1}$ to avoid representing the inverse at all times. Therefore, (4.39) can be rewritten as the LMI below.

$$\mathbf{P_I}\mathbf{A}^\intercal + \mathbf{A}\mathbf{P_I} + \mathbf{W}^\intercal\mathbf{B}^\intercal + \mathbf{B}\mathbf{W} \prec 0. \tag{4.40}$$

Hence, to solve this problem we need to find matrices $\mathbf{P}$, positive definite, and $\mathbf{W}$, which satisfy the LMI in (4.40), making the closed loop system asymptotically stable. However, sometimes, it is desirable that the stable system shows a dynamic performance according to some predetermined specifications. This is the main principle behind pole-placement techniques(DERUSSO; CLOSE; ROY, 1990), where the eigenvalues are chosen based on the specifications and then matrix $\mathbf{K}$ is calculated based on the predetermined eigenvalues.

However, in the present study, we want to determine a region in the complex plane where the closed loop eigenvalues can be located. This type of state feedback control is, therefore, concerned with finding a gain matrix $\mathbf{K}$ which guarantees that all poles are located inside a region in complex plane, say $\mathcal{S}$, while there exists positive definite matrix $\mathbf{P}$ that satisfies the LMI in (4.40) (LIU; YAO, 2016). The solution can be found by assembling a system of LMIs that must be solved simultaneously using an optimization procedure (DUAN; YU, 2013; DULLERUD; PAGANINI, 2013). Consider a convex region $\mathcal{S}$ in the complex plane in which all closed loop eigenvalues must be located. A typical region $\mathcal{S}$ is represented in Figure 24. The convexity of the region is necessary in order to guarantee that the system of LMIs can be solved using convex optimization techniques (DUAN; YU, 2013). As one can see, the region is completely defined by three parameters: $\alpha$, $\theta$ and $\rho$. Variable $\alpha$ is related to the real part of the smallest eigenvalue allowed or the eigenvalue most closely located to the imaginary axis. This parameter is strictly related to the smallest setling time $t_s$ allowed for the system (ÅSTRÖM; MURRAY, 2010). The settling time $t_s$ indicates how much time is needed in order for the system to achieve its steady state value after a disturbance. Variable $\theta$ on the other hand is closely related to the minimum damping coefficient allowed for this system. In fact, the damping ratio, which is commonly used in the analysis of linear systems using the frequency domain, and the angle $\theta$ are related through $\xi = \cos\theta$ (ÅSTRÖM; MURRAY, 2010). Therefore, $\theta$ is associated with the time needed for an oscillation caused by a disturbance to vanish from the dynamic response of the system. The larger the damping, the faster a sinusoidal oscillation vanishes. Finally, parameter $\rho$ is related to the largest eigenvalue allowed in the system. This value is usually used to limit how fast a system can respond to some disturbance and, in addition, it can be use to filter fast dynamics coming from measurement

systems or the original system. Limiting the maximum size of an eigenvalue is necessary in order to provide robustness to the practical implementation of the control system.

Figure 24 – Convex $\mathcal{S}$ region and its parameters $\alpha$, $\rho$ e $\theta$.

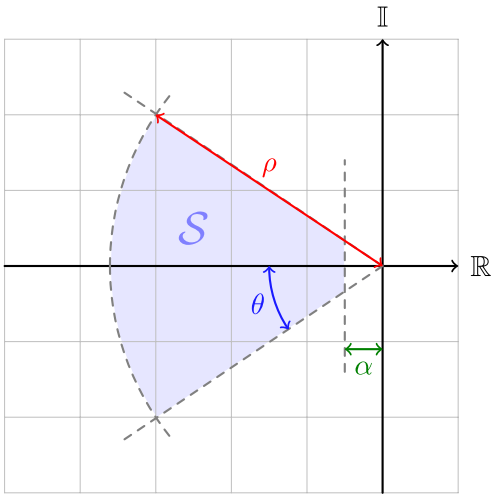


Source: Author (2022).

In order to place all the closed loop eigenvalues inside a region characterized by parameters $\alpha$, $\rho$ and $\theta$, one must solve the set of linear matrix inequalites shown in (4.41) (DUAN; YU, 2013). By finding the appropriate matrices $\mathbf{P_I}$ and $\mathbf{W}$, one can easily calculate the gain matrix $\mathbf{K} = \mathbf{WP}$ needed for the full-state feedback control system design.

$$
\begin{aligned}
&2\alpha\mathbf{P_I} + \mathbf{AP_I} + \mathbf{P_I}\mathbf{A}^\intercal + \mathbf{BW} + \mathbf{W}^\intercal\mathbf{B}^\intercal \prec 0,\\
&\begin{bmatrix} -\rho\mathbf{P_I} & \mathbf{AP_I} + \mathbf{BW} \\ \mathbf{P_I}\mathbf{A}^\intercal + \mathbf{W}^\intercal\mathbf{B}^\intercal + & -\rho\mathbf{P_I} \end{bmatrix} \prec 0,\\
&\begin{bmatrix} (\mathbf{AP_I} + \mathbf{P_I}\mathbf{A}^\intercal + \mathbf{BW} + \mathbf{W}^\intercal\mathbf{B}^\intercal)\sin\theta & (\mathbf{AP_I} - \mathbf{P_I}\mathbf{A}^\intercal + \mathbf{BW} - \mathbf{W}^\intercal\mathbf{B}^\intercal)\cos\theta \\ (-\mathbf{AP_I} + \mathbf{P_I}\mathbf{A}^\intercal - \mathbf{BW} + \mathbf{W}^\intercal\mathbf{B}^\intercal)\cos\theta & (\mathbf{AP_I} + \mathbf{P_I}\mathbf{A}^\intercal + \mathbf{BW} + \mathbf{W}^\intercal\mathbf{B}^\intercal)\sin\theta \end{bmatrix} \prec 0.
\end{aligned}
\tag{4.41}
$$

# 5 STUDIED TEST SYSTEMS AND CONTROLLER DESIGN

In this chapter, the two studied test systems have their simulation diagrams presented together with parameters values used during implementation. These values are also used to tune the different controllers. Besides that, this section also shows how the simulation experiment is set-up on a digital environment and how the controller action might be implemented. It is also important to recall that each of the test systems undergoes a different type of simulation, depending on the stated objectives for the experiment.

## 5.1 SINGLE VSC SYSTEM

Consider the VSC interfacing an AC and a DC systems, as depicted in Figure 16 and recall the linear dynamic representation shown in equation (4.13). These are the references for structuring the experiments that are conducted with the single VSC system.

### 5.1.1 **Experiment Description**

In this set of experiments, both control strategies, the LQR and the robust pole placement, are designed and tested in the same system while it undergoes changes in the power profile. The VSC interfaces an AC grid and a DC bus, which changes its power demand. In the first moment, there is no power exchange between the DC and the AC system and therefore $P_{in}^{init} = 0$, but later the power injected by the DC side into the AC grid increases until it reaches $P_{in}^{max}$. After that, the DC side changes its power profile, consuming $-P_{in}^{min}$ from the AC terminal. Therefore, it is possible to say that the VSC converter tested in this experiment and its control system should be able to deal with a bidirectional power-flow between the DC bus and the AC grid. The values of power adopted for the experiment are displayed in Table 1.

Table 1 – Input power values for the single VSC test system.

| Description | Value |
|---|---|
| Initial DC bus input power ($P_{in}^{init}$) | 0 $W$ |
| Maximum DC bus input power ($P_{in}^{max}$) | 30 $kW$ |
| Minimum DC bus input power ($P_{in}^{min}$) | -30 $kW$ |

Source: Author (2022).

### 5.1.2 **System Description and Parameters**

The diagram representing the single VSC system that is tested in this study is depicted in Figure 25. The dashed lines correspond to control and measurement signals that are used in the different devices that compose the test system and electrical connections

are represented with a solid dark line. Note that, in this test system, the grid is considered to be an ideal voltage source and, therefore, there is no RL branch between the point of common coupling and the actual grid. The effect of a non-ideal grid is considered in the BTB test system.

Figure 25 – Single VSC test system diagram.

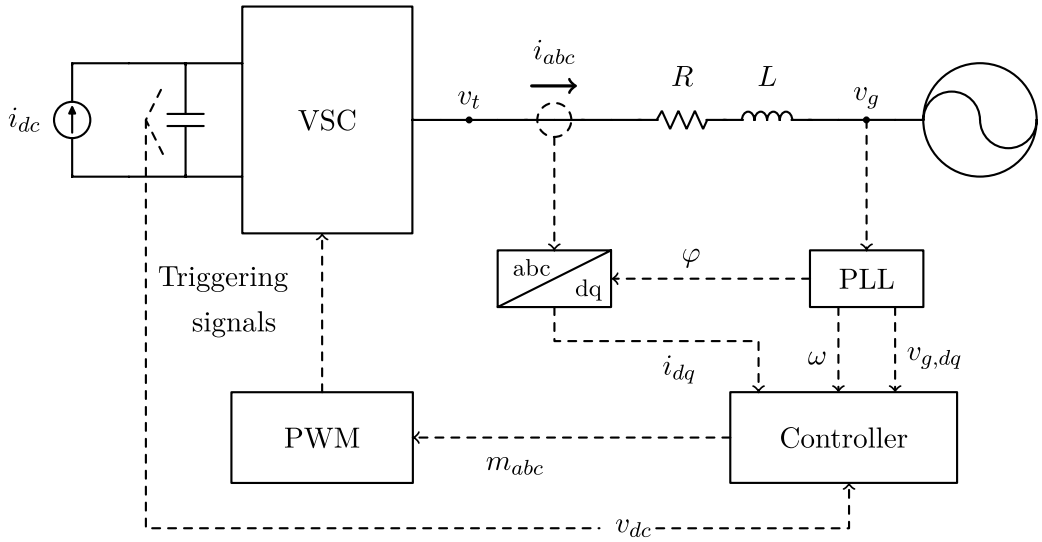


Source: Author (2022).

The system depicted in Figure 25 has its parameters listed on Table 2. These values are extremely important for the numerical calculation of the linear system, needed for designing both control strategies analyzed in this experiment.

Table 2 – Single VSC System Parameters.

| Description | Value & Unit |
|---|---|
| RMS Line Voltage at PCC ($v_{g,rms}$) | 220 $V$ |
| Peak Phase-to-Ground Voltage at PCC ($\hat{V}_g$) | 180 $V$ |
| Grid Frequency ($f$) | 60 $Hz$ |
| Grid Angular Frequency ($\omega$) | 376.99 $rad/s$ |
| DC Bus Capacitance ($C_{dc}$) | 2 $mF$ |
| Capacitor Parallel Resistance ($r_c$) | 1 $k\Omega$ |
| DC Bus Voltage ($V_{dc}$) | 400 $V$ |
| Line Equivalent Inductance ($L$) | 2 $mH$ |
| Line Equivalent Resistance ($R$) | 75,4 $m\Omega$ |
| Switching Frequency ($f_s$) | 20 $kHz$ |

Source: Author (2022).

The PLL system represented in Figure 25 is the same one described in Section 3.6. There, it is stated that, for the SRF-based PLL controller, a good performance is achieved with $\xi = 0.7$ and $\omega_n = 100$ radians per second. By replacing these values, and the value of $\hat{V}_g$ from Table 2, on equation (3.128) it is possible to obtain the values displayed in Table

3. In addition, both SOGI filters used in the PLL have $\omega_r$ and $k$ fixed at the values shown also in Table 3.

Table 3 – Phase-Locked Loop system parameters.

| Description | Value |
|---|---|
| Proportional Gain from SRF's controller ($K_{pi}$) | 0.7788 $\frac{rad}{s \cdot V}$ |
| Integral Time Constant from SRF's controller ($T_{pi}$) | 0.0140 $s$ |
| SOGI's band-pass frequency ($\omega_r$) | 377 $rad/s$ |
| SOGI's gain ($k$) | 1.4142 $V/V$ |

Source: Author (2022).

Note that, because the DC bus voltage is expected to be maintained under a constant value during the entire simulation, the current $I_{dc}$ can be calculated from the power value as

$$I_{dc} = \frac{P_{in}}{V_{dc}}, \tag{5.1}$$

where $P_{in}$ can be $P_{in}^{min}$, $P_{in}^{max}$ or $P_{in}^{init}$. Hence, by using the value of $V_{dc}$ from Table 2 it is possible to use equation (5.1) for calculating the maximum and minimum values of $i_{dc}$ that the converter should be able to deal. Those values are summarized in Table 4.

Table 4 – Input DC current values for the single VSC test system.

| Description | Value |
|---|---|
| Initial input DC current ($I_{dc}^{init}$) | 0 $A$ |
| Maximum nput DC current ($I_{dc}^{max}$) | 75 $A$ |
| Minimum input DC current ($I_{dc}^{min}$) | -75 $A$ |

Source: Author (2022).

### 5.1.3 **Control Design**

Now that the system's parameters are presented the control design process can be performed by using the theory stated in previous chapters but especially in Section 4.3. The process to calculate the state feedback matrix for the LQR and the Robust Pole Placement strategies is shown in this Subsection.

#### 5.1.3.1 *LQR*

The first task in designing an LQR for the studied test system is to find a steady state operation point in which the system is going to be linearized. The task however is not trivial since the experiment involves bidirectional power flow and, therefore, a change in operation point during the simulation, leading to a change in the linear system being

considered for control design. Hence, it is necessary to pick a point that should be within the input power range stated on Table 1 and its corresponding DC bus current range, shown in Table 4. Because there is no definitive rule to chose such value, suppose a design where $P_{in} = 20kW$ is chosen. By using equation (5.1), it is possible to find the corresponding value for $I_{dc}$. In addition to that, because the PLL is considered to be effective the value of $V_{g,d}$ is expected to be equal to $\hat{V}_g$, while the value of $V_{g,q}$ is expected to be 0 due to the appropriate tracking. Finally, the quadrature current reference $\bar{i}_q^*$ is set to zero and, therefore, the corresponding steady state value of that variable is also expected to be zero. These pieces of information are summarized in Table 5.

Table 5 – Equilibrium conditions for LQR design.

| Description | Value |
|---|---|
| Input Power ($P_{in}$) | 20 $kW$ |
| Input Current ($I_{dc}$) | 50 $A$ |
| Tracked Voltage Value on Direct Axis at the PCC ($V_{g,d}$) | 180 $V$ |
| Tracked Voltage Value on Quadrature Axis at the PCC ($V_{g,q}$) | 0 $V$ |
| Quadrature Axis Current ($I_q$) | 0 $A$ |

Source: Author (2022).

It is possible to use the values listed on Tables 2 and 5 on equations (4.4) for determining additional initial conditions needed for obtaining a linear system. These variables are listed in Table 6.

Table 6 – Calculated steady state variables for LQR design.

| Description | Value |
|---|---|
| Direct Axis Modulation Index ($M_d$) | 0.927109351546722 $V$ |
| Direct Axis Current ($I_d$) | 71.908094288386636 $A$ |
| Quadrature Axis Modulation Index ($M_q$) | 0.271087128900045 $V$ |

Source: Author (2022).

The information listed in Tables 2, 5 and 6 can be used to calculate the matrices from equation (4.11). The result is shown in equation (5.2), where the subscript **L** on matrices stands for LQR. Note that $\bar{v}_{dc}^*$ is kept constant and equal to 400 V, while $\bar{i}_q^*$ is

kept to be 0 A.

$$\frac{d}{dt}\begin{bmatrix}\tilde{i}_d\\ \tilde{i}_q\\ \tilde{v}_{dc}\\ x_1\\ x_2\end{bmatrix} = \overbrace{\begin{bmatrix}-37.7000 & 376.9911 & 231.7773 & 0 & 0\\ -376.9911 & -37.7000 & 67.7718 & 0 & 0\\ -347.6660 & -101.6577 & 0 & 0 & 0\\ 0 & -1 & 0 & 0 & 0\\ 0 & 0 & -1 & 0 & 0\end{bmatrix}}^{\mathbf{A_{vsc,L}}}\overbrace{\begin{bmatrix}\tilde{i}_d\\ \tilde{i}_q\\ \tilde{v}_{dc}\\ x_1\\ x_2\end{bmatrix}}^{\mathbf{x_{vsc}}} + \overbrace{\begin{bmatrix}10^5 & 0\\ 0 & 10^5\\ -26970 & 0\\ 0 & 0\\ 0 & 0\end{bmatrix}}^{\mathbf{B_{vsc,L}}}\overbrace{\begin{bmatrix}\tilde{u}_d\\ \tilde{u}_q\end{bmatrix}}^{\mathbf{u_{vsc}}} + \overbrace{\begin{bmatrix}0 & 0 & 0\\ 0 & 0 & 0\\ 0 & 0 & 500\\ 1 & 0 & 0\\ 0 & 1 & 0\end{bmatrix}}^{\mathbf{F_{vsc}}}\overbrace{\begin{bmatrix}\bar{i}_q^*\\ \bar{v}_{dc}^* - 400\\ \tilde{i}_{dc}\end{bmatrix}}^{\mathbf{v_{vsc}}}. \tag{5.2}$$

Matrices $\mathbf{A_{vsc,L}}$ and $\mathbf{B_{vsc,L}}$ can be combined for assembling controllability matrix $\mathcal{C}_{vsc,L}$. When assessing its rank using Matlab, it is possible to check that $\mathcal{C}_{vsc,L}$ is full rank, meaning the pair ($\mathbf{A_{vsc,L}}$,$\mathbf{B_{vsc,L}}$) is fully controllable and it is possible to find a matrix $\mathbf{K_{vsc,L}}$ using the LQR strategy. As it is shown in equation (4.33), it is necessary to have matrices $\mathbf{Q}$ and $\mathbf{R}$ for designing an LQR-based controller. These are weight matrices and their values is shown in equations (5.3) and (5.4).

$$\mathbf{Q} = \begin{bmatrix}1 & 0 & 0 & 0 & 0\\ 0 & 1 & 0 & 0 & 0\\ 0 & 0 & 1 & 0 & 0\\ 0 & 0 & 0 & 10^6 & 0\\ 0 & 0 & 0 & 0 & 10^5\end{bmatrix}. \tag{5.3}$$

$$\mathbf{R} = \begin{bmatrix}100 & 0\\ 0 & 100\end{bmatrix}. \tag{5.4}$$

Matrix $\mathbf{K_{vsc,L}}$ is then calculated using function `lqr` from Matlab, which has matrices $\mathbf{A_{vsc,L}}$, $\mathbf{B_{vsc,L}}$, $\mathbf{Q}$ and $\mathbf{R}$ as inputs, in that order. The result, which has been multiplied by minus one for coherence with the mathematical representation adopted in this study, is shown in Equation (5.5).

$$\mathbf{K_{vsc,L}} = \begin{bmatrix}-0.0660 & 0.0002 & 0.1592 & -3.5230 & -31.6031\\ 0.0015 & -0.1092 & 0.0050 & 99.9379 & -1.1141\end{bmatrix}. \tag{5.5}$$

#### 5.1.3.2 *Robust Pole Placement*

This LMI-based strategy can take into consideration a range of operation conditions instead of using only one point as it was shown in the LQR design. This is done by using the maximum and minimum values of $P_{in}$ from Table 1 for creating two sets of LMIs that will be solved simultaneously. For that purpose, two sets of linear systems must be calculated; one for $P_{in}^{max}$ and, consequently, to $I_{dc}^{max}$, and another one for $P_{in}^{min}$ and $I_{dc}^{min}$. However, both calculations will take into consideration the parameters that are listed in Table 7

Table 7 – Equilibrium conditions for robust controller design.

| Description | Value |
|---|---|
| Tracked Voltage Value on Direct Axis at the PCC ($V_{g,d}$) | 180 $V$ |
| Tracked Voltage Value on Quadrature Axis at the PCC ($V_{g,q}$) | 0 $V$ |
| Quadrature Axis Current ($I_q$) | 0 $A$ |

Source: Author (2022).

For the condition where $P_{in} = P_{in}^{min}$ and, therefore, $I_{dc} = I_{dc}^{min}$, it is possible to calculate the variables from Eq. (4.4). The results are shown on Table 8. The subscript $_1$ is going to be used as a reference for this condition.

Table 8 – Calculated steady state variables for minimum power in robust controller design.

| Description | Value |
|---|---|
| Direct Axis Modulation Index ($M_{d,min}$) | 0.855955662603689 $V$ |
| Direct Axis Current ($I_{d,min}$) | -116.8284811573242 $A$ |
| Quadrature Axis Modulation Index ($M_{q,min}$) | -0.440432997760684 $V$ |

Source: Author (2022).

Now the information listed in Tables 2 and 8 can be used to calculate the matrices from equation (4.11). The result is shown in equation (5.6), where the subscript **R** on matrices was added as a reference to robust pole placement. Note once again that that $\bar{v}_{dc}^{*}$

and $\bar{i}_q^*$ are kept constant and equal to 400 V and 0 A, respectively.

$$\frac{d}{dt}\begin{bmatrix} \tilde{i}_d \\ \tilde{i}_q \\ \tilde{v}_{dc} \\ x_1 \\ x_2 \end{bmatrix} = \overbrace{\begin{bmatrix} -37.7000 & 376.9911 & 213.9889 & 0 & 0 \\ -376.9911 & -37.7000 & -110.1082 & 0 & 0 \\ -320.9834 & 165.1624 & 0 & 0 & 0 \\ 0 & -1 & 0 & 0 & 0 \\ 0 & 0 & -1 & 0 & 0 \end{bmatrix}}^{\mathbf{A_{vsc,R,1}}} \overbrace{\begin{bmatrix} \tilde{i}_d \\ \tilde{i}_q \\ \tilde{v}_{dc} \\ x_1 \\ x_2 \end{bmatrix}}^{\mathbf{x_{vsc}}} + \overbrace{\begin{bmatrix} 10^5 & 0 \\ 0 & 10^5 \\ 43810 & 0 \\ 0 & 0 \\ 0 & 0 \end{bmatrix}}^{\mathbf{B_{vsc,R,1}}} \overbrace{\begin{bmatrix} \tilde{u}_d \\ \tilde{u}_q \end{bmatrix}}^{\mathbf{u_{vsc}}} + \overbrace{\begin{bmatrix} 0 & 0 & 0 \\ 0 & 0 & 0 \\ 0 & 0 & 500 \\ 1 & 0 & 0 \\ 0 & 1 & 0 \end{bmatrix}}^{\mathbf{F_{vsc}}} \overbrace{\begin{bmatrix} \bar{i}_q^* \\ \bar{v}_{dc}^* - 400 \\ \tilde{i}_{dc} \end{bmatrix}}^{\mathbf{v_{vsc}}}. \tag{5.6}$$

For the condition where $P_{in} = P_{in}^{max}$ and $I_{dc} = I_{dc}^{max}$, the results are shown on Table 9. The subscript $_2$ is going to be used as a reference for this condition.

Table 9 – Calculated steady state variables for maximum power in robust controller design.

| Description | Value |
|---|---|
| Direct Axis Modulation Index ($M_{d,max}$) | 0.940102030193714 $V$ |
| Direct Axis Current ($I_{d,max}$) | 106.3714328745725 $A$ |
| Quadrature Axis Modulation Index ($M_{q,max}$) | 0.401010854484692 $V$ |

Source: Author (2022).

$$\frac{d}{dt}\begin{bmatrix} \tilde{i}_d \\ \tilde{i}_q \\ \tilde{v}_{dc} \\ x_1 \\ x_2 \end{bmatrix} = \overbrace{\begin{bmatrix} -37.7000 & 376.9911 & 235.0255 & 0 & 0 \\ -376.9911 & -37.7000 & 100.2527 & 0 & 0 \\ -352.5383 & -150.3791 & 0 & 0 & 0 \\ 0 & -1 & 0 & 0 & 0 \\ 0 & 0 & -1 & 0 & 0 \end{bmatrix}}^{\mathbf{A_{vsc,R,2}}} \overbrace{\begin{bmatrix} \tilde{i}_d \\ \tilde{i}_q \\ \tilde{v}_{dc} \\ x_1 \\ x_2 \end{bmatrix}}^{\mathbf{x_{vsc}}} + \overbrace{\begin{bmatrix} 10^5 & 0 \\ 0 & 10^5 \\ -39890 & 0 \\ 0 & 0 \\ 0 & 0 \end{bmatrix}}^{\mathbf{B_{vsc,R,2}}} \overbrace{\begin{bmatrix} \tilde{u}_d \\ \tilde{u}_q \end{bmatrix}}^{\mathbf{u_{vsc}}} + \overbrace{\begin{bmatrix} 0 & 0 & 0 \\ 0 & 0 & 0 \\ 0 & 0 & 500 \\ 1 & 0 & 0 \\ 0 & 1 & 0 \end{bmatrix}}^{\mathbf{F_{vsc}}} \overbrace{\begin{bmatrix} \bar{i}_q^* \\ \bar{v}_{dc}^* - 400 \\ \tilde{i}_{dc} \end{bmatrix}}^{\mathbf{v_{vsc}}}. \tag{5.7}$$

The pair $\mathbf{A_{vsc,R,1}}$ and $\mathbf{B_{vsc,R,1}}$, and the pair $\mathbf{A_{vsc,R,2}}$ and $\mathbf{B_{vsc,R,2}}$ can be used for calculating controllability matrices $\mathcal{C}_{vsc,1}$ and $\mathcal{C}_{vsc,2}$, respectively. By using Matlab for assessing their ranks, it is possible to find that both are full rank, meaning that both pairs are fully controllable and that one single matrix $\mathbf{K_{vsc,R}}$ can be found. For that purpose, it is first necessary to determine the area $\mathcal{S}$ that will contain the poles for all the operation points within the desired power range. The values for the parameters that define area $\mathcal{S}$ are listed in Table 10.

Table 10 – Pole placement region information for controller design.

| Description | Value |
|---|---|
| Minimum attenuation ($\alpha_{vsc}$) | 129 $s^{-1}$ |
| Minimum damping ($\theta_{vsc}$) | 45 ° |
| Maximum radius ($\rho_{vsc}$) | 12566.37 $s^{-1}$ |

Source: Author (2022).

Using the parameters listed in Table 10 and matrices $\mathbf{A_{vsc,R,1}}$, $\mathbf{B_{vsc,R,1}}$, $\mathbf{A_{vsc,R,2}}$ and $\mathbf{B_{vsc,R,2}}$, it is possible to write the following set of LMIs

$$
\begin{aligned}
&2\alpha_{vsc}\mathbf{P_I} + \mathbf{A_{vsc,R,1}}\mathbf{P_I} + \mathbf{P_I}\mathbf{A_{vsc,R,1}}^{\intercal} + \mathbf{B_{vsc,R,1}}\mathbf{W} + \mathbf{W}^{\intercal}\mathbf{B_{vsc,R,1}}^{\intercal} \prec 0,\\
&2\alpha_{vsc}\mathbf{P_I} + \mathbf{A_{vsc,R,2}}\mathbf{P_I} + \mathbf{P_I}\mathbf{A_{vsc,R,2}}^{\intercal} + \mathbf{B_{vsc,R,2}}\mathbf{W} + \mathbf{W}^{\intercal}\mathbf{B_{vsc,R,2}}^{\intercal} \prec 0,\\
&\begin{bmatrix} -\rho_{vsc}\mathbf{P_I} & \mathbf{A_{vsc,R,1}}\mathbf{P_I} + \mathbf{B_{vsc,R,1}}\mathbf{W} \\ \mathbf{P_I}\mathbf{A_{vsc,R,1}}^{\intercal} + \mathbf{W}^{\intercal}\mathbf{B_{vsc,R,1}}^{\intercal} + & -\rho_{vsc}\mathbf{P_I} \end{bmatrix} \prec 0,\\
&\begin{bmatrix} -\rho_{vsc}\mathbf{P_I} & \mathbf{A_{vsc,R,2}}\mathbf{P_I} + \mathbf{B_{vsc,R,2}}\mathbf{W} \\ \mathbf{P_I}\mathbf{A_{vsc,R,2}}^{\intercal} + \mathbf{W}^{\intercal}\mathbf{B_{vsc,R,2}}^{\intercal} + & -\rho_{vsc}\mathbf{P_I} \end{bmatrix} \prec 0,\\
&\begin{bmatrix} \mathbf{M_{vsc,1}}\sin\theta_{vsc} & \mathbf{L_{vsc,1}}\cos\theta_{vsc} \\ \mathbf{N_{vsc,1}}\cos\theta_{vsc} & \mathbf{M_{vsc,1}}\sin\theta_{vsc} \end{bmatrix} \prec 0,\\
&\begin{bmatrix} \mathbf{M_{vsc,2}}\sin\theta_{vsc} & \mathbf{L_{vsc,2}}\cos\theta_{vsc} \\ \mathbf{N_{vsc,2}}\cos\theta_{vsc} & \mathbf{M_{vsc,2}}\sin\theta_{vsc} \end{bmatrix} \prec 0,
\end{aligned}
\tag{5.8}
$$

where

$$
\begin{aligned}
\mathbf{M_{vsc,1}} &= \mathbf{A_{vsc,R,1}}\mathbf{P_I} + \mathbf{P_I}\mathbf{A_{vsc,R,1}}^{\intercal} + \mathbf{B_{vsc,R,1}}\mathbf{W} + \mathbf{W}^{\intercal}\mathbf{B_{vsc,R,1}}^{\intercal},\\
\mathbf{M_{vsc,2}} &= \mathbf{A_{vsc,R,2}}\mathbf{P_I} + \mathbf{P_I}\mathbf{A_{vsc,R,2}}^{\intercal} + \mathbf{B_{vsc,R,2}}\mathbf{W} + \mathbf{W}^{\intercal}\mathbf{B_{vsc,R,2}}^{\intercal},\\
\mathbf{L_{vsc,1}} &= \mathbf{A_{vsc,R,1}}\mathbf{P_I} - \mathbf{P_I}\mathbf{A_{vsc,R,1}}^{\intercal} + \mathbf{B_{vsc,R,1}}\mathbf{W} - \mathbf{W}^{\intercal}\mathbf{B_{vsc,R,1}}^{\intercal},\\
\mathbf{L_{vsc,2}} &= \mathbf{A_{vsc,R,2}}\mathbf{P_I} - \mathbf{P_I}\mathbf{A_{vsc,R,2}}^{\intercal} + \mathbf{B_{vsc,R,2}}\mathbf{W} - \mathbf{W}^{\intercal}\mathbf{B_{vsc,R,2}}^{\intercal},\\
\mathbf{N_{vsc,1}} &= -\mathbf{A_{vsc,R,1}}\mathbf{P_I} + \mathbf{P_I}\mathbf{A_{vsc,R,1}}^{\intercal} - \mathbf{B_{vsc,R,1}}\mathbf{W} + \mathbf{W}^{\intercal}\mathbf{B_{vsc,R,1}}^{\intercal},\\
\mathbf{N_{vsc,2}} &= -\mathbf{A_{vsc,R,2}}\mathbf{P_I} + \mathbf{P_I}\mathbf{A_{vsc,R,2}}^{\intercal} - \mathbf{B_{vsc,R,2}}\mathbf{W} + \mathbf{W}^{\intercal}\mathbf{B_{vsc,R,2}}^{\intercal}.
\end{aligned}
\tag{5.9}
$$

These LMIs can be simultaneously solved by using a Matlab Toolbox for LMIs and appropriate commands. The final result is shown in Equation (5.10).

$$\mathbf{K_{vsc,R}} = \begin{bmatrix} -0.0487 & -0.0005 & 0.0549 & -0.4255 & -6.5895 \\ 0.0033 & -0.0544 & 0.0005 & 7.1143 & -0.0629 \end{bmatrix}. \tag{5.10}$$

### 5.1.4 Controller Implementation

In order to implement the controller, let us create a general approach where $\mathbf{K}_{vsc}$ represents both the LQR and LMI-based gain matrices that are calculated in previous sections. In fact, consider that

$$\mathbf{K_{vsc}} = \begin{bmatrix} k_{11} & k_{12} & k_{13} & k_{14} & k_{15} \\ k_{21} & k_{22} & k_{23} & k_{24} & k_{25} \end{bmatrix}. \tag{5.11}$$

Then, recall that

$$\begin{cases} m_d &= M_d + \tilde{m}_d, \\ m_q &= M_q + \tilde{m}_q. \end{cases} \tag{5.12}$$

Since the small signal variation comes from the variable exchange done in Eq. (4.9), it is possible to write that

$$\begin{cases} m_d &= M_d + \frac{2}{V_{dc}}\tilde{v}_{g,d} + \tilde{u}_d, \\ m_q &= M_q + \frac{2}{V_{dc}}\tilde{v}_{g,q} + \tilde{u}_q. \end{cases} \tag{5.13}$$

Recall that steady state value of $v_{g,d}$ is $\hat{V}_g$ while the expected value of $v_{g,q}$ under steady state is 0. In addition, recall that $\mathbf{u_{vsc}} = \mathbf{K_{vsc}}\mathbf{x_{vsc}}$. Hence

$$\begin{cases} m_d = M_d + \frac{2}{V_{dc}}\left(v_{g,d} - \hat{V}_g\right) + k_{11}\tilde{i}_d + k_{12}\tilde{i}_q + k_{13}\tilde{v}_{dc} + k_{14}x_1 + k_{15}x_2, \\ m_q = M_q + \frac{2}{V_{dc}}v_{g,q} + k_{21}\tilde{i}_d + k_{22}\tilde{i}_q + k_{23}\tilde{v}_{dc} + k_{24}x_1 + k_{25}x_2. \end{cases} \tag{5.14}$$

By recalling equation (4.2) it is possible to write

$$\begin{cases} m_d = M_d + \frac{2}{V_{dc}}\left(v_{g,d} - \hat{V}_g\right) + k_{11}(\bar{i}_d - I_d) + k_{12}(\bar{i}_q - I_q) + k_{13}(\bar{v}_{dc} - V_{dc}) + k_{14}x_1 + k_{15}x_2, \\ m_q = M_q + \frac{2}{V_{dc}}v_{g,q} + k_{21}(\bar{i}_d - I_d) + k_{22}(\bar{i}_q - I_q) + k_{23}(\bar{v}_{dc} - V_{dc}) + k_{24}x_1 + k_{25}x_2. \end{cases} \tag{5.15}$$

If the integrators are to be implemented digitally, it is possible to write that

$$\begin{cases} x_1[t_k] = x_1[t_{k-1}](t_k - t_{k-1}) = (\bar{i}_q^*[t_{k-1}] - \bar{i}_q[t_{k-1}])\Delta t_k, \\ x_2[t_k] = x_2[t_{k-1}](t_k - t_{k-1}) = (\bar{v}_{dc}^*[t_{k-1}] - \bar{v}_{dc}[t_{k-1}])\Delta t_k. \end{cases} \tag{5.16}$$

where $\Delta t_k$ is the time step used by the controller. When using $P_{in}^{init} = 0$, the values from Table 2 and equations (4.4) it is possible to numerically implement the controller as

$$\begin{cases} m_d = 0.9 + 0.005\,(v_{g,d} - 180) + k_{11}\bar{i}_d + k_{12}\bar{i}_q + k_{13}(\bar{v}_{dc} - 400) + k_{14}x_1 + k_{15}x_2, \\ m_q = 0.005 v_{g,q} + k_{21}\bar{i}_d + k_{22}\bar{i}_q + k_{23}(\bar{v}_{dc} - 400) + k_{24}x_1 + k_{25}x_2, \end{cases} \tag{5.17}$$

and

$$\begin{cases} x_1[t_k] = -\bar{i}_q[t_{k-1}]\Delta t_k, \\ x_2[t_k] = (400 - \bar{v}_{dc}[t_{k-1}])\Delta t_k. \end{cases} \tag{5.18}$$

### 5.1.5 **Experiment Set-Up**

The experiment is assembled in PSIM©, for two simulations, each testing one of the controllers developed in this section. The diagram that shows the different components of the simulated system is shown in Figure 26. Note that the control is executed by a C Block component, in the bottom right part of the diagram. The simulation step used for this system is $t_{step} = 1\ \mu s$.

The entire system is simulated for 1.5 seconds. At first, the input power $P_{in}$ changes instantaneously from 0 to 20 $kW$ at instant $t = 0.2\ s$. Later on the input power changes, again instantaneously, from 20 $kW$ to 30 $kW$, or $P_{in}^{max}$, at $t = 0.5\ s$. From $t = 0.8\ s$ to $t = 1.2\ s$, $P_{in}$ changes from $P_{in}^{max}$ to $P_{in}^{min}$, i.e., $-30\ kW$ in a ramp. This change in power profile allows us to have insights on the proposed controllers' performance under a bidirectional power flow.

## 5.2 BTB-VSC SYSTEM

Now, consider the BTB-VSC that performs the interface of two independent AC systems, as depicted in Figure 18 and recall the linear dynamic representation shown in equation (4.23). The next subsections add the sufficient information about the performed experiment in the studied test system.

Figure 26 – Simulation diagram for the single VSC test system.

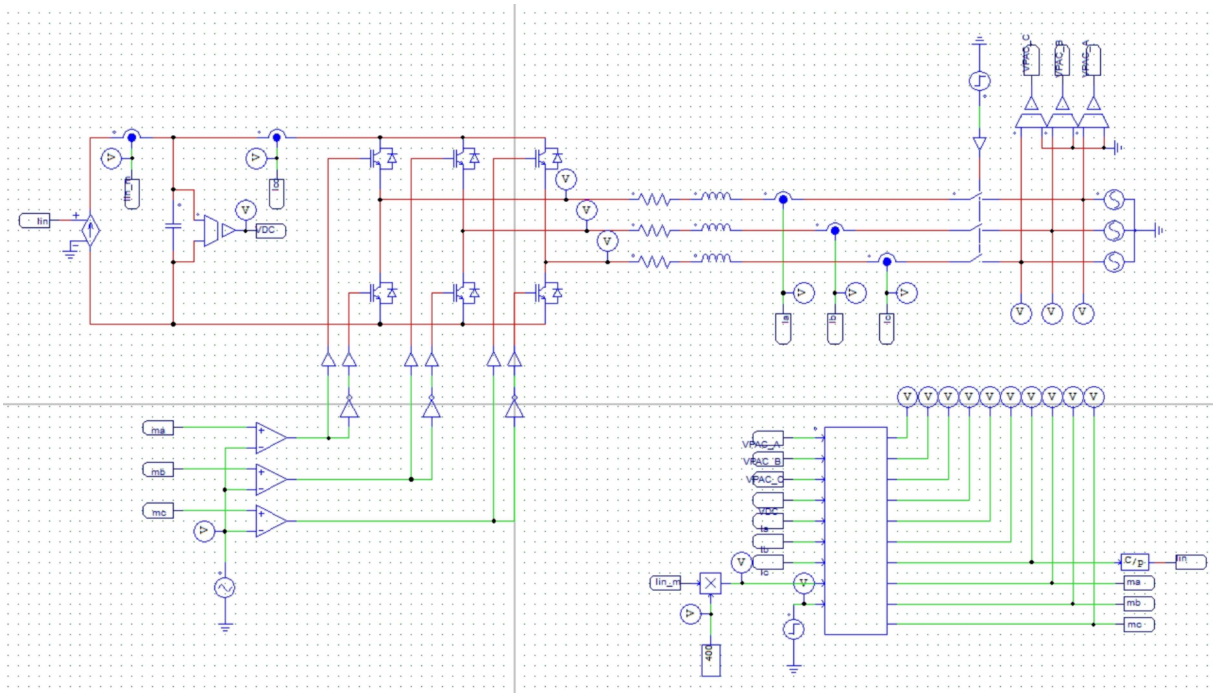

Source: Author (2022).

### 5.2.1 Experiment Description

In this experiment, the controller is designed using the robust pole placement strategy and the system is tested under two different conditions. The first condition is the change in power flow that is seen in the single VSC test system. Here, the same values of power shown in Table 1 are considered and, therefore, there is a bidirectional power-flow between both AC systems. The power values are shown in Table 11.

Table 11 – Input power values for the single VSC test system.

| Description | Value |
|---|---|
| Terminal 1 Maximum Power ($P_1^{max}$) | 30 $kW$ |
| Terminal 1 Minimum Power ($P_1^{min}$) | -30 $kW$ |

Source: Author (2022).

The second condition that is tested in this experiment is a change in the parameters that compose the grid. This is done in order to simulate a disturbance that occurs in the power grid, here represented by the AC system connected to terminal 2. Any disturbance that occurs within the equivalent power grid would affect the values of resistance and inductance that compose the RL branc connecting the voltage source to the PCC. The details about the values that are used in this experiment are discussed on the next subsections.

### 5.2.2 System Description and Parameters

The BTB-VSC system that is tested in this study is depicted as a simplified diagram in Figure 27. Once again, dashed lines correspond to control and measurement signals while electrical connections are represented with a solid dark line. Note that terminal one is directly connected to a voltage source via the RL filter, while terminal two is connected to a power grid, represented by an ideal voltage source in series with an RL branch, as it was discussed in Chapter 3.

Figure 27 – BTB-VSC test system diagram.

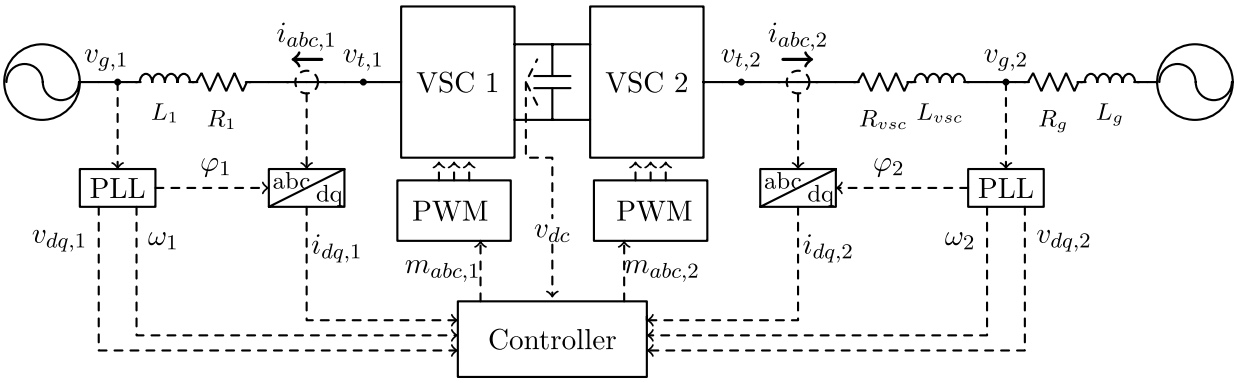


Source: Author (2022).

Note that equivalent resistance and inductance in terminal two are divided into VSC and grid values. The VSC value is fixed and it is equal to the ones at terminal one. On the other hand, grid values are considered to be within a certain range. These pieces of information are summarized on Table 12.

Table 12 – BTB-VSC system parameters.

| Description | Values |
|---|---|
| VSC Terminal Equivalent Inductance ($L_{vsc}$) | 2 $mH$ |
| VSC Terminal Equivalent Resistance ($R_{vsc}$) | 75 $m\Omega$ |
| Grid Equivalent Inductance Range ($L_g$) | [0.2 2] $mH$ |
| Grid Equivalent Resistance Range ($R_g$) | [5 75] $m\Omega$ |

Source: Author (2022).

The remaining parameters for the system depicted Figure 27 are listed on Table 13. Once again, these values are used for the numerical calculation of the linear systems which are needed for designing the assessed control strategy. Both PLL circuits that are employed for synchronization with systems at terminals one and two are designed following the same principle that is presented in the single VSC test system. Both PLL are also tuned using the same parameters as the ones shown in Table 3.

Table 13 – BTB-VSC system parameters.

| Description | Value |
|---|---|
| RMS Line Voltage at both PCC ($v_{g,rms}$) | 220 $V$ |
| Grid Frequency ($f$) | 60 $Hz$ |
| Grid Frequency ($\omega$) | 376.99 $rad/s$ |
| DC Bus Capacitance ($C_{dc}$) | 2 $mF$ |
| Capacitor Parallel Resistance ($r_c$) | 1 $k\Omega$ |
| DC Bus Voltage ($V_{dc}$) | 500 $V$ |
| System 1 Equivalent Inductance ($L_1$) | 2 $mH$ |
| System 1 Equivalent Resistance ($R_1$) | 75 $m\Omega$ |
| System 2 Equivalent Inductance ($L_2 = L_{vsc} + L_g$) | [2.2 4] $mH$ |
| System 2 Equivalent Resistance ($R_2 = R_{vsc} + R_g$) | [80 150] $m\Omega$ |
| Switching Frequency for both VSCs ($f_s$) | 20 $kHz$ |

Source: Author (2022).

### 5.2.3 **Control Design**

As it was already discussed, the LMI-based robust pole placement strategy assessed in this study can take into consideration a range of operation conditions. The different operation conditions that are studied here take into consideration the variation of three parameters: power reference in terminal one, grid resistance and grid inductance. Since each parameter has a maximum and a minimum value, the total number of possible combinations is $2^3 = 8$. Therefore, eight different linear systems should be considered and their description is summarized in Table 14.

Table 14 – Combination of operating conditions.

| Condition Number | Terminal One Power | Grid Resistance | Grid Inductance |
|---|---|---|---|
| 1 | $P_1^{min}$ | $R_g^{min}$ | $L_g^{min}$ |
| 2 | $P_1^{min}$ | $R_g^{min}$ | $L_g^{max}$ |
| 3 | $P_1^{min}$ | $R_g^{max}$ | $L_g^{min}$ |
| 4 | $P_1^{min}$ | $R_g^{max}$ | $L_g^{max}$ |
| 5 | $P_1^{max}$ | $R_g^{min}$ | $L_g^{min}$ |
| 6 | $P_1^{max}$ | $R_g^{min}$ | $L_g^{max}$ |
| 7 | $P_1^{max}$ | $R_g^{max}$ | $L_g^{min}$ |
| 8 | $P_1^{max}$ | $R_g^{max}$ | $L_g^{max}$ |

Source: Author (2022).

The linear matrices are calculated taking into consideration the parameters for the different combinations described in Table 14, the values on Table 13 and the initial conditions stated on Table 15. Recall that values related to measured voltages are outputs from the PLL circuit, while quadrature current reference values are always set to zero.

Table 15 – Equilibrium conditions for BTB controller design.

| Description | Value |
|---|---|
| Tracked Voltage Value on Direct Axis at Terminal 1 ($V_{g,d,1}$) | 180 $V$ |
| Tracked Voltage Value on Quadrature Axis at Terminal 1 ($V_{g,q,1}$) | 0 $V$ |
| Initial Qudrature Current in Terminal 1 ($I_{q,1}$) | 0 $A$ |
| Tracked Voltage Value on Direct Axis at Terminal 2 ($V_{g,d,2}$) | 180 $V$ |
| Tracked Voltage Value on Quadrature Axis at Terminal 2 ($V_{g,q,2}$) | 0 $V$ |
| Initial Quadrature Current in Terminal 2 ($I_{q,2}$) | 0 $A$ |

Source: Author (2022).

Combining the information available in all Tables, it is possible to solve the set of equations (4.15) for all eight cases and to assemble the pair ($\mathbf{A_{btb}}$,$\mathbf{B_{btb}}$) for each case. The matrices resulting from the calculation procedure performed for each case are omitted but the process is analogous to the one presented for the single VSC controller strategy based on robust pole placement via LMIs. Now that matrices are ready, it is necessary to determine the regio $\mathcal{S}$ in which the poles should be all located. The parameters that allow such region to be assembled are summarized in Table 16.

Table 16 – Pole placement region information for BTB controller design.

| Description | Value |
|---|---|
| Minimum attenuation ($\alpha_{btb}$) | 121.2 $s^{-1}$ |
| Minimum damping ($\theta_{btb}$) | 50 $^\circ$ |
| Maximum radius ($\rho_{btb}$) | 12566.37 $s^{-1}$ |

Source: Author (2022).

By using the pair of matrices ($\mathbf{A_{btb}}$,$\mathbf{B_{btb}}$) assembled for each case and the parameters available on Table 16, it is possible to assemble the eight sets of equations (4.41) that are solved simultaneously. Once again, they are solved using a Matlab Toolbox for LMIs and appropriate commands. The final result is shown in (5.19).

$$\mathbf{K_{btb}} = \begin{bmatrix} \mathbf{K_s} & \mathbf{K_c} \end{bmatrix}. \tag{5.19}$$

where

$$\mathbf{K_s} = \begin{bmatrix} -0.0575 & -0.0017 & -0.0462 & 0.0014 & 0.0874 \\ 0.0028 & -0.0442 & -0.0017 & -0.0007 & 0.0007 \\ 0.0030 & 0.0001 & -0.0257 & -0.0042 & -0.0028 \\ 0.0089 & -0.0014 & 0.0081 & -0.0669 & -0.0116 \end{bmatrix}, \tag{5.20}$$

and

$$\mathbf{K_c} = \begin{bmatrix} 1.1280 & -0.1700 & 0.0164 & -11.1748 \\ -0.2385 & 6.1297 & 0.1163 & -0.0027 \\ -4.3244 & -0.0155 & -0.0937 & 1.6905 \\ -0.8086 & 0.2023 & 11.0824 & 1.8159 \end{bmatrix}. \tag{5.21}$$

### 5.2.4 Controller Implementation

The controller implementation here is done similarly to what is presented for the single VSC but with the corresponding variables and matrices. In this case, suppose a matrix equation as

$$\begin{bmatrix} m_{d,1} \\ m_{q,1} \\ m_{d,2} \\ m_{q,2} \end{bmatrix} = \begin{bmatrix} M_{d,1} + \dfrac{2}{V_{dc}}(v_{g,d,1} - \hat{V}_{g,1}) \\ M_{q,1} + \dfrac{2}{V_{dc}} v_{g,q,1} \\ M_{d,2} + \dfrac{2}{V_{dc}}(v_{g,d,2} - \hat{V}_{g,2}) \\ M_{q,2} + \dfrac{2}{V_{dc}} v_{g,q,2} \end{bmatrix} + \mathbf{K_s} \begin{bmatrix} \bar{i}_{d,1} - I_{d,1} \\ \bar{i}_{q,1} - I_{q,1} \\ \bar{i}_{d,2} - I_{d,2} \\ \bar{i}_{q,2} - I_{q,2} \\ \bar{v}_{dc} - V_{dc} \end{bmatrix} + \mathbf{K_c} \begin{bmatrix} x_1 \\ x_2 \\ x_3 \\ x_4 \end{bmatrix}, \tag{5.22}$$

where

$$\begin{cases} x_1[t_k] = (\bar{i}^*_{d,1}[t_{k-1}] - \bar{i}_{d,1}[t_{k-1}])\Delta t_k, \\ x_2[t_k] = (\bar{i}^*_{q,1}[t_{k-1}] - \bar{i}_{q,1}[t_{k-1}])\Delta t_k, \\ x_3[t_k] = (\bar{i}^*_{q,2}[t_{k-1}] - \bar{i}_{q,2}[t_{k-1}])\Delta t_k, \\ x_4[t_k] = (\bar{v}^*_{dc}[t_{k-1}] - \bar{v}_{dc}[t_{k-1}])\Delta t_k. \end{cases} \tag{5.23}$$

If the system is initialized with $P_1^{init} = 0$, it is possible to use the parameters on Tables 13 and 15 and equations (4.15) for numerically implementing the controller as

$$\begin{bmatrix} m_{d,1} \\ m_{q,1} \\ m_{d,2} \\ m_{q,2} \end{bmatrix} = \begin{bmatrix} 0.9 + 0.004(v_{g,d,1} - 180) \\ 0.004 v_{g,q,1} \\ 0.9 + 0.004(v_{g,d,2} - 180) \\ 0.004 v_{g,q,2} \end{bmatrix} + \mathbf{K_s} \begin{bmatrix} \bar{i}_{d,1} \\ \bar{i}_{q,1} \\ \bar{i}_{d,2} \\ \bar{i}_{q,2} \\ \bar{v}_{dc} - 500 \end{bmatrix} + \mathbf{K_c} \begin{bmatrix} x_1 \\ x_2 \\ x_3 \\ x_4 \end{bmatrix}, \tag{5.24}$$

where

$$\begin{cases} x_1[t_k] = (\bar{i}^*_{d,1}[t_{k-1}] - \bar{i}_{d,1}[t_{k-1}])\Delta t_k, \\ x_2[t_k] = -\bar{i}_{q,1}[t_{k-1}]\Delta t_k, \\ x_3[t_k] = -\bar{i}_{q,2}[t_{k-1}]\Delta t_k, \\ x_4[t_k] = (500 - \bar{v}_{dc}[t_{k-1}])\Delta t_k. \end{cases} \tag{5.25}$$

### 5.2.5 **Experiment Set-Up**

The BTB-VSC test system and the LMI-based controller are implemented in PSIM© for two simulations. Each simulation is designed to test the controller in different conditions: a switch in the power flow and a disturbance in the line parameters of the grid. The diagram depicted in Figure 28 shows the different components of the simulated system. Note that, once again, the control is executed by a C Block component, shown in the bottom part of the diagram. The simulation step used for both simulations is $t_{step} = 1\ \mu s$ and both simulation last for 0.6 second.

Figure 28 – Simulation diagram for the BTB-VSC test system.

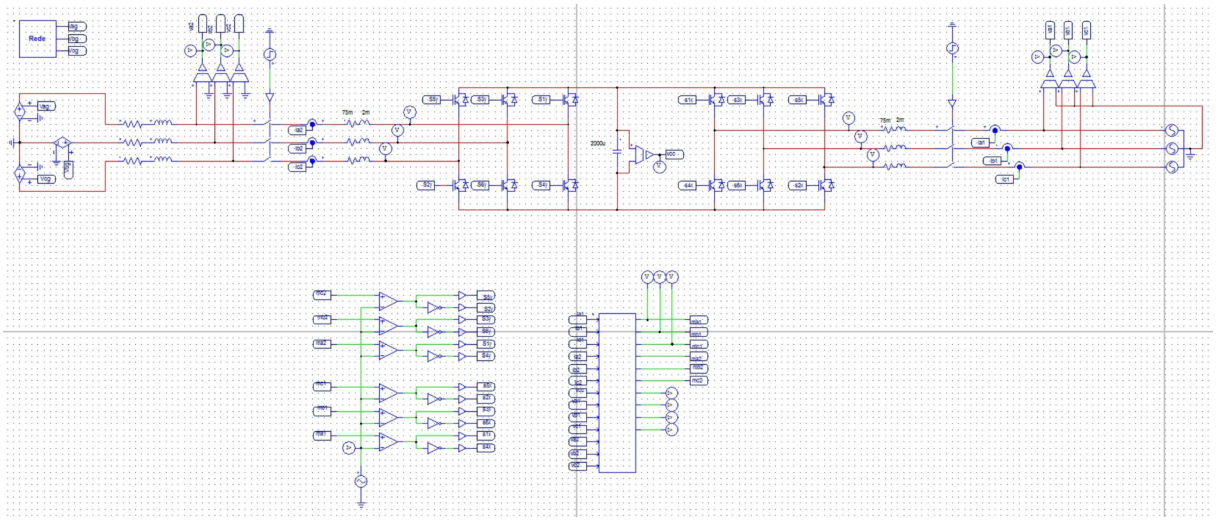

Source: Author (2022).

In the first simulation, the grid resistance and inductance are maintained constant throughout the simulation, totalling $R_2 = 100m\Omega$ and $L_2 = 3.2mH$. The power reference changes from 0 to $10kW$ and then to $30kW$ in $t = 0.1\ s$ and $t = 0.2\ s$, respectively. The power reference changes again to $-30kW$ in a ramp starting from $t = 0.3$ and ending at $t = 0.4\ s$. In the second simulation, the power reference changes from 0 to $30kW$ in $t = 0.1\ s$ and is kept constant in the rest of the simulation. At $t = 0.32\ s$, grid inductance value in the PCC changes abruptly from $L_2 = 2.2$ to $L_2 = 4$, while resistance is constant and equal to $R_2 = 100m\Omega$. This is done in order to simulate a disturbance in the power grid modifying its equivalent inductance value which is represented in the model.

# 6 SIMULATIONS RESULTS

This chapter summarizes the results found when simulating the two studied systems in the different conditions that are presented in the previous chapter. Results are first separated into the different studied test systems and, then, they are grouped according to what is being tested in the particular simulation experiment.

## 6.1 SINGLE VSC SYSTEM

This section summarizes the results for the studied single VSC system. The results are separated into the different controllers that are tested with this system. Recall that the main event that happens in this simulation is the power flow between the DC and the AC systems that changes during the simulation.

### 6.1.1 LQR Results

The results related to the single VSC system controlled by an LQR are shown in this subsection. The active input power reference and the actual measured input power are presented on Figure 29. It is possible to note that the controller can track the reference for the designed value of 20 $kW$ and also for the values of 0 $kW$ and 30 $kW$. However, note that, when the power flow between the DC and the AC systems is inverted, the LQR-based controller cannot track the reference anymore, compromizing the stability of the entire system.

Figure 29 – Active input power reference and the actual measured value for the VSC controlled by the LQR.

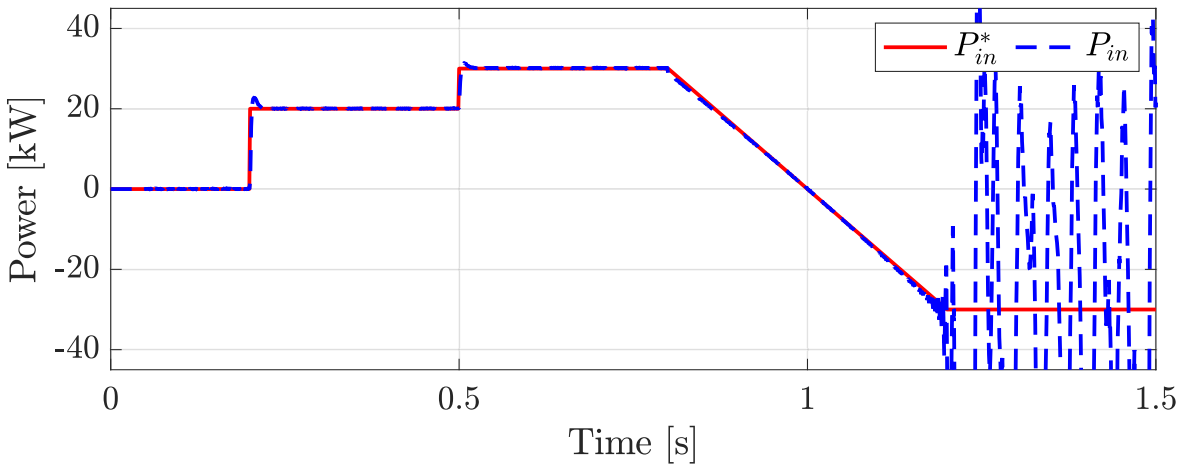


Source: Author (2022).

This fact is corroborated by Figure 30, in which the behavior of the DC bus voltage along with the reference value are depicted. Note that the voltage has variations in time instants in which the value of $P_{in}$ changes, such as $t = 0.2\ s$ and $t = 0.5\ s$. However, as

one can observe, the controller acts rapidly to restore the DC bus voltage to its reference value. Once again, note that in the instant in which the input power shows an unstable behavior, the controller cannot act on the maintenance of the DC bus voltage.

Figure 30 – DC bus voltage behavior for the VSC controlled by the LQR.

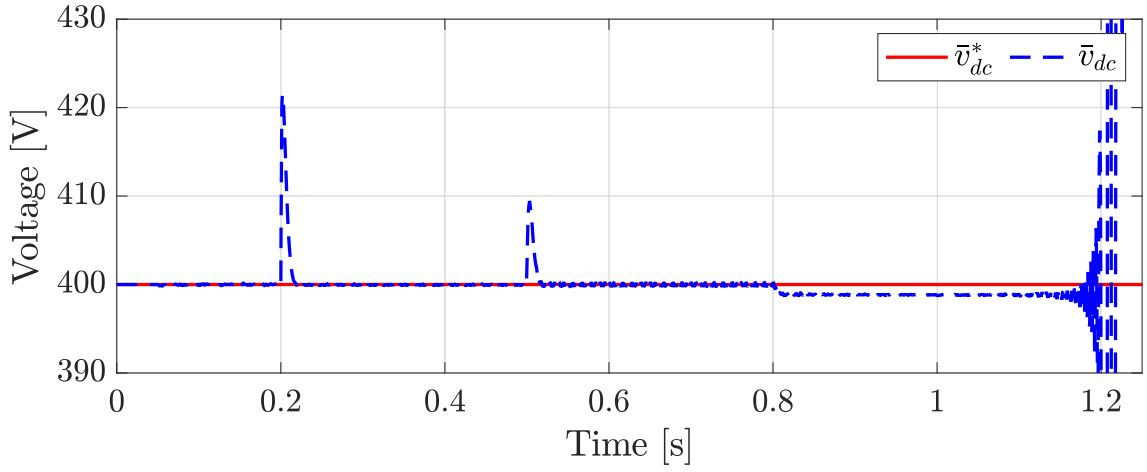


Source: Author (2022).

The behaviors of all three-phase currents, $i_a(t)$, $i_b(t)$ and $i_c(t)$, along with direct-axis component current, $i_d(t)$ are shown in Figures 31 and 32. In the former, it is possible to observe that the currents present the expected behavior, increasing their magnitude as input power $P_{in}$ successively increases. However, as one can observe in the latter Figure, the controller fails at the instant in which the input power is completely inverted.

Figure 31 – Current behavior for the LQR-controlled VSC during time interval between 0.15 and 0.65 $s$.

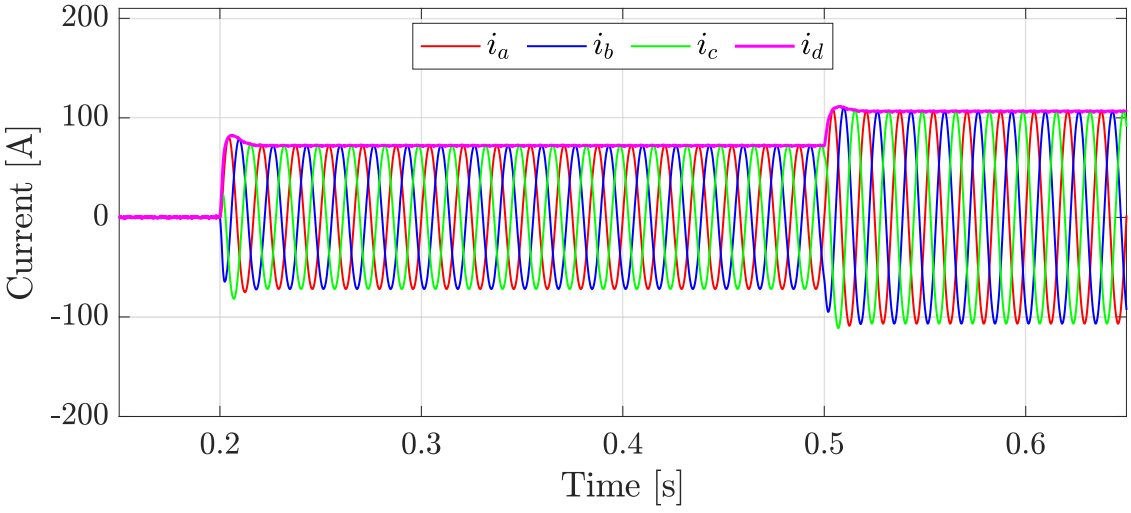


Source: Author (2022).

The unstable behavior that is presented in Figures **??**, **??** and **??** can be more deeply understood when the eigenvalues for the closed loop system are presented. Figure

Figure 32 – ICurrent behavior for the LQR-controlled VSC during time interval between 0.775 and 1.225 $s$.

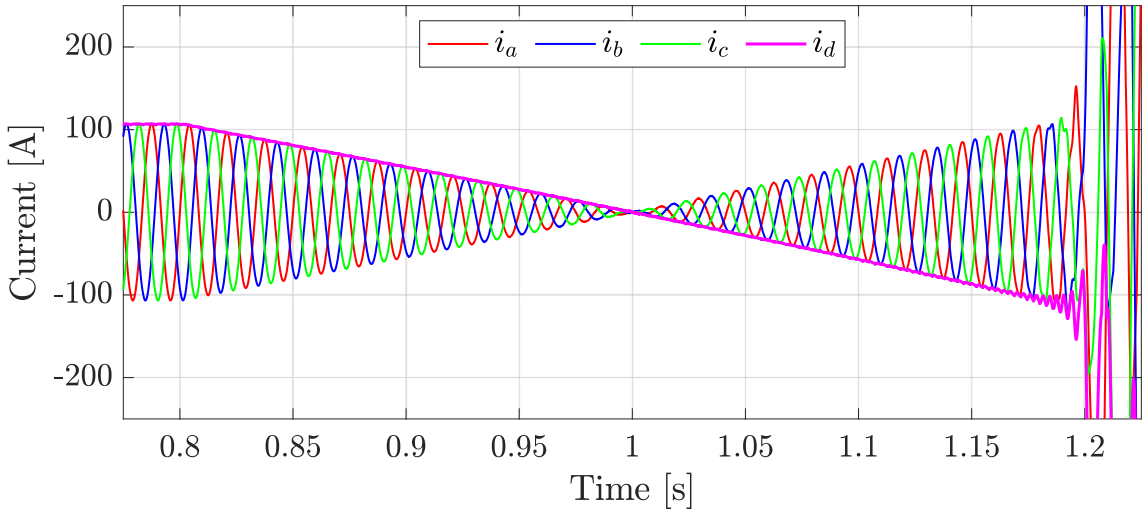


Source: Author (2022).

33 depicts the closed loop eigenvalues of the LQR-controlled single VSC system while $P_{in}$ varies from $P_{in}^{max}$ to $P_{in}^{min}$. Note that for some values of $P_{in}$, there is a pair of eigenvalues that appears on the right-hand side of the complex plane, justifying the observed unstable dynamics. The issue that caused this instability is the fact that the LQR controller was designed for a single operation point, i.e., $P_{in} = 20\ kW$, and the behavior under other operating points is not taken into consideration during the design procedure. One option that could solve this problem would be to iteratively design the LQR controller while checking if all operating points have stable eigenvalues. Although it is not guaranteed that the system is stable between two data points representing stable operating conditions, this root-locus-inspired routine could allow some preliminary assessment of the system's overall stability.

### 6.1.2 Robust Pole Placement Results

The results related to the single VSC system controlled by the LMI-based robust pole placement controller are shown in this subsection. First, the active input power reference is compared with the actual measured value in Figure 34. Note that, this time, the controller enables the system to properly follow the power reference, even during the power flow inversion that occurs between instants $t = 0.8s$ and $t = 1.2s$.

The behavior of the DC-bus voltage, together with the reference value, is presented on Figure 35. Note that variations are observed soon after the time instants where the input power $P_{in}$ changes its value. However, the LMI-based controller acts on returning the DC-bus voltage to its designed steady state value.

The behaviors of all three-phase currents, $i_a(t)$, $i_b(t)$ and $i_c(t)$, on the VSCs terminal

Figure 33 – Closed-loop eigenvalues using LQR-based controller for different values of $P_{in}$.

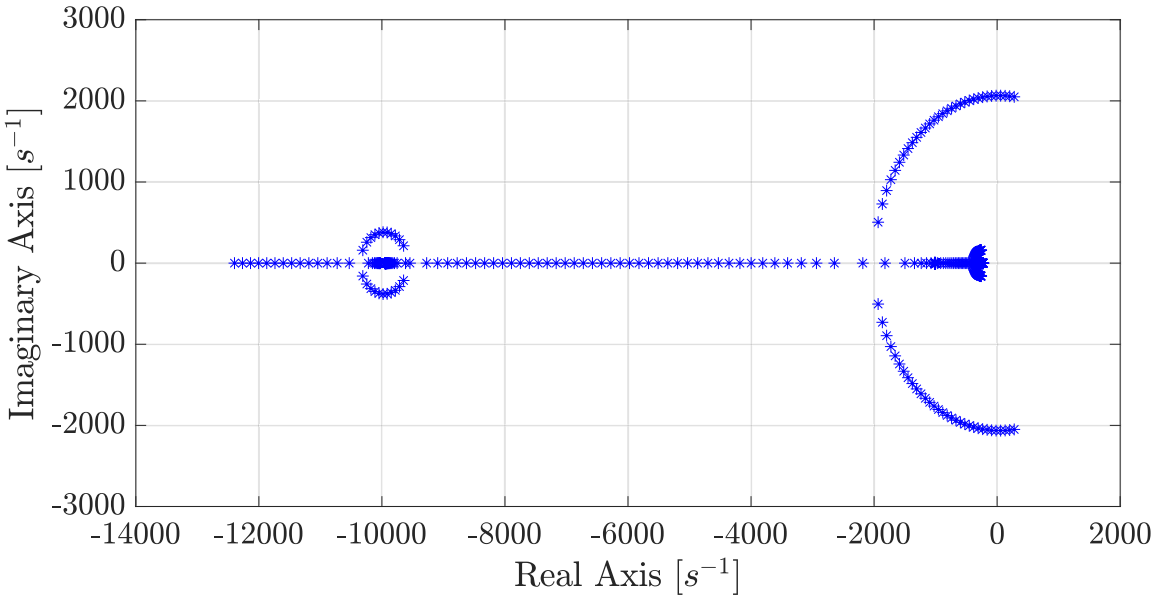


Source: Author (2022).

Figure 34 – Active input power reference and the actual measured value for the VSC using the robust controller.

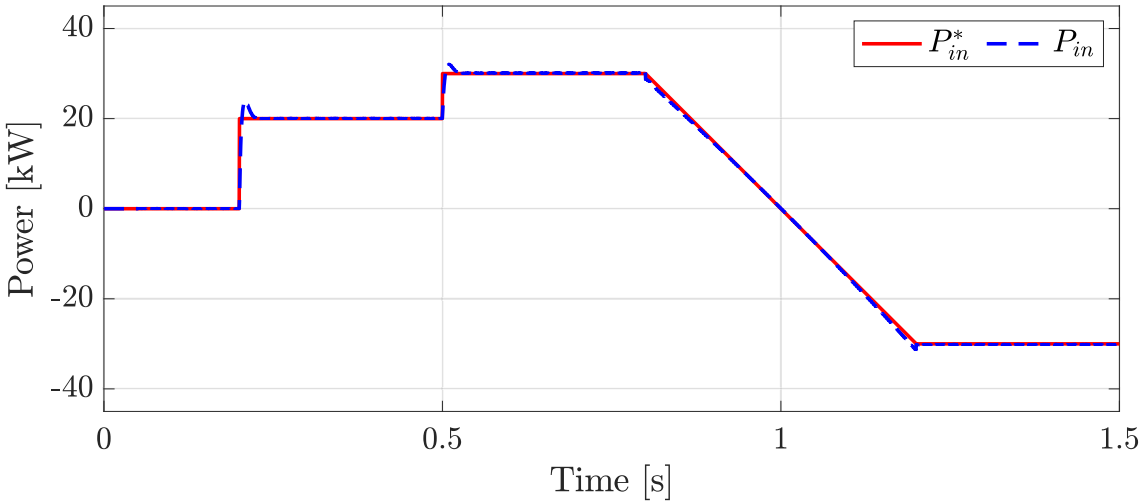


Source: Author (2022).

along with the corresponding direct-axis component current, $i_d(t)$ are shown in Figures 36 and 37. It is easy to observe that, differently to what is observed for the VSC using an LQR-based controller, the currents maintain a stable behavior even after the input power has been completely inverted.

The closed loop eigenvalues for different values of $P_{in}$ together with the desired region $\mathcal{S}$ (dashed dark lines) are shown in Figures 38 and 39. Note that all the eigenvalues, for all operating points, are located inside the desired region of the complex plane, allowing the system to have desired performance under different operating conditions. It is also important to note that this was achieved by only considering two equilibrium points: the

Figure 35 – DC bus voltage behavior for the VSC using the robust controller.

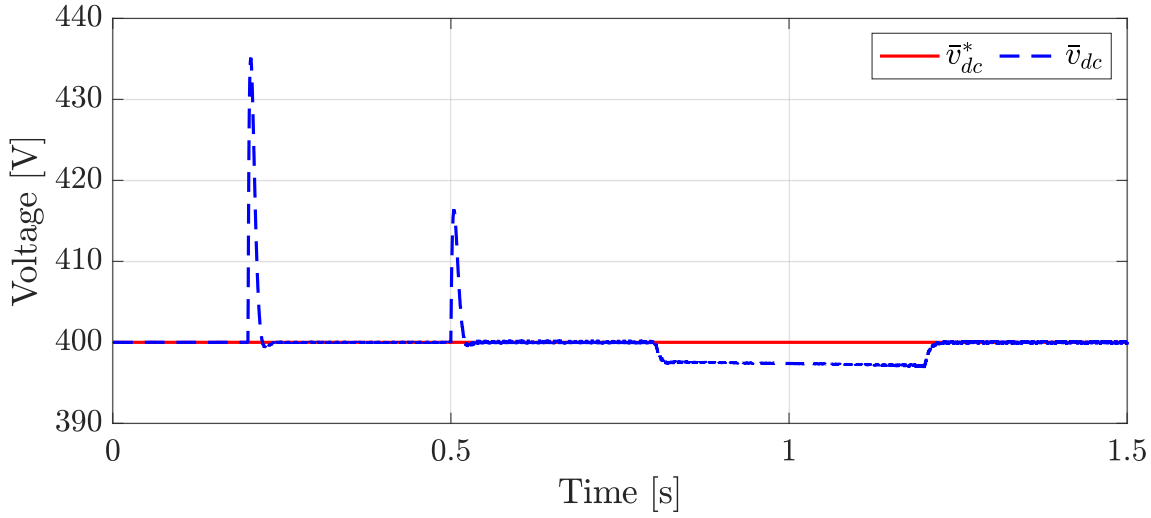


Source: Author (2022).

Figure 36 – Current behavior for the VSC using a robust controller during time interval between 0.15 and 0.65 $s$.

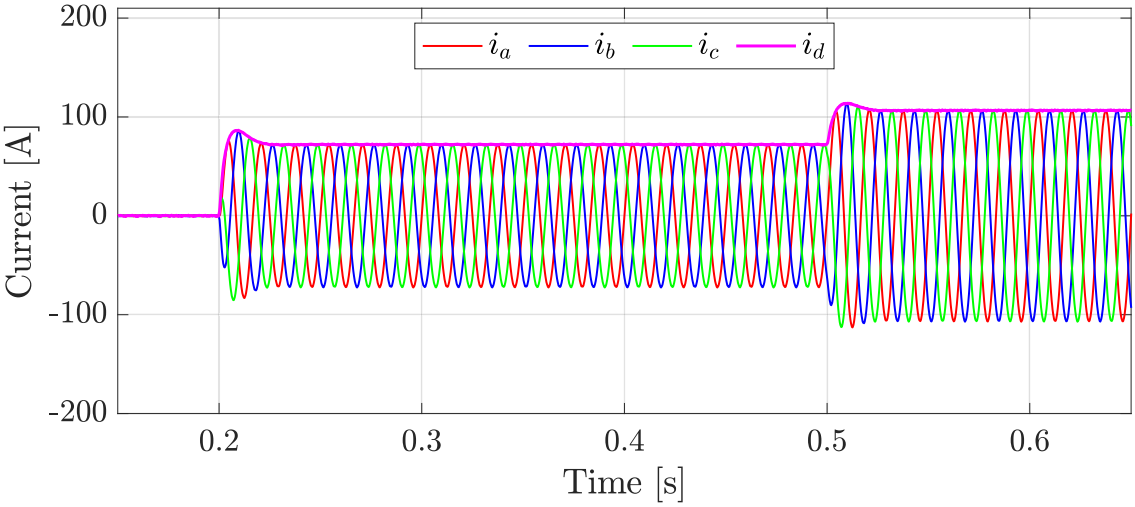


Source: Author (2022).

extremes $P_{in}^{max}$ and $P_{in}^{min}$.

## 6.2 BTB-VSC SYSTEM

This section summarizes the results obtained on the simulation of the BTB-VSC system. Results are separated for the two different simulations that are conducted in this study: the power inversion and the disturbance involving the equivalent RL branch on terminal 2. In addition to that, this section starts by showing the closed loop eigenvalues for the eight different operating points that are considered for the controller design on Figures 40 and 41. Note that all eigenvalues are located inside the desired region $\mathcal{S}$, which is drawn using dashed dark lines. As it was already mentioned, the design procedure only

Figure 37 – Current behavior for the VSC using a robust controller during time interval between 0.775 and 1.225 $s$

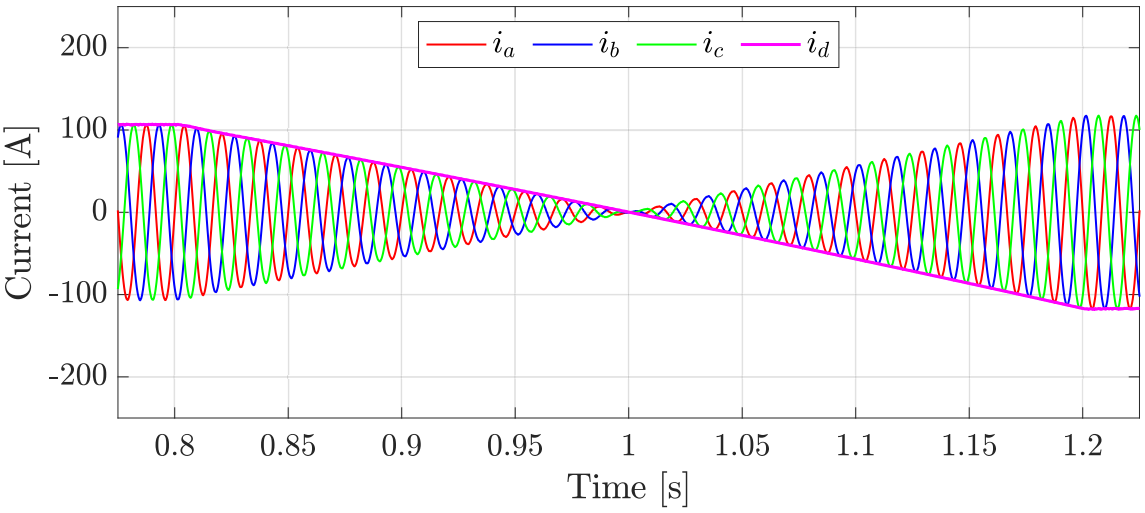


Source: Author (2022).

Figure 38 – Closed loop poles for the single VSC system using the robust controller.

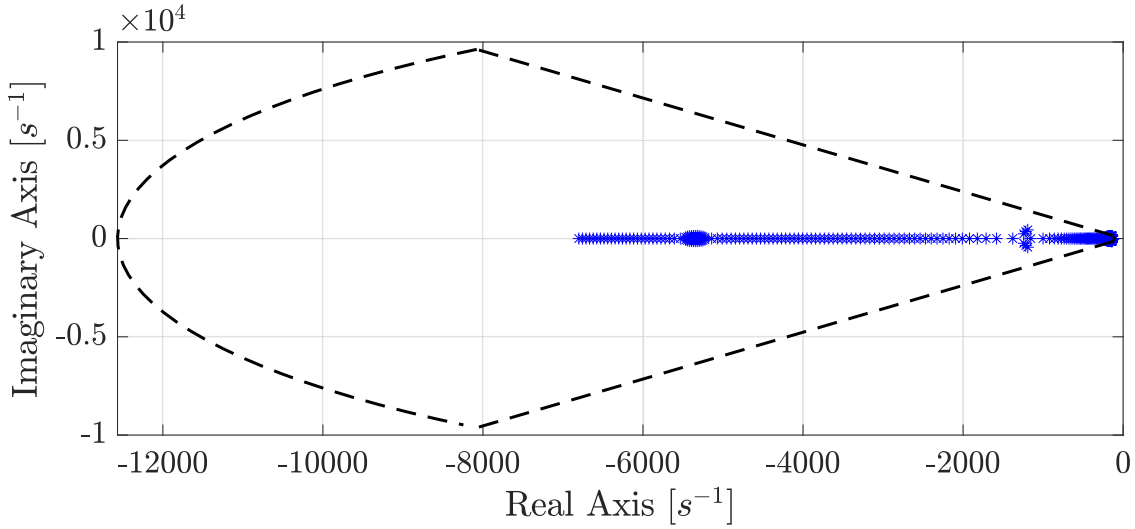


Source: Author (2022).

needs to consider the extreme of each range of operating conditions. Similarly to the single VSC test system, it is expected that all closed loop poles for all different operating conditions to be located inside $\mathcal{S}$ by using the LMI-based technique.

### 6.2.1 Bidirectional Power Flow Simulation

First, consider the simulation where the power flow between AC systems one and two is inverted. The power behavior on terminal one is presented on Figure 42 and note that the power reference value is met with a smooth behavior. Also observe that the power inversion is performed without any issue.

Because of that, the three-phase currents also change accordingly, with a smooth

Figure 39 – Closed loop poles for the single VSC system using the robust controller.

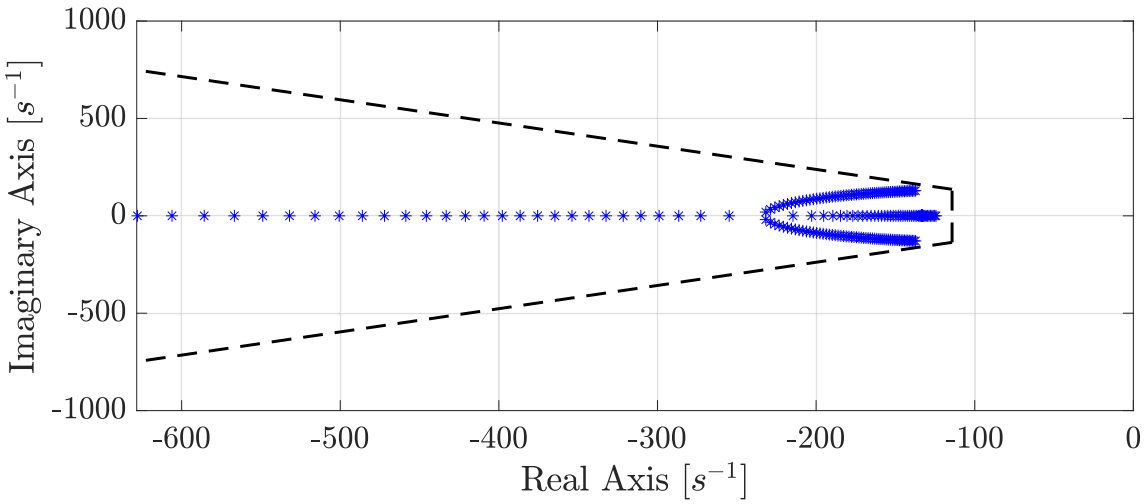


Source: Author (2022).

Figure 40 – Closed loop poles for the BTB-VSC system.

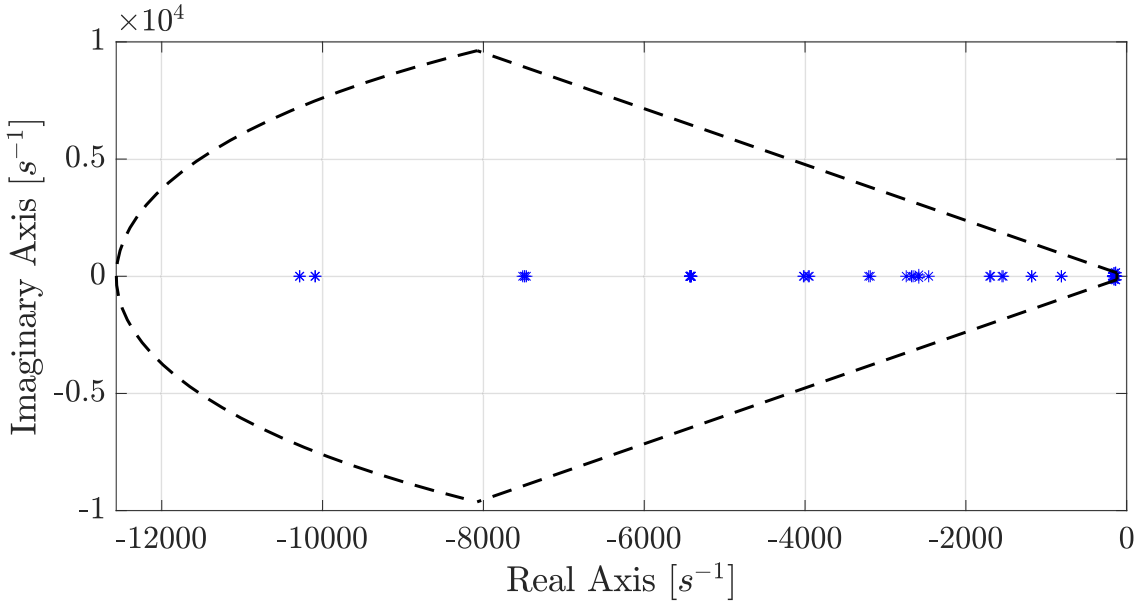


Source: Author (2022).

behavior, when the power reference is changed, as it is shown in Figure 43. Note that there is no overshoot that can be observed, even when the reference changes abruptly as in a step function.

The DC-bus voltage behavior during the simulation is shown in Figure **??**. Note that changes in the voltage value are observed in the instants where the power reference changes. However, the voltage value has less than $10V$ variation for any terminal one power reference change, accounting for approximately 1.5% variation of its reference value.

Figure 41 – Zoom in closed loop poles for the BTB-VSC system.

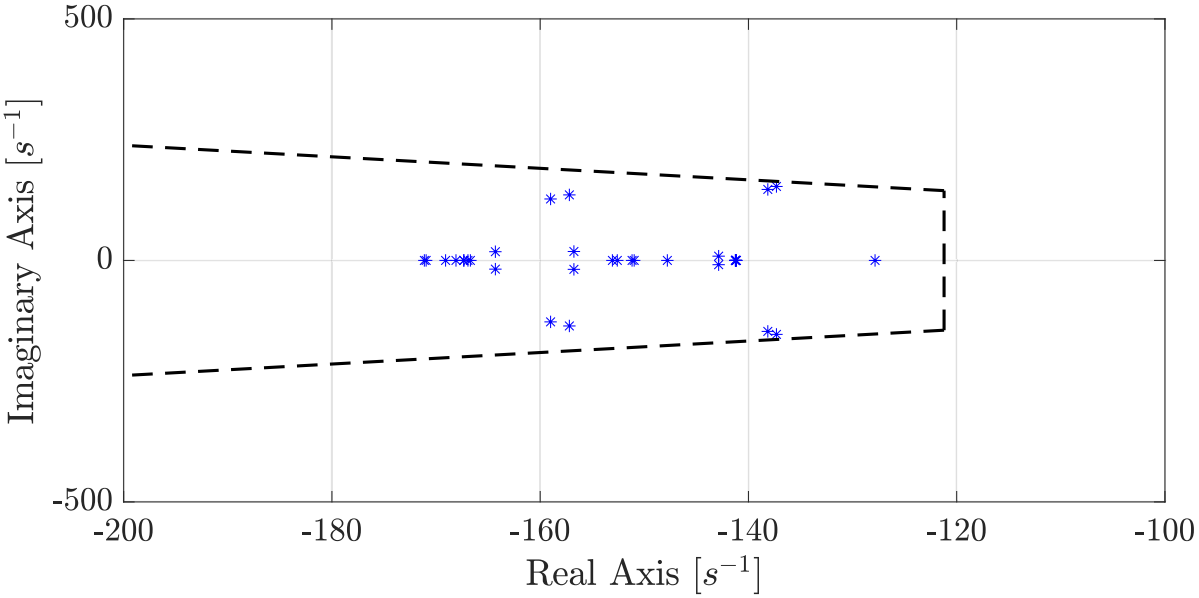


Source: Author (2022).

Figure 42 – Power behavior in terminal 1 of BTB-VSC for power flow inversion case.

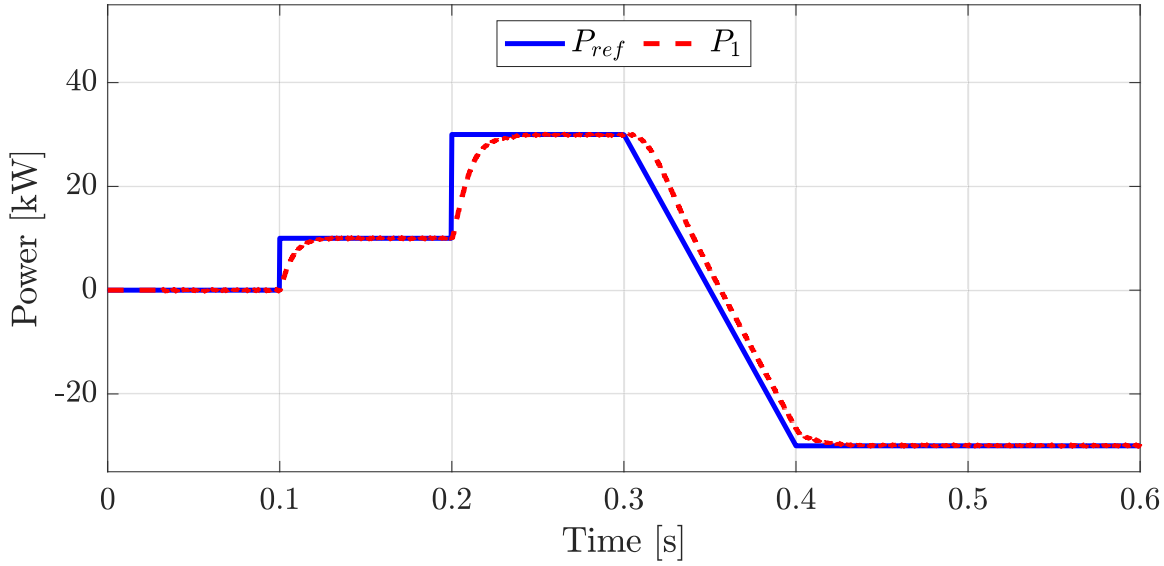


Source: Author (2022).

### 6.2.2 Line Impedance Disturbance Simulation

Now, consider the simulation where the line inductance value changes mid-simulation from 0.2 to 2 $mH$ at time instant $t = 0.32$ $s$. First note that the power reference for terminal one changes from 0 to 30 $kW$ at $t = 0.1$ $s$ and then it is kept constant at the maximum value for the rest of the simulation. This is shown in Figure 45. Note that, at the instant in which the inductance value changes, there is a small sag in the instant power measured in terminal one.

Figure 43 – Current injected in terminal 2 of BTB-VSC for power flow inversion case.

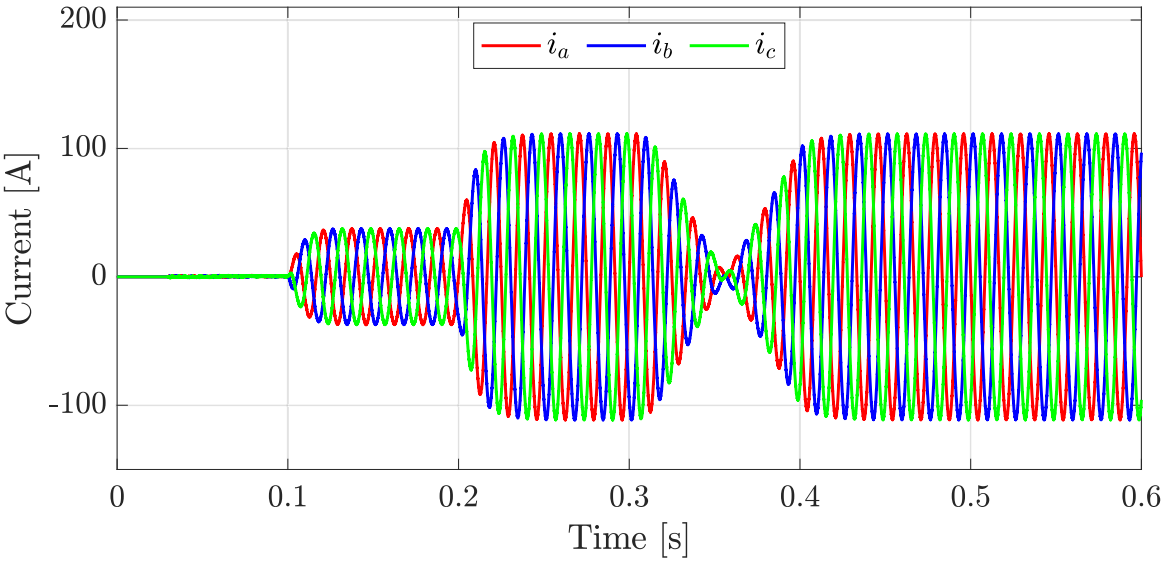


Source: Author (2022).

Figure 44 – Voltage over DC bus capacitor for power flow inversion case.

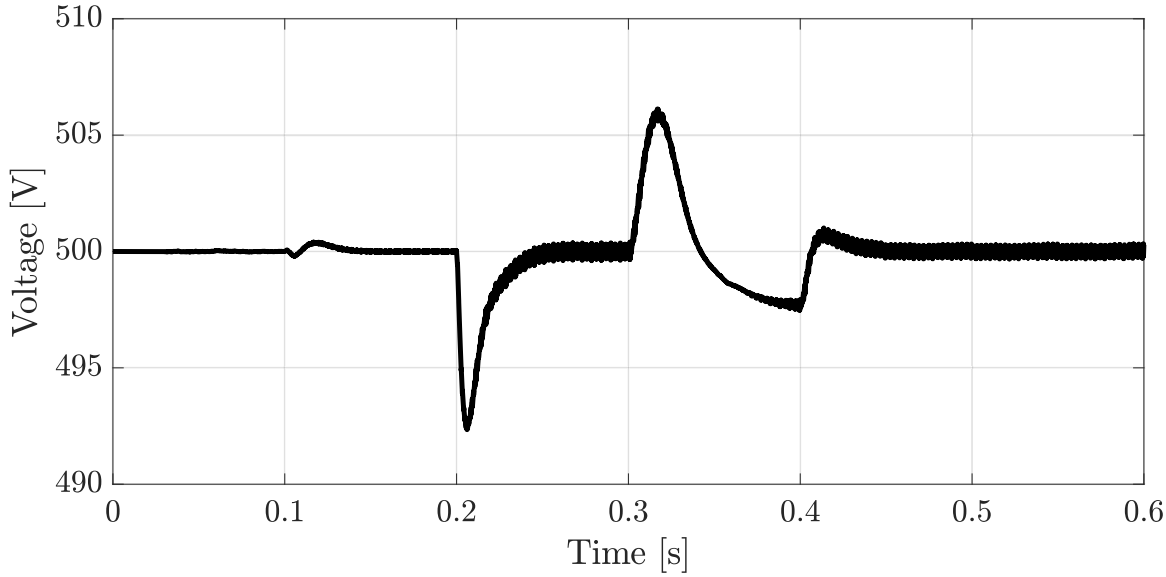


Source: Author (2022).

The line inductance change, which is considerable, translates into small changes in the three-phase currents as it is depicted in Figure 46. Note that the disturbance is almost negligble in the three-phase currents.

In addition to that, the DC bus voltage has less than 5 $V$ variation during the line inductance change, as it is presented in Figure 46. This variation corresponds to less than 1%, showing that the design controller deals very well with abtupt changes in grid impedance and with bidirectional power flow variations between the two AC systems.

Figure 45 – Power behavior in terminal 1 of BTB-VSC for grid impedance disturbance case.

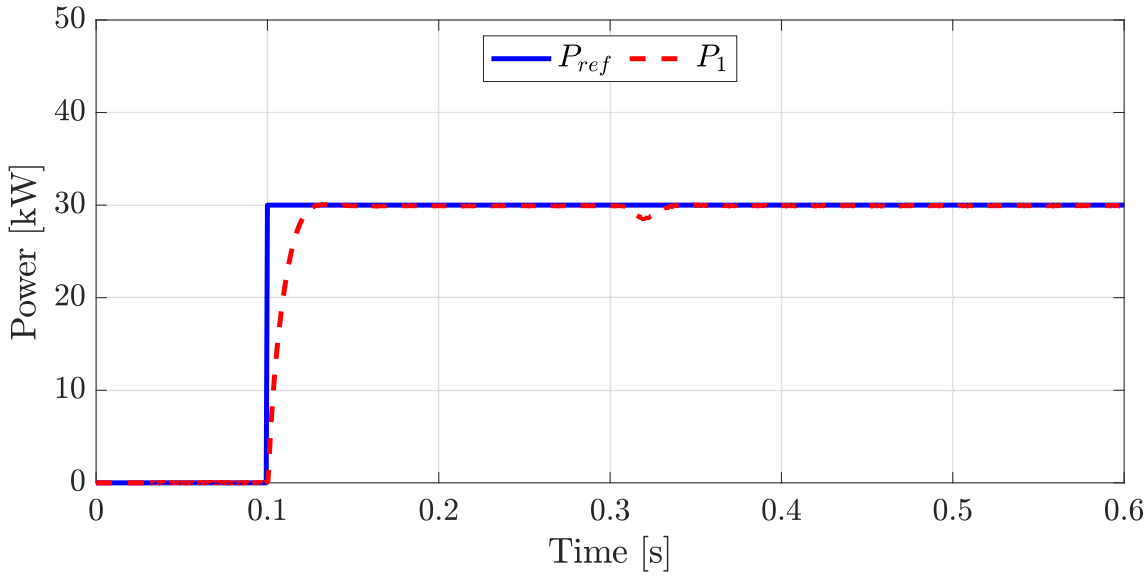


Source: Author (2022).

Figure 46 – Current injected in terminal 2 of BTB-VSC for grid impedance disturbance case.

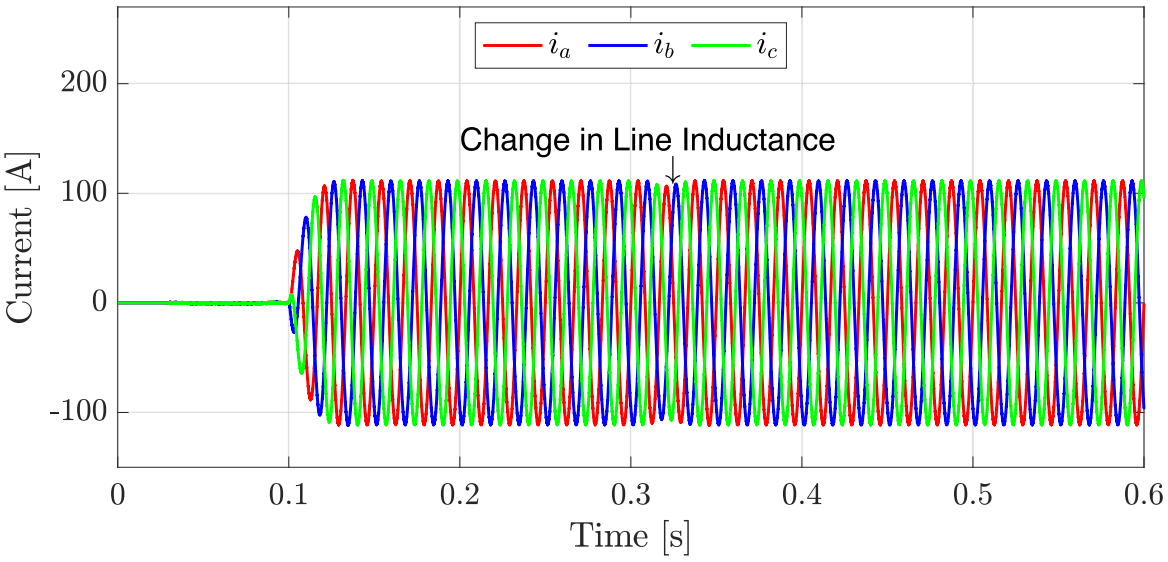


Source: Author (2022).

Figure 47 – Voltage over DC bus capacitor for grid impedance disturbance case.

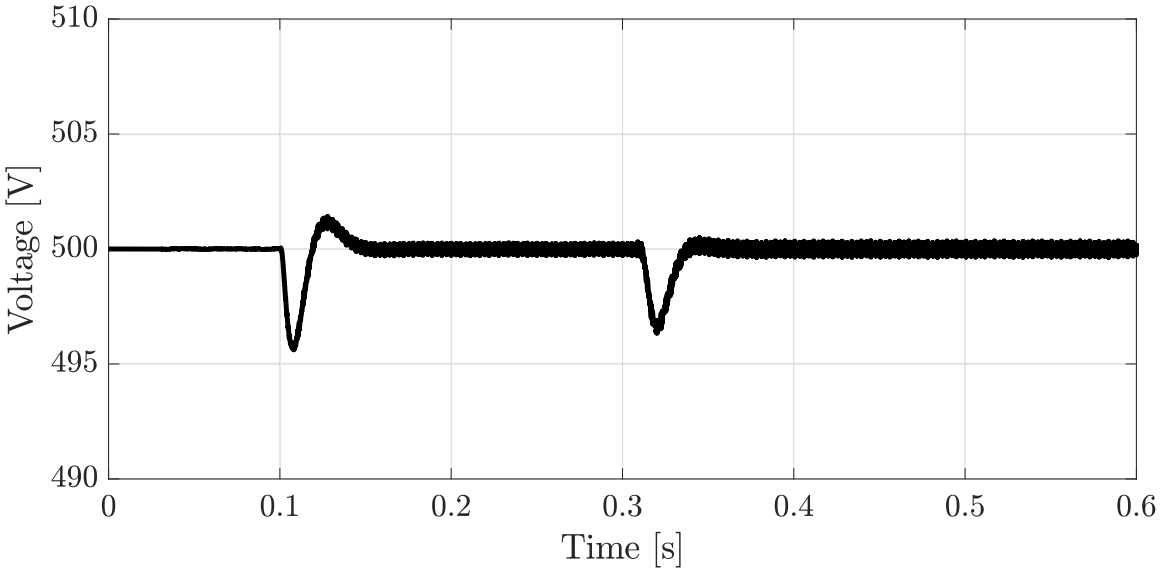


Source: Author (2022).

# 7 CONCLUSION

In this study, the mathematical fundamentals for modeling voltage-sourced converters is laid down and then used in different parts of the research presented here. Linear algebra concepts, such as norm and eigenvalue matrix decomposition, are described given the application context on power electronics converters. Theoretical tools commonly used in the study of nonlinear systems, such as averaging and linearization, are described with appropriate details and are applied for obtaining adequately precise models for the converters assessed in this study. The ammount of detail and theoretical content in this study can be further used as a guide for future students that aim at understanding the modeling of power electronic devices and control applications related to these converters that are currently becoming more frequent in power systems worldwide.

The models that are obtained in this study match the ones that are commonly present in literature, although sligthly different techniques are used for obtaining the average model, for example. In addition to that, the results provided in this paper corroborate to the fact that models obtained in this study are adequate for control purposes, especially if linear techniques are used. In fact, state-space representation is used for exploring a multivariable approach, allowing modern control techniques to be implemented and tested in different converters and simulations.

Two multivariable control strategies are developed, implemented and assessed for controlling a single VSC interfacing a DC and an AC systems: an LQR-based controller and an LMI-based robust pole placement strategy. The DC bus system is connected to a current source that can be used to represent energy consumption or generation on that side of the system. Both strategies are tested in order to assess each control's performance under the different power profiles demanded by the DC-bus-connected system. Results show that, although the LQR might seem simpler in the controller development, especially considering the state feedback gain matrix calculation, it might not be straightforward when designing such controller for different operating points. In fact, an appropriate design would have to undergo successive iterations to assess the system's overall stability under the different equilibria. This is illustrated by the fact that the obtained controller, which was designed considering one operating point, was not stable when large values of power are being consumed by the DC system. On the other hand, the LMI-based pole placement strategy used in this study took presented a stable behavior for all values of input power by the DC bus, even negative ones. This is because the control design procedure takes these extreme values into consideration and guarantee that, if a state-feedback gain matrix is found, the system will be stable for all values within the range of the limit points used in the design.

Comparing both strategies, their practical implementation is basically the same

and what changes is just the gain matrix. The LQR-based strategy requires less efforts in preparing the matrices that will be used in the control design procedure. However, it is clear that the controller is strongly dependant on the equilibrium used for obtaining the linear matrices. If more parameters are expected to vary, then the design procedure of a stable controller starts to become harder and tiresome. On the other hand, the LMI-based approach was shown to be more versatile, showing a stable and adequate dynamic response for the different operating points assessed during simulation.

The versatility of such multivariable strategy was then the subject of testing in the second experiment executed in this study. After the development of a state-pace model for the BTB-VSC system interconnecting two AC systems, the LMI-based robust pole placement strategy was also used for obtaining an appropriate controller for the system being studied. In this case, the control approach was focused not only in allowing a bidirectional power flow over the converter, but also on enabling the BTB-VSC to deal with uncertainties in grid equivalent inducance and resistance at the PCC and possible disturbances that could affect these variables.

The controller is designed, again, using a multivariable approach; taking the dynamic behavior of both AC sides and the DC-link capactor into consideration for one singl controller to deal with both sides. In fact, this is extremely important for its robust performance and, although the set of LMI equations that need to be solved simultaneously is not straightforward to obtain, implementation of the resulting controller is rather simple. The implemented control strategy allows the BTB-VSC to operate succssfully under different grid conditions and power reference values without any issues. The results provided in this study show that the LMI-based controller has a very robust performance under bidirectional power flow and disturbances on grid equivalent impedance. Controlled variables presented smooth dynamic with small overshoot for step changes in reference values and for abrupt change in grid equivalent inductance value. Therefore, considering all the advantages that are observed in this paper, the LMI-based robust pole placement strategies are shown to be very promising alternative control approaches for VSC- and BTB-based systems and, hence, they should be relevant for power electronic applications on power systems in the upcoming years.

# REFERENCES

ALCALA, J.; CARDENAS, V.; RAMIREZ-LOPEZ, A.; GUDINO-LAU, J. Study of the bidirectional power flow in back-to-back converters by using linear and nonlinear control strategies. In: IEEE. **2011 IEEE Energy Conversion Congress and Exposition**. [S.l.], 2011. p. 806–813.

ALMEIDA, P. M. d. Modelagem e controle de conversores estaticos fonte de tensao utilizados em sistemas de geracao fotovoltaicos conectados a rede eletrica de distribuicao. **Juiz de Fora**, 2011.

ANDERSON, B. D.; MOORE, J. B. **Optimal control: linear quadratic methods**. [S.l.]: Courier Corporation, 2007.

ÅSTRÖM, K. J.; MURRAY, R. M. **Feedback systems: an introduction for scientists and engineers**. [S.l.]: Princeton university press, 2010.

BACHA, S.; MUNTEANU, I.; BRATCU, A. I. *et al.* **Power electronic converters modeling and control**. [S.l.]: Springer, 2014. v. 1. 454 p.

BALIGA, B. J. Enhancement-and depletion-mode vertical-channel mos gated thyristors. **Electronics Letters**, IET, v. 15, n. 20, p. 645–647, 1979.

BENNETT, W. New results in the calculation of modulation products. **The Bell System Technical Journal**, Nokia Bell Labs, v. 12, n. 2, p. 228–243, 1933.

BICKFORD, J.; HEATON, A. Transient overvoltages on power systems. In: IET. **IEE Proceedings C (Generation, Transmission and Distribution)**. [S.l.], 1986. v. 133, p. 201–225.

BING, Z.; SUN, J. Frequency-domain modeling of multipulse converters by double-fourier series method. **IEEE Transactions on Power Electronics**, IEEE, v. 26, n. 12, p. 3804–3809, 2011.

BLAABJERG, F.; LISERRE, M.; MA, K. Power electronics converters for wind turbine systems. **IEEE Transactions on industry applications**, IEEE, v. 48, n. 2, p. 708–719, 2011.

CHAPMAN, S. **Electric machinery fundamentals**. [S.l.]: Tata McGraw-Hill Education, 2005.

CHEN, F.; BURGOS, R.; BOROYEVICH, D.; RODRIGUEZ-DIAZ, E.; MENG, L.; VASQUEZ, J. C.; GUERRERO, J. M. Analysis and distributed control of power flow in dc microgrids to improve system efficiency. In: IEEE. **2016 4th International Symposium on Environmental Friendly Energies and Applications (EFEA)**. [S.l.], 2016. p. 1–6.

CHEN, Z. An overview of power electronic converter technology for renewable energy systems. **Electrical drives for direct drive renewable energy systems**, Elsevier, p. 80–105, 2013.

CHERRY, E. C. The duality between interlinked electric and magnetic circuits and the formation of transformer equivalent circuits. **Proceedings of the Physical Society. Section B**, IOP Publishing, v. 62, n. 2, p. 101, 1949.

COZZI, L.; GOULD, T. World energy outlook 2017. **International Energy Agency**, 2017.

DERUSSO, P. M.; CLOSE, C. M.; ROY, R. J. **State variables for engineers**. [S.l.]: Krieger Publishing Co., Inc., 1990.

DOMMEL, H. W. **Electromagnetic Transients Program Reference Manual:(EMTP) Theory Book**. [S.l.]: Bonneville Power Administration, 1986.

DUAN, G.-R.; YU, H.-H. **LMIs in control systems: analysis, design and applications**. [S.l.]: CRC press, 2013.

DULLERUD, G. E.; PAGANINI, F. **A course in robust control theory: a convex approach**. [S.l.]: Springer Science & Business Media, 2013. v. 36.

ENRIGHT, W.; NAYAK, O.; IRWIN, G.; ARRILLAGA, J. An electromagnetic transients model of multi-limb transformers using normalized core concept. In: **IPST'97-International Conference on Power System Transients**. [S.l.: s.n.], 1997. p. 93–98.

ENRIGHT, W. G. **Transformer models for electromagnetic transient studies with particular reference to HVdc transmission.** [S.l.]: University of Canterbury. Department of Electrical and Electronic Engineering, 1996.

FRIEDLI, T.; KOLAR, J. W.; RODRIGUEZ, J.; WHEELER, P. W. Comparative evaluation of three-phase ac–ac matrix converter and voltage dc-link back-to-back converter systems. **IEEE Transactions on industrial electronics**, IEEE, v. 59, n. 12, p. 4487–4510, 2011.

KASSAKIAN, J. G.; SCHLECHT, M. F.; VERGHESE, G. C. **Principles of power electronics**. [S.l.]: Wesley Publishing Company, 1991.

KHALIL, H. K.; GRIZZLE, J. W. **Nonlinear systems**. [S.l.]: Prentice Hall Upper Saddle River, NJ, 2002. v. 3.

KRAUSE, P. C.; WASYNCZUK, O.; SUDHOFF, S. D.; PEKAREK, S. **Analysis of electric machinery and drive systems**. [S.l.]: Wiley Online Library, 2002. v. 2.

KREIN, P. T.; BENTSMAN, J.; BASS, R. M.; LESIEUTRE, B. L. On the use of averaging for the analysis of power electronic systems. **IEEE Transactions on Power Electronics**, IEEE, v. 5, n. 2, p. 182–190, 1990.

LIMONGI, L.; BOJOI, R.; PICA, C.; PROFUMO, F.; TENCONI, A. Analysis and comparison of phase locked loop techniques for grid utility applications. In: IEEE. **2007 Power Conversion Conference-Nagoya**. [S.l.], 2007. p. 674–681.

LIU, K.-Z.; YAO, Y. **Robust control: theory and applications**. [S.l.]: John Wiley & Sons, 2016.

MEERKOV, S. M. The averaging of the trajectories of slow dynamical systems. **Differ. Uravn.**, v. 9, n. 9, p. 1609–1617, 1973.

MILANO, F.; MANJAVACAS, Á. O. **Converter-Interfaced Energy Storage Systems: Context, Modelling and Dynamic Analysis**. [S.l.]: Cambridge University Press, 2019.

MIRANDA, L. M.; VARAJÃO, D.; SANTOS, B. dos; ARAÚJO, R. E.; MOREIRA, C.; LOPES, J. P. Power flow control with bidirectional dual active bridge battery charger in low-voltage microgrids. In: IEEE. **2013 15th European Conference on Power Electronics and Applications (EPE)**. [S.l.], 2013. p. 1–10.

MOHAN, N.; UNDELAND, T. M.; ROBBINS, W. P. **Power electronics: converters, applications, and design**. [S.l.]: John Wiley & Sons, 2003.

OLIVARES, D. E.; MEHRIZI-SANI, A.; ETEMADI, A. H.; CAÑIZARES, C. A.; IRAVANI, R.; KAZERANI, M.; HAJIMIRAGHA, A. H.; GOMIS-BELLMUNT, O.; SAEEDIFARD, M.; PALMA-BEHNKE, R. *et al.* Trends in microgrid control. **IEEE Transactions on smart grid**, IEEE, v. 5, n. 4, p. 1905–1919, 2014.

ORNELAS-TELLEZ, F.; RICO-MELGOZA, J. J.; ESPINOSA-JUAREZ, E.; SANCHEZ, E. N. Optimal and robust control in dc microgrids. **IEEE Transactions on Smart Grid**, IEEE, v. 9, n. 6, p. 5543–5553, 2017.

OSÓRIO, C. R.; KOCH, G. G.; BORIN, L. C.; CLEVESTON, I.; MONTAGNER, V. F. Controlador robusto quasi-deadbeat e relaxações com aplicação em inversores conectados à rede. In: **Eletrônica de Potência**. [S.l.]: SOBRAEP, 2018. v. 23, n. 3, p. 320–329.

RODRÍGUEZ-CABERO, A.; SÁNCHEZ, F. H.; PRODANOVIC, M. A unified control of back-to-back converter. In: IEEE. **2016 IEEE Energy Conversion Congress and Exposition (ECCE)**. [S.l.], 2016. p. 1–8.

RODRIGUEZ, P.; TEODORESCU, R.; CANDELA, I.; TIMBUS, A. V.; LISERRE, M.; BLAABJERG, F. New positive-sequence voltage detector for grid synchronization of power converters under faulty grid conditions. In: IEEE. **2006 37th IEEE Power Electronics Specialists Conference**. [S.l.], 2006. p. 1–7.

SANDERS, J. A.; VERHULST, F.; MURDOCK, J. **Averaging methods in nonlinear dynamical systems**. [S.l.]: Springer, 2007. v. 59.

SETHNA, P.; MORAN, T. Some nonlocal results for weakly nonlinear dynamical systems. **Quarterly of Applied Mathematics**, v. 26, n. 2, p. 175–185, 1968.

SHARIFABADI, K.; HARNEFORS, L.; NEE, H.-P.; NORRGA, S.; TEODORESCU, R. **Design, control, and application of modular multilevel converters for HVDC transmission systems**. [S.l.]: John Wiley & Sons, 2016.

SONTAG, E. D. **Mathematical control theory: deterministic finite dimensional systems**. [S.l.]: Springer Science & Business Media, 2013. v. 6.

SOUZA, I. D. N.; ALMEIDA, P. M.; FOGLI, G. A.; BARBOSA, P. G.; RIBEIRO, P. F. Multivariable optimal control applied to a back-to-back power converter. **IEEE Transactions on Industrial Electronics**, p. 1–13, 2021.

STEINMETZ, C. P. Theory of the general alternating current transformer. **Transactions of the American Institute of Electrical Engineers**, IEEE, v. 12, p. 245–256, 1895.

STROGATZ, S. H. **Nonlinear dynamics and chaos with student solutions manual: With applications to physics, biology, chemistry, and engineering**. [S.l.]: CRC press, 2018.

SUN, J.; GROTSTOLLEN, H. Averaged modelling of switching power converters: Reformulation and theoretical basis. In: IEEE. **PESC'92 Record. 23rd Annual IEEE Power Electronics Specialists Conference**. [S.l.], 1992. p. 1165–1172.

SUNTIO, T.; MESSO, T.; PUUKKO, J. **Power electronic converters: dynamics and control in conventional and renewable energy applications**. [S.l.]: John Wiley & Sons, 2017.

TEODORESCU, R.; LISERRE, M.; RODRIGUEZ, P. **Grid converters for photovoltaic and wind power systems**. [S.l.]: John Wiley & Sons, 2011. v. 29.

TREFETHEN, L. N.; III, D. B. **Numerical linear algebra**. [S.l.]: Siam, 1997. v. 50.

WATSON, G. N. **A treatise on the theory of Bessel functions**. 2. ed. [S.l.]: cambrige university press, 1944. ISBN 9780521483919.

YAZDANI, A.; IRAVANI, R. **Voltage-sourced converters in power systems: modeling, control, and applications**. [S.l.]: John Wiley & Sons, 2010.

ZHOU, K.; DOYLE, J. C. **Essentials of robust control**. [S.l.]: Prentice Hall Upper Saddle River, NJ, 1998. v. 104.